

OCEAN CURRENT ENERGY RESOURCE ASSESSMENT FOR THE
UNITED STATES

A Dissertation
Presented to
The Academic Faculty

by

Xiufeng Yang

In Partial Fulfillment
of the Requirements for the Degree
Doctor of Philosophy in the
School of Civil and Environmental Engineering

Georgia Institute of Technology
December 2013

Copyright © 2013 by Xiufeng Yang

OCEAN CURRENT ENERGY RESOURCE ASSESSMENT FOR THE
UNITED STATES

Approved by:

Kevin A. Haas, Committee Chair
School of Civil and Environmental
Engineering
Georgia Institute of Technology

Hermann M. Fritz
School of Civil and Environmental
Engineering
Georgia Institute of Technology

Philip J. Roberts
School of Civil and Environmental
Engineering
Georgia Institute of Technology

Emanuele Di Lorenzo
School of Earth and Atmospheric
Sciences
Georgia Institute of Technology

Paul A. Work
California Water Science Center
U.S. Geological Survey

Date Approved: November 11, 2013

ACKNOWLEDGEMENTS

I would like to express my deepest gratitude to my advisor Dr. Kevin Haas, for providing me with research opportunities and his patient and enlightening guidance throughout my time at Georgia Tech. I am extremely grateful for the invaluable time Dr. Hermann Fritz has invested in advising my research. I sincerely thank Dr. Paul Work for educating me in various topics in coastal engineering and providing me with field and teaching experiences. I want to sincerely thank Dr. Di Lorenzo for enriching my knowledge in oceanography and his continuous support since my thesis proposal. I also wish to thank Dr. Philip Robert for serving on my thesis committee and his comments on my thesis. I would also like to thank other professors, Dr. Donald Webster, Dr. David Scott, Dr. Annalisa Bracco, and many others who are of great help to make this dissertation happen.

I want to show my greatest appreciation to Dr. Fabrice Bonjean from SAT-OCEAN for his brilliant ideas in processing ocean data. I truly appreciate all the help I have received from the HYCOM online forum, especially from Dr. Alan Wallcraft. I want to thank U.S. Department of Energy for providing financial support and invaluable feedback.

I am deeply thankful for the support from my colleagues from Georgia Tech Savannah campus: Brittany Bruder, Brian McFall, Stephanie Smallegan, Zafer Defne, Chatchawin Srisuwan, Thomas Stone, Dongsik Chang, Lide Jiang, Fahad Mohammed, Thomas Gay, Adam Sapp, Heidi Hammerstein and many others. Without all the memories shared with them, my graduate school will be colorless. I also want to thank all my friends and all the memories from Savannah, especially John Tzen, C.K. and Rose for loving me like family, and Rui Sun for understanding and caring about me. Savannah is a beautiful city that everyone who has read this dissertation should visit.

Last but not least, I want to thank my dad, mom, sister and my brother-in-law for their unconditional love and endless support for my education. Although thousands of miles apart, they are always my source of love, courage, and perseverance.

TABLE OF CONTENTS

ACKNOWLEDGEMENTS	iii
LIST OF TABLES	vi
LIST OF FIGURES	vii
SUMMARY	xiv
I INTRODUCTION	1
II LITERATURE REVIEW	6
2.1 Status of Ocean Renewable Energy	6
2.2 Western Boundary Current Dynamics	9
2.3 Overview of the Gulf Stream	11
2.4 Ocean Current Energy Assessment	14
2.4.1 Energy Extraction Devices	14
2.4.2 Ocean Energy Budget	15
2.4.3 Assessment Based on Power Density	17
2.4.4 Assessment Based on Dynamic Models	19
2.5 Motivation for Present Study	20
III CHARACTERIZING OCEAN CURRENTS IN THE UNITED STATES 22	
3.1 Ocean Model Data Sources	22
3.1.1 Available Numerical Model Data	22
3.1.2 Model Selection	24
3.2 Variability of the Florida Current	27
3.3 Kinetic Energy Flux in the Florida Current	33
3.3.1 Characterizing Kinetic Energy Flux in the Florida Current	33
3.3.2 Estimating 30 Years of Kinetic Energy Flux	36
3.4 Dissemination of Data	39
3.5 Data Probability Uncertainty	43
IV ESTIMATES OF POWER POTENTIAL	46
4.1 Simplified Ocean Circulation Model	46
4.2 Model Calibration	49

4.3	Uniform Turbine Drag	51
4.4	Localized Turbine Drag	57
4.5	Numerical Model Validation	61
4.6	Total Energy Dissipation by Localized Turbines	62
4.7	Effects of Localized Turbine Drag	65
4.8	Total Available Power from Undisturbed Power Density	73
4.9	Total Power Summary	79
V	MODELING EFFECTS OF POWER EXTRACTION WITH HYCOM	81
5.1	Model Configurations	81
5.2	Baseline Results	86
5.3	Modeling Turbines	90
5.4	Effects of Power Extraction from the Florida Current	93
5.4.1	Change in Mean Surface Current	93
5.4.2	Change in Sea Surface Height (SSH)	97
5.4.3	Change in Mean Power Density	99
5.4.4	Temporal Effects of Power Extraction	105
5.5	Summary	115
VI	CONCLUSIONS	119
APPENDIX A	— DIRECT COMPARISON BETWEEN MODEL AND	
	DRIFTER DATA	127
REFERENCES	138

LIST OF TABLES

3.1	Summary of available numerical model data.	23
3.2	Example of drifter data from GDP.	24
3.3	Statistical comparison results for the west and Alaska coasts.	27
3.4	Statistical comparison between models for the east coast	29
3.5	Ocean model data chosen for different areas	29
4.1	The relative error ($RMS/MEAN$) between analytical and numerical total energy dissipation for different spatial resolutions and different t values. . .	62
4.2	The values of approximate turbine region area, peak turbine drag coefficient, and peak power for all scenarios.	64
4.3	Comparing power estimate in theory with the estimate based on undisturbed kinetic power.	79
5.1	Summary of 4 different power extraction cases.	93
5.2	Summary of the effects of power extraction for four different cases.	104

LIST OF FIGURES

2.1	Schematic of the North Atlantic surface ocean circulation.	11
2.2	Satellite image of the Gulf Stream meanders shown from surface temperature, June 1984 (NASA, 2012)	13
2.3	Examples of (a): horizontal axis turbine (Verdant Power); (b): vertical axis turbine (GCK Technology); (c): ducted turbine (Lunar Energy); (d): C-plane turbine (Aquantis, LLC)	16
2.4	Energy budget for the global ocean (shaded boxes are the principal energy reservoirs in the ocean, with crude energy values given in exajoules (EJ) 10^{18} J, and yottajoules (YJ) 10^{24} J; fluxes to and from the reservoirs are in terrawatts (TWs).) (Wunsch and Ferrari, 2004)	17
3.1	Spatial coverage of available ocean models.	23
3.2	Status of global drifter arrays on May 28, 2012 (source: NOAA).	25
3.3	Comparing drifter data with interpolated model data.	25
3.4	Division of east coast area into E1-E9 sub-regions.	28
3.5	GIS map showing the mean surface current power density for the U.S. coast.	28
3.6	Comparison of 30-day running averaged volume flux in the Florida Current between cable measurement and two versions of HYCOM data: (a) Global HYCOM and (b) HYCOM GoM.	30
3.7	Comparison of one-year averaged vertical current speed profiles between ADCP measurement and HYCOM GoM data located at approximately (26.07N, 79.84W).	31
3.8	Distributions of (a) annual mean surface current speed, (b) standard deviation, and (c) the coefficient of variation in the Florida Current.	32
3.9	Cross-sectional distributions of (a) annual mean current speed, (b) standard deviation, and (c) the coefficient of variation in Florida Current at the latitude of 26.6264N.	32
3.10	Time series of total kinetic energy flux in the Florida Current.	33
3.11	Yearly variation of (a) mean kinetic energy flux and (b) standard deviation in the Florida Current from 2004 to 2010.	34
3.12	Monthly variation of (a) mean kinetic energy flux and (b) standard deviation in the Florida Current.	34
3.13	Vertical kinetic energy flux density in the Florida Current for selected months (Feb., May, Jul., and Nov.) and annual mean.	35

3.14	(a) Least square fit of the relationship between volume and kinetic energy flux with 95% confidence interval from 2004 to 2010, and (b) projected 30-year low-pass filtered time series of kinetic energy flux based on historical cable data with 95% confidence interval.	37
3.15	Predicted kinetic energy flux from 2004 to 2006 from cable data with the energy flux calculated from HYCOM model data: (a) time series of daily data, and (b) 30-day running averaged time series.	37
3.16	Least square fit of the relationship between volume and kinetic energy flux with 95% confidence interval from 2004 to 2010.	38
3.17	Projected 30-year low-pass filtered time series of kinetic energy flux based on historical cable data with 95% confidence interval.	39
3.18	Monthly variation of (a) mean kinetic energy flux and (b) standard deviation in the Florida Current based on projected 30 years of kinetic energy flux data.	39
3.19	Yearly variation of (a) mean kinetic energy flux and (b) standard deviation in the Florida Current based on projected 30 years of kinetic energy flux data.	40
3.20	GIS map of mean surface ocean current speed with pull down menus on the top and interactive widgets on the right.	41
3.21	Example figures of vertical current speed profiles for location (26.912N, 79.680W): (a) monthly variation and (b) standard deviation.	42
3.22	Example figures of (a) joint and (b) marginal probability distributions of surface current velocity for (26.912N, 79.680W).	43
3.23	Confidence interval profiles for probability estimation based on (a) daily data of 7 years, and (b) daily data for an individual month of 7 years.	45
3.24	An example of the probability distribution and 95% confidence interval of surface current speed at (26.912E, 79.600W) estimated from (a) daily data of 7 years, (b) daily data of only December.	45
4.1	Location of the selected cross-section (red line) in the Gulf Stream system, through which volume flux and energy flux are calculated and compared: (a) the North Atlantic Basin, and (b) the simplified basin with analytical streamlines.	50
4.2	(a) Error Factor “E.F.” as a function of varying maximum wind stress τ_0 and natural friction coefficient C_d for different depths, and (b) “E.F.” as a function of depth.	52
4.3	Spatial variation of each term in the x momentum equation: (a) Coriolis forcing, (b) drag force, (c) wind stress, (d) pressure gradient.	55
4.4	Spatial variation of each term in the y momentum equation: (a) Coriolis forcing, (b) drag force, (c) pressure gradient.	56

4.5	Power dissipation from turbines for three different flow conditions as a function of the turbine drag coefficient; energy dissipation by turbines for the mean flow condition is highlighted in red and the corresponding natural dissipation is highlighted in blue.	57
4.6	Distribution of the non-dimensional localized turbine drag in the Gulf Stream ($\epsilon = 10^4 km^2$).	59
4.7	Non-uniform mesh grid for the domain with $t=3$, $n=50$, and $m=30$	60
4.8	(a) Analytical and numerical total energy production/dissipation, and (b) energy dissipation by turbines and natural dissipation from both analytical and numerical solutions for case T3.	63
4.9	(a) Approximate areas of turbine regions for 5 different scenarios, (b) energy dissipation by turbines as a function of the peak turbine drag coefficient C_{t0} for different scenarios.	64
4.10	Energy dissipation by turbines as a function of turbine drag coefficient for three different seasonal flow conditions for scenario A (red curve highlighting the mean flow condition).	65
4.11	Changes of (a) zonal velocity component, (b) meridional velocity component due to additional localized turbine drag (scenario A).	66
4.12	Comparing (a) zonal (u), and (b) meridional (v) current velocity components along the western boundary layer ($x \approx 2km$) for undisturbed circulation and circulation with localized turbine drag (scenario A).	67
4.13	Force balance along the western boundary layer ($x \approx 2km$) for (a) undisturbed case and (b) the case with localized turbine drag (scenario A).	68
4.14	Ocean surface elevation with lines of constant pressure for (a) undisturbed case, (b) case with additional turbines, and (c) the sea surface change after additional turbine drag is added.	69
4.15	Streamlines for (a) undisturbed circulation, (b) circulation with localized turbine drag.	70
4.16	Spatial variation of each term from Equation 4.16 with localized turbine drag (scenario A): (a) density of energy dissipation by turbines; (b) density of natural energy dissipation; (c) density of energy production by wind; (d) work done by pressure gradient.	71
4.17	(a) Undisturbed streamlines with multiple cross-sections every 10 degrees, (b) residual energy flux for each cross-section on left with different level of localized energy dissipation from the Gulf Stream by turbines.	72
4.18	Residual volume flux as a function of peak turbine drag coefficient C_{t0} for different scenarios.	73
4.19	Changes of (a) energy production, and (b) natural energy dissipation in the circulation with turbine drag coefficient for different scenarios.	74

4.20	The area in the Florida Current where the hypothetical turbine array will be deployed.	75
4.21	Monthly variation of (a) total kinetic power and (b) power per device from the hypothetical turbine array.	76
4.22	Area with black dots representing the area with mean current speed exceeding 1 m/s.	76
4.23	Monthly variation of (a) total kinetic power and (b) power per device with devices only deployed in areas with mean speed exceeding 1 m/s.	77
4.24	(a) The turbine region including sections up and down stream of the Florida Current, and (b) the monthly variation of total kinetic power.	78
4.25	(a) The turbine area including offshore of Cape Hatteras, and (b) the monthly variation of total kinetic power.	78
5.1	HYCOM computational domain with bathymetry	83
5.2	The annual mean surface wind stress on the North Atlantic Ocean derived from ERA15 dataset.	85
5.3	The monthly mean surface wind stress for the Florida Current from ERA15 dataset for (a) July and (b) January, with red dots showing the locations of F1, F2 and F3.	85
5.4	The monthly mean wind stress vectors of 12 months for 3 different locations (F1, F2 and F3) located along the U.S. east coast.	86
5.5	Time series of region mean kinetic energy.	87
5.6	Annual mean surface current speed for undisturbed condition (m/s).	88
5.7	Annual mean power density of the top 200m water column for undisturbed condition (W/m^2).	88
5.8	Monthly mean volume flux in the Florida Current from both model results (blue) and submarine cable measurement (red).	90
5.9	Two layouts of turbines in the Florida Strait with blue areas representing the approximate locations of turbine region; layout (a) is used in cases 1 and 3, while layout (b) is used in cases 2 and 4.	92
5.10	(a) Annual mean surface current speed in power extraction case 1, (b) change in mean surface current speed in case 1 relative to the baseline (m/s); black box outlines the location of turbines.	94
5.11	(a) Annual mean surface current speed in power extraction case 2, (b) change in mean surface current speed in case 2 relative to the baseline (m/s); black box outlines the location of turbines.	95
5.12	The difference of the surface mean current speed between summer (30-day average in July) and winter (30-day average in December) for case 1; black box outlines the location of turbines.	95

5.13	(a) Annual mean current speed at 100 m in power extraction case 1, (b) change in mean current speed at 100 m in case 1 relative to the baseline (m/s) ; black box outlines the location of turbines.	96
5.14	(a) Annual mean current speed at 100 m in power extraction case 2, (b) change in mean current speed at 100 m in case 2 relative to the baseline (m/s); black box outlines the location of turbines.	96
5.15	The volume flux in the Florida Current for undisturbed case (red), power extraction case 1 (blue) and power extraction case 2 (magenta).	97
5.16	Annual mean SSH for the baseline case.	98
5.17	(a) Annual mean SSH in power extraction case 1, (b) change in mean SSH in case 1 relative to the baseline (<i>m</i>); black box outlines the location of turbines.	99
5.18	(a) Annual mean SSH in power extraction case 2, (b) change in mean SSH in case 2 relative to the baseline (<i>m</i>); black box outlines the location of turbines.	99
5.19	(a) Annual mean power density of the top 200 m water column in power extraction case 1, (b) change in mean power density of the top 200 m water column in case 1 relative to the baseline (W/m^2); black box outlines the location of turbines.	101
5.20	(a) Annual mean power density of the top 200 m water column in power extraction case 2, (b) change in mean power density of the top 200 m water column in case 2 relative to the baseline (W/m^2); black box outlines the location of turbines.	101
5.21	Power dissipation from turbines in case 1 together with the undisturbed and residual kinetic energy flux starting from April of the 7th year.	102
5.22	Power dissipation from turbines in case 2 together with the undisturbed and residual kinetic energy flux starting from April of the 7th year.	104
5.23	Locations of the 5 selected points shown in the annual mean surface current speed map (m/s).	105
5.24	Current velocities and SSH at location A (79.6W, 27.5N) for undisturbed flow and for case 1 with positive <i>u</i> velocity being eastward and positive <i>v</i> velocity northward.	107
5.25	Current velocities and SSH at location B (78.8W, 28.7N) for undisturbed flow and for case 1 with positive <i>u</i> velocity being eastward and positive <i>v</i> velocity northward.	108
5.26	Current velocities and SSH at location C (82.2W, 26.4N) for undisturbed flow and for case 1 with positive <i>u</i> velocity being eastward and positive <i>v</i> velocity northward.	109
5.27	Current velocities and SSH at location D (74.2W, 34.2N) for undisturbed flow and for case 1 with positive <i>u</i> velocity being eastward and positive <i>v</i> velocity northward.	110

5.28	Flow field change in case 1 relative to the baseline case on day 155 (a) and day 250 (b) for location D.	110
5.29	Current velocities and SSH at location E (82.8W, 23.9N) for undisturbed flow and for case 1 with positive u velocity being eastward and positive v velocity northward.	111
5.30	Current velocities and SSH at location A (79.6W, 27.5N) for undisturbed flow and for case 2 with positive u velocity being eastward and positive v velocity northward.	112
5.31	Current velocities and SSH at location B (78.8W, 28.7N) for undisturbed flow and for case 2 with positive u velocity being eastward and positive v velocity northward.	112
5.32	Current velocities and SSH at location C (82.8W, 26.4N) for undisturbed flow and for case 2 with positive u velocity being eastward and positive v velocity northward.	113
5.33	Current velocities and SSH at location D (74.2W, 34.2N) for undisturbed flow and for case 1 with positive u velocity being eastward and positive v velocity northward.	114
5.34	Current velocities and SSH at location E (82.8W, 23.9N) for undisturbed flow and for case 2 with positive u velocity being eastward and positive v velocity northward.	114
5.35	Changes in (a) annual mean surface current speed and (b) instantaneous surface current speed at day 360 for case 1.	115
5.36	Current velocities and SSH at location F (51.6W, 7.6N) for undisturbed flow and for case 1 with positive u velocity being eastward and positive v velocity northward.	116
5.37	Variance of surface current speed for the undisturbed condition case (a) and case 1 (b).	116
5.38	Change of variance of surface current speed in case 1.	117
A.1	Comparison of Global HYCOM data with measurement data for E1 region.	127
A.2	Comparison of HYCOM GoM data with measurement data for E1 region.	128
A.3	Comparison of NCOM data with measurement data for E1 region.	128
A.4	Comparison of Global HYCOM data with measurement data for E2 region.	129
A.5	Comparison of HYCOM GoM data with measurement data for E2 region.	129
A.6	Comparison of NCOM data with measurement data for E2 region.	130
A.7	Comparison of Global HYCOM data with measurement data for E3 region.	130
A.8	Comparison of HYCOM GoM data with measurement data for E3 region.	131
A.9	Comparison of NCOM data with measurement data for E3 region.	131

A.10 Comparison of Global HYCOM data with measurement data for E4 region.	132
A.11 Comparison of NCOM data with measurement data for E4 region.	132
A.12 Comparison of Global HYCOM data with measurement data for E5 region.	133
A.13 Comparison of NCOM data with measurement data for E5 region.	133
A.14 Comparison of Global HYCOM data with measurement data for E6 region.	134
A.15 Comparison of NCOM data with measurement data for E6 region.	134
A.16 Comparison of Global HYCOM data with measurement data for E7 region.	135
A.17 Comparison of NCOM data with measurement data for E7 region.	135
A.18 Comparison of Global HYCOM data with measurement data for E8 region.	136
A.19 Comparison of NCOM data with measurement data for E8 region.	136
A.20 Comparison of Global HYCOM data with measurement data for E9 region.	137
A.21 Comparison of NCOM data with measurement data for E9 region.	137

SUMMARY

Increasing energy consumption in recent years together with increasing public awareness and concerns about climate change and environmental pollution have spurred growing interest in different types of renewable energy. Ocean currents are an attractive source of renewable energy due to their inherent reliability, persistence, and sustainability. General ocean circulations exist in the form of large rotating ocean gyres, and feature extremely rapid current flow in the western boundaries due to the Coriolis Effect. The Gulf Stream system is the western boundary current of the North Atlantic Ocean that flows along the east coastline of the United States. In this dissertation a comprehensive resource assessment of ocean currents as a potential renewable energy source for the United States is performed with a major emphasis on the Gulf Stream. The Gulf Stream system is of particular interest as a potential energy resource to the United States with significant currents and proximity to a large population on the U.S. east coast.

To assess the energy potential from ocean currents for the United States, the characterization of ocean currents along the U.S. coastline is performed in this study. A GIS database that maps the ocean current energy resource distribution for the entire U.S. coastline and also provides joint velocity magnitude and direction probability histograms was developed using seven years of numerical model data to help advance awareness in ocean current energy resource assessment. The accuracy of the database was evaluated by Ork Ridge National Laboratory (ORNL)'s independent validation effort. A web-based GIS interface was designed by Georgia Tech's GIS center (<http://www.oceancurrentpower.gatech.edu/>) for dissemination of the data. The website includes GIS layers of monthly and yearly mean ocean current velocity and power density for ocean currents along the entire coastline of the United States, as well as joint and marginal probability histograms for current velocities at a horizontal resolution of 4-7 km with 10-25 bins over depth. Various tools are provided for viewing, identifying, filtering and downloading the data.

The Florida Current is found to have a much higher power density than other offshore areas in the U.S. with the majority of the kinetic energy concentrated in the upper 200 m of the water column. Having a geographical constraint by Florida and the Bahamas, the Florida Current is fairly stable with prevalent seasonal variability in the upper layer of the water column resulting from surface momentum flux variation. The core of the Florida Current features higher stability than the edges as a result of the meandering and seasonal broadening of the current flow. The spatial and temporal variabilities of the Gulf Stream significantly increase as it flows past Cape Hatteras.

The theoretical energy balance in the Gulf Stream system is examined using the two-dimensional ocean circulation equations based on the assumptions of the Stommel model for subtropical gyres with the quasi-geostrophic balance between pressure gradient, Coriolis force, wind stress, and friction driving the circulation. Additional turbine drag is formulated and incorporated in the model to represent power extraction by turbines. Parameters in the model are calibrated against ocean observational data such that the model can reproduce the volume and kinetic energy fluxes in the Gulf Stream. The results show that considering extraction over a region comprised of the entire Florida Current portion of the Gulf Stream system, the theoretical upper bound of the average power dissipation is around 5.1 GW, or 45 TWh/yr. If the extraction area comprises the entire portion of the Gulf Stream within 200 miles of the U.S. coastline, the theoretical upper bound of the averaged power dissipation becomes approximately 18.6 GW or 163 TWh/yr. The impact of the power extraction is primarily constrained in the vicinity of the turbine region, and includes a significant reduction of flow strength and water level drop in the power extraction site. The turbines also significantly reduce residual energy fluxes in the flow, and cause redirection of the Gulf Stream.

A full numerical simulation of the ocean circulation in the Atlantic Ocean was performed using the Hybrid Coordinate Ocean Model (HYCOM) and power extraction from the Florida Current is modeled as an additional momentum sink. The effects of power extraction are shown to include flow rerouting from the Florida Strait channel to the east of the Bahamas. A prominent seasonal variability of power extraction is not observed due to stronger flow

diversion from the Florida Current in seasons with stronger flow. A significant water level drop is shown at the power extraction site, as is a slight water level rise along the coasts of the Gulf and Florida. The sum of extracted power and the residual energy flux in the Florida Current is lower than the original energy flux in the baseline case, indicating a net loss of kinetic energy reserve in the Florida Current channel due to flow redirection. The impact from power extraction on the mean flow field is concentrated in the near field of the power extraction site, while shifts in the far flow field in time and space have little impact on the overall statistics.

CHAPTER I

INTRODUCTION

There is a growing interest in renewable energy around the world. The increasing demand for electrical energy and the decreasing availability of fossil fuels is a sign of the upcoming energy crisis for the human society. Concerns over climate changes and reduction of carbon emissions have been driving forces for seeking affordable and environmentally friendly energy alternatives (Vanek et al., 2008). The decrease in fossil fuel reserves makes renewable energy attractive to both government and industry. Some countries are also seeking energy independence by reducing fossil fuel imports from foreign regions and developing domestic alternatives of clean energy.

The modernization of the global economy is a direct result of fossil fuel consumption including fossil oil, natural gas and coal. In the past three decades global energy consumption has almost doubled, and it is predicted that global energy demand will be about 30 percent higher in 2040 compared to 2010 (ExxonMobil, 2012). In 2004, more than 75% of the primary energy consumption was from fossil fuels, whereas only about 5% was from renewable resources (Beretta, 2007). In 2012, 13.2% of the domestically produced electricity came from renewable energy resources in the United States (EIA, 2013). On one hand, fossil fuels are non-renewable and will eventually be used up. On the other hand, as the primary source of energy, fossil fuels have hidden costs. Burning fossil fuels causes pollution and environmental degradation by releasing carbon dioxide (CO_2) into the air, resulting in acid rain, water pollution and global warming. Moreover, national energy security can be threatened by dependency on foreign sources of fossil fuels. Due to increasing concerns about environmental pollution as well as energy security, countries are increasingly recognizing the importance of renewable energy. A rush of investment into renewable energy therefore has been observed in recent years.

Renewable energy comes from sources that are continually replenished, such as solar,

wind and water hydro energy. Renewable energy has great benefits compared to fossil fuels, including environmental improvement, fuel diversity and national security if it can supply a significant portion of the country's energy needs. Furthermore, renewable energy industry investments will most likely be spent on materials and infrastructure rather than on energy imports, and therefore will help fuel local economies by creating more jobs.

The renewable energy industry is growing strongly in recent years. In 2012, the global investment in renewable energy reached \$244 billion US dollars. Global capacity of solar energy reached 40GW and capacity of wind energy reached 198GW (REN21, 2012). One frontier of renewable energy is in the ocean. Although oceans cover more than 70% of the earth's surface and are promising reservoirs of alternative energy resources, energy production from the ocean presently only makes up a negligible portion of our daily energy supply. In countries with coastlines, coastal areas are usually home to a wealth of natural and economic resources and are typically the most developed areas in the country. Renewable energy from the coastal and offshore regions can be conveniently used to supply the most populated areas in the country if harvested efficiently from the ocean. Fast moving ocean currents are a significant reservoir of ocean kinetic energy. Since water is about 800 times denser than air, ocean current flow with the same speed has a much higher power density than wind.

In most areas of the ocean, the current flow is not strong enough to be economically used as a power supply. But in regions with extremely strong flow such as the Gulf Stream, ocean currents can potentially provide sufficient and possibly cost-effective power. Technology for extracting kinetic energy from ocean currents, although existing, is still far from mature. Numerous research efforts have been taken to develop efficient and advanced technology for recovering energy from ocean currents. In 2007, an experimental array of grid-connected turbine developed by Verdant Power were installed in the East River in New York (VerdantPower, 2007). In 2008, a dual 16 m-diameter rotor SeaGen turbine was installed in Strangford Narrows in Northern Ireland (Westwood, 2008). OpenHydro of Ireland installed a 6 m-diameter in-stream turbine in a tidal test facility in 2007 and installed a 10 m-diameter turbine at the Nova Scotia Minas Passage Tidal Demonstration site in 2009

(OpenHydro, 2009). Most existing turbine technologies were developed for extracting tidal current energy, but can also be leveraged for open ocean current energy extraction. The world's first marine current turbine experimental system big enough for offshore locations was installed at 1 km offshore of North Devon, UK in 2003 (Bedard et al., 2010).

Ocean current patterns vary both spatially and temporally, it is therefore desirable to conduct thorough resource assessments to produce accurate estimates of power production potential, costs and optimal engineering strategy before turbine deployment. Environmental influences in both near and far fields need to be evaluated. Resource assessments specifically for ocean current energy in the Gulf Stream date back to 1977, when a team led by Aerovironment Inc. conducted some preliminary studies to estimate power production from the Gulf Stream current and its environmental effects (Lissaman, 1979). A more conservative prediction made by Von Arx et al. (1974) suggests that an amount of up to 1 GW kinetic power can be extracted from the Gulf Stream by turbines without seriously disrupting climatic conditions. However, neither author elucidated on the details of their resource estimates. In 2005 the Florida Atlantic University (FAU) formed a team of researchers to investigate feasibility of extracting ocean current energy from the Gulf Stream. However present knowledge of the energy potential in the Gulf Stream and its extractability is still incomplete. Successful formulae for calculating maximum extractable energy from ocean currents still do not exist. Near and far field effects of energy extraction from ocean currents are largely unknown.

The present study included a comprehensive assessment on ocean current energy potential in the United States to fill in the gap in this research area. Ocean current energy can be extracted in a similar way as wind energy by using turbines. However, the ocean renewable energy industry lags about a decade behind the wind industry and therefore holds enormous potential as a new energy resource (Mueller and Wallace, 2008). Undisturbed kinetic power density of the current flow is a reasonable representation of the richness of the ocean current energy resources, and provides an order-of-magnitude estimate of the availability of the energy resource. When only a small number of power conversion devices are used,

power density provides a meaningful estimate of the extractable power with turbines. However, when a large number of devices are used and large amount of energy is extracted, the current velocity will be reduced due to obstruction of conversion devices, and the estimate based on undisturbed power density may be questionable. Therefore, the dynamics of the circulation system need to be studied in order to properly estimate the upper limit of the energy potential in theory.

In this dissertation, a comprehensive literature review is presented to gain an understanding of the current status of different types of renewable energy resources from the ocean. A detailed explanation of the western boundary current intensification is also presented. Since the Gulf Stream system is of particular interest to the United States, a thorough review on the formation and characteristics of the Gulf Stream is also provided in the literature review, together with a survey of the past efforts on estimating the energy potential from the Gulf Stream system.

The literature review is followed by characterization of ocean currents along the United States with emphasis on the Gulf Stream. The characterization of ocean currents is based on a 7-year ocean model simulation and a GIS database with web interface is developed to support dissemination of data. Both spatial and temporal variabilities of the Gulf Stream are analyzed based on this 7 years of ocean model data, and undisturbed power potential is estimated for the Gulf Stream. Although the undisturbed power density provides an order-of-magnitude estimate for the available power potential in ocean currents, this is insufficient when a large number of devices will result in considerable current velocity reduction. To incorporate the cumulative effects from power conversion devices, a simple two-dimensional ocean circulation model is utilized based on the assumptions of the Stommel model to study the dynamics and energy balance of the quasi-geostrophic currents. Turbines are included in the model as additional drag force, and different drag coefficients are formulated to represent different surface areas of the turbine region and different strength of energy extraction. This simplified ocean circulation model is able to provide theoretical estimate on the upper limit of power potential from the Gulf Stream, and also evaluate the effects from energy extraction by turbines. However, 2-D model has its limitations, and therefore

a full numerical modeling of the circulation in the North Atlantic ocean is performed with HYCOM to obtain a more realistic representation of the Gulf Stream system. Turbines are included in the model as additional momentum sink. Large scale hydrodynamic effects of power extraction on the flow regime are evaluated for both the near and far fields.

CHAPTER II

LITERATURE REVIEW

The literature review is presented in four parts. The first part reviews the current status of different types of ocean renewable energy technologies. The second part reviews the mechanism of the western boundary current of subtropic gyres in ocean basins. The third part presents an overview of the formation and characteristics of the Gulf Stream. The last part reviews the current status and popular methodologies for ocean current energy assessment.

2.1 Status of Ocean Renewable Energy

One frontier of renewable energy is in the ocean. In the ocean, energy can be derived from different sources, including wind, surface water waves, ocean gradients, tides and currents (Asmus and Wheelock, 2009; Bedard et al., 2010). It is predicted that the world's electricity produced by ocean based devices could reach 7% by 2050 (Esteban and Leary, 2012). The following section presents a brief overview of different types of ocean renewable energy.

Offshore Wind Energy

Wind farms have been built in offshore waters to generate electricity with wind turbines. Because of reduced surface roughness, offshore wind usually features greater speed than onshore wind (Koller et al., 2006). Since wind power is proportional to the cube of wind speed, faster wind speed will lead to significantly larger available power. Offshore wind turbines have a number of advantages over onshore turbines including more available transportation and erection equipment, less visual intrusion, and less critical turbine noise emissions (Musial and Butterfield, 2004). However, the negative side of offshore development includes higher costs, more difficult accessibility, corrosion and fouling. Offshore wind is considered by the U.S. Energy Information Agency as the new energy resource with the highest levelized cost (EIA, 2010). The environmental conditions at sea are also more severe. In the 21st century, several European countries and manufacturers are leading the

way in developing and installing offshore wind turbines. However, challenges remain for the offshore wind energy industry, such as power transmission and power stability (Manwell et al., 2010). In the United States, offshore waters are generally deeper than those in Europe, and therefore make it more challenging for developing new technology. It is predicted that with sufficient technology advancement, the cost for deepwater offshore wind energy could possibly reach the competitive level with traditional energy (Musial and Butterfield, 2004).

Ocean Wave Energy

Ocean surface waves are usually generated by wind blowing over the water surface, generating waves with various frequencies and wavelengths. Numerous devices have been proposed to convert wave energy into electricity through mechanical motions. The classification of devices include: point absorbers, attenuators, terminators, and overtopping devices based on their working principles (MMS, 2006). Point absorbers usually have components that move relative to each other along the vertical axis with the wave action driving energy converters to generate power. Attenuators are floating structures consisting of multiple segments, and are oriented parallel to the wave direction. Wave propagation causes flexing of devices and drives built-in energy converters. Terminators are usually installed onshore or nearshore to capture waves in a chamber. Periodic inflow and outflow of waves drive turbines to generate power. The Oscillating Water Column (OWC) is an example of terminator devices. Overtopping devices function like a tide barrage. The reservoirs of overtopping devices are filled with higher level of water from incoming waves and the release of the trapped water turns hydro turbines. There have been many research efforts on evaluating the possibility and potential of extracting wave power (e.g. Clement et al., 2002; EPRI, 2006, 2011). Numerous locations in different countries have been investigated for the availability of wave power for energy conversion in the past few decades (e.g. Salter, 1974; Kofoed et al., 2006; Henfridsson et al., 2007; Beyene and Wilson, 2007).

Ocean Thermal Energy

The temperature gradient in the ocean can also be utilized to generate energy. Ocean Thermal Energy Conversion (OTEC) uses the temperature difference between cooler deep

water and warmer surface water to run a heat engine and produce power. The U.S. government’s support for OTEC programs started in the 1980s, with Hawaii being selected as the first experimental location. The technologies to extract energy from ocean thermal gradients, although existing, are still in their infancies and far from commercialization (Bedard et al., 2010).

Tidal Energy

Tidal stream energy systems are currently in development at various locations where high tidal current speed occurs in relatively shallow water. Tidal currents originate from the rise and fall of sea levels due to combined gravitational forcing from the sun and the moon. Therefore, tides vary periodically on different time scales ranging from hours to months according to relative positions of the earth, the moon and the sun. Tides are a rich reservoir of both potential and kinetic energy. The classical method of energy harvesting is to trap water during high tides using a dam or barrage. Trapped water can be released later during low tide to generate electricity (Prandle, 1984). The La Rance tidal barrage in France, the Annapolis Royal Generating Station in Nova Scotia, Canada and the Jiangxia Station in China are all tidal energy facilities based on this working principle (Hammons, 1993). However, it is noted that tidal barrages may have potential negative impact on the local environment, which can be reduced at an economic cost (Wolf et al., 2009).

Tidal streams can also be tapped as a kinetic energy resource. A current energy converter extracts and converts the kinetic energy in the current into a transmittable energy form. The in-stream power per cross-sectional unit area, power density P , is calculated with the following equation:

$$P = \frac{1}{2}C_p\rho V^3 \tag{2.1}$$

where C_p is the conversion coefficient, ρ is density of the fluid and V is flow speed. Efficiencies of tidal power converters are reported to be between 16% and 50% (Ben Elghali et al., 2007; Gorban et al., 2001). Ocean water is about 800 times denser than air, so ocean currents of about one-tenth the wind speed can generate the same power as wind (Twidell and Weir, 2006). However tidal power has two shortcomings due to periodicity:

the tidal current strength oscillates four times a day in most places, and the amount of energy available at times of spring tides is considerably greater than during neaps. Whereas the effect of the first can be minimized by using generators at different places along the coast in different phases of the tidal wave, the second means that power generation oscillates with a fortnightly period. Tidal power assessments have been performed for different locations around the world, and the effects of tidal power extraction have also been studied (e.g. Sutherland et al., 2007; Karsten et al., 2008; Defne et al., 2012; Polagye et al., 2009; Blunden and Bahaj, 2006; Bryden et al., 2007).

Ocean Current Energy

Ocean currents are another attractive source of energy due to their inherent reliability, persistence and sustainability. Ocean currents originate from the general circulation of the global ocean, and tend to be more stable with fewer variations. Driving forces for large scale ocean currents include the earth's rotation, gravity, wind stresses, and density differences. Besides these, tides, river discharge, surface pressure gradients and bottom friction can also play roles in shaping the current. Various ocean current energy assessment studies have been carried out in the past for different areas of the ocean, such as the Agulhas Current (Wright et al., 2011; Marais et al., 2011) and Florida Current (Duerr and Dhanak, 2012). The prime example is the Straits of Florida where the Gulf Stream flows out of the Caribbean Sea and into the North Atlantic on its way to northern Europe. The peak speed of the current is more than 2 m/s at the surface decreasing with depth (Elert, 2002); therefore, the Florida Current has long been identified as a target for potential development of ocean current energy.

2.2 Western Boundary Current Dynamics

To evaluate the ocean current energy potential from the Gulf Stream system, the first step is to gain a good understanding of the ocean circulation system that generates currents such as the Gulf Stream system. The general ocean circulation is a result of combined forces including winds, Coriolis effect, temperature and salinity difference, tides, interactions with shorelines and seabeds, among others. In almost all ocean basins, ocean circulations exist

in the form of large rotating currents called gyres. There are five major ocean gyres around the globe: Indian Ocean Gyre, North Atlantic Gyre, North Pacific Gyre, South Atlantic Gyre, and South Pacific Gyre. Ocean gyres can also be categorized into subtropical gyres and subpolar gyres based on their locations (Thurman and Trujillo, 2003).

The subtropical gyres in the northern hemisphere are used as an example. Due to the rotation of the earth and westward trade winds, ocean currents are pushed towards the west side of the basin and against the eastern boundary of continents, resulting in pile-up of water mass along the east coast of continents. The westward trade winds in the tropics and the eastward westerlies at mid-latitudes exert a clockwise friction and thus a negative curl on the ocean surface, resulting in the equatorward Sverdrup Drift (Sverdrup, 1947). The widely known Gulf Stream system is formed by the equatorward depth-integrated flow returning northward in the western boundary. Western boundary currents are narrower and deeper than the eastern boundary currents, and can be 10 times faster and carrying 5 times as much water (Gross, 1993). This phenomenon, named western intensification, causes extremely strong western boundary currents, such as the Gulf Stream in Atlantic Ocean, the Kuroshio Current in the North Pacific Ocean and the Brazil Current in the South Atlantic Ocean.

The formation of extremely strong western boundary currents can be explained from a mathematical point of view by Sverdrup Transport Theory (Sverdrup, 1947). The Sverdrup Theory (Sverdrup Balance) pointed out a balance between the wind stress exerted on the ocean surface and the vertically integrated meridional transport of ocean water. The derivation is skipped here, and the Sverdrup Balance is expressed as

$$\beta M_y = \text{curl}_z(T) \tag{2.2}$$

where β is the rate of change of the Coriolis parameter with latitude, M_y is the vertical-integrated mass transport, and $\text{curl}_z(T)$ is the vertical component of the curl of the wind stress. The westward trade winds in the tropics and the eastward westerlies at mid-latitudes exert a clockwise friction, and thus create a negative curl on the subtropical surface of the Ocean, which results in a negative depth-integrated mass transport according to the

equation. This equatorward depth-integrated flow in the ocean then returns poleward in western boundary currents. Therefore clockwise surface wind stress contributes to the stronger western boundary currents.

2.3 Overview of the Gulf Stream

The Gulf Stream shown in Figure 2.1 is the strong western boundary current of the North Atlantic subtropical gyre, which is bounded approximately between 10° N and 50° N in latitude and by North America to the west and Europe to the east (Raye, 2002). The portion of the Gulf Stream running within the Florida Strait bounded by Florida and the Bahamas is also called the Florida Current (Leaman et al., 1987).

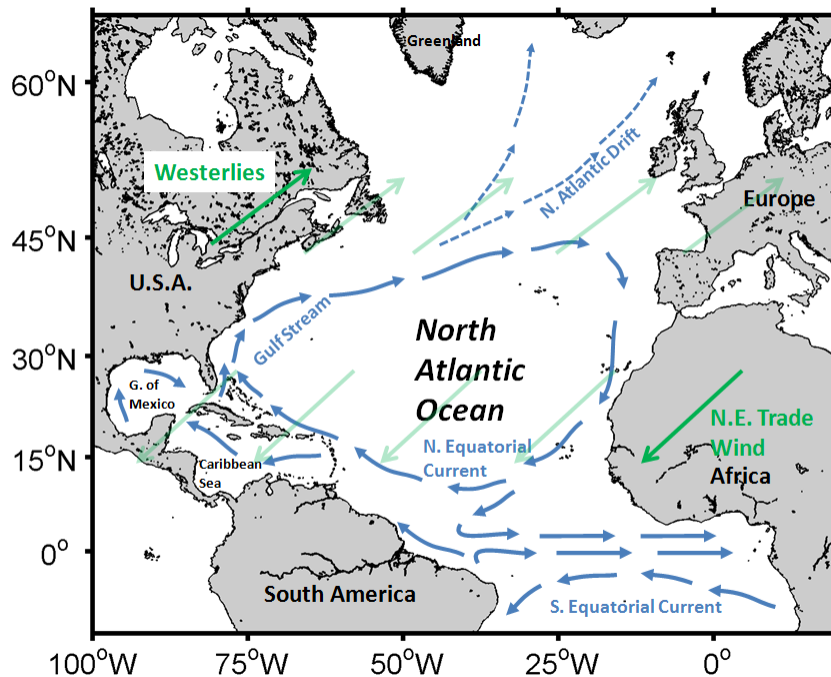


Figure 2.1: Schematic of the North Atlantic surface ocean circulation.

The discovery of the Gulf Stream dates back as far as the 1500s by Europeans. The first map of the Gulf Stream was charted by Benjamin Franklin in the 1700s. Systematic study of the Gulf Stream began in 1930 with Woods Hole Oceanographic Institution's (WHOI) acquisition of the ship *Atlantis*. Early hydrographic studies of the Gulf Stream in the U.S. started with Columbus Iselin, who was also the first master and designated physical oceanographer of *Atlantis*. His study gave a good idea of the general setting and

environment of the Stream and revealed the relation between temperature and salinity in this part of the ocean (Iselin, 1936).

The Gulf Stream transports a huge volume of water mass and heat. It starts from the Gulf of Mexico, flows as the Florida Current and leaves the east coast of the US near Cape Hatteras. The actual position where the Gulf Stream leaves the coast changes in time. It usually shifts north in the fall, and south in the winter (Auer, 1987). The volume transport in the Gulf Stream increases from about 30 Sv ($1 \text{ Sv} = 1 \times 10^6 \text{ m}^3/\text{sec}$) in the Florida Current to a maximum of about 150 Sv at approximately 45°W (Larsen and Sanford, 1985; Hogg and Johns, 1995). The increase in volume transport in the downstream direction is thought to result from the velocity increase in the deep water, which is due to deep ocean circulation (Hall and Fofonoff, 1993; Johns et al., 1995).

The Gulf Stream has variations both in space and in time. Fluctuations of transport as big as 30% of the mean are observed with different time scales (Greatbatch et al., 1995). The Gulf Stream transport has a strong seasonal variation, strongest in summer and weakest in winter (Niiler and Richardson, 1973; Baringer and Larsen, 2001). The fluctuation is mostly confined to the upper 300 m of the ocean, and is partly due to seasonal heat and expansion of the surface water (Hogg and Johns, 1995). Other variabilities at shorter periods can be attributed to lateral meanders and local wind forcing, among others (Duing, 1975; Lee and Williams, 1988).

The major tidal constituents contributing to the Gulf Stream are M_2 (semi-diurnal) and K_1 (diurnal), and their contribution to the surface current measured at approximately 0.05 m/s and 0.06 m/s, respectively (Leaman et al., 1987; Shay et al., 1998). Fluctuations from tides are relatively small compared to the fluctuations from northward advection of eddies and weekly periodic meanders (Lee, 1975). The Florida Current is not symmetric with the channel axis (the center line) with stronger flow on the shallower western side (Leaman et al., 1987). Such velocity non-uniformity generates horizontal shears, which results in eddies of 10-30 km in diameter (Raye, 2002).

The path of the Gulf Stream is not a straight line. It usually develops wave-like meanders, especially downstream of Cape Hatteras (see Figure 2.2). In the upstream meanders

are usually constrained by narrow continental shelves and have amplitude rarely exceeding 55 km. In the downstream, the meanders tend to be much bigger, with fluctuation as long as 400 km. The Gulf Stream meanders are not steady, but change over time. So the wave pattern can be very different in different months and years. Sometimes the Gulf Stream meanders break off the stream and form mesoscale eddies. Rings can form off a northward bending meander or a southward bending meander, which will create warm core rings and cold core rings respectively (Ring-Group, 1981; Joyce, 1984). Therefore rings can be found on both sides of the stream. Ring formation is a very important way for the ocean to redistribute heat and energy (Hogg and Johns, 1995). The Gulf Stream splits into two separate streams near the Grand Banks. One branch curves to the north along the continent and becomes the North Atlantic Current. The other one moves towards southeast and becomes Azores Current (Mann, 1967; Gould, 1985).

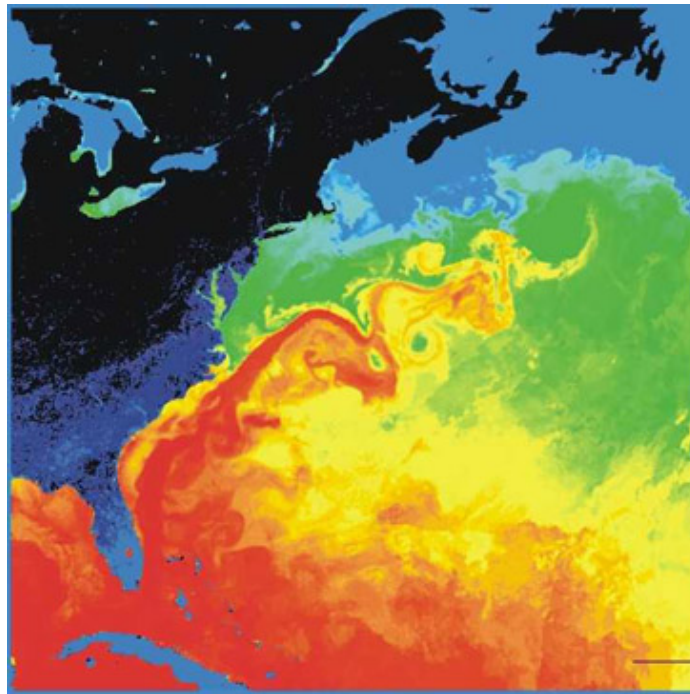


Figure 2.2: Satellite image of the Gulf Stream meanders shown from surface temperature, June 1984 (NASA, 2012)

The northern part of the Florida Strait bounded by Florida and the Bahamas confines the majority of the Gulf Stream to a narrow channel (Leaman et al., 1987). The Florida Current is approximately 100 km wide, and its maximum depth is about 800 m. The western

boundary of the Florida Current can be as close as 5 km to the Florida coast (Raye, 2002). On average, the axis of the Florida Current is about 350 m deep, and no more than 25 km from the Florida shoreline (Schott and Duing, 1976). The surface current velocity in the Florida Current can be as fast as 2.5 m/s. The Florida Current derives most of its water flow from the Gulf of Mexico and a minor portion from the Northwest Providence Channel and the Antilles Current (Hogg and Johns, 1995).

The intensified flow in the Florida Current due to restrictive geometry makes this region one of the most ideal sites for ocean current energy extraction on the east coast of the U.S. The nearby Miami metropolitan region, which is the seventh largest in the United States, according to the Bureau of the Census, with increasing energy demand, makes hydrokinetic energy extraction from this portion of the Gulf Stream potentially attractive as a component of a diversified renewable energy portfolio for the future (Hanson et al., 2010).

2.4 Ocean Current Energy Assessment

The western boundary currents with persistent and swift flows are the most appealing regions in terms of ocean current energy extraction. Among them, the Gulf Stream is one of the most intensively studied ocean currents. The potential of the Gulf Stream to provide clean and renewable energy have interested researchers for many years (Von Arx et al., 1974; Lissaman, 1979; Raye, 2002; Hanson et al., 2010, 2011; Duerr and Dhanak, 2012).

2.4.1 Energy Extraction Devices

Since the purpose of this study is to make a resource assessment of ocean current energy potential and will not be based on any specific turbine technologies, only a brief overview of turbine designs is provided. The basic design principles categorize underwater turbines into several types. A common design has a horizontal axis (see Figure 2.3(a) for example). The horizontal axis turbine design has been widely used in wind energy extraction, and is also suitable for ocean current energy extraction. The main rotor shaft of horizontal axis turbines is pointed parallel to the water current direction. Horizontal axis turbines are sometimes designed to allow for pitching or yawing motions so that turbines can face against the incoming flow. Such designs can guarantee maximum volume flux through the

turbine and a higher efficiency. The main rotor shaft of turbines can also be positioned vertically (see Figure 2.3(b) for example). Vertical axis design has both advantage and disadvantage compared with horizontal axis design. Since the vertical axis turbines will not need to be facing the direction of incoming flow to maximize efficiency, they are especially suitable for areas where current flow constantly changes direction. Vertical turbines also have the advantage of being able to be packed closer, therefore allowing for more devices in a given space. However, the vertical axis turbines usually experience additional drag as their blades rotate into the coming flow.

Researchers have been working on different designs of turbines with different numbers of blades and shapes hoping to enhance power generating efficiency (Guney and Kaygusuz, 2010). A common variation to enhance conversion efficiency of horizontal axis turbines is to add a duct or a shroud to the turbine (see Figure 2.3(c) for example). The duct part of the turbine has the ability to converge and accelerate the flow through a converging intake and thereby increase power generation. Lawn (2003) found out theoretically that ducted turbines can be 30% more efficient than non-ducted turbines. The earliest systematic research program on extracting ocean current energy from the Florida Current, the “Coriolis Program”, is based on a prototype design of a ducted turbine (Lissaman, 1979).

Another variation design under development is called “Aquantis C-plane”, designed by Aquantis, LLC, a company based in Santa Barbara, California (see Figure 2.3(d)). The C-Plane is moored to the ocean floor, and is designed with flight control and lift surfaces. Together with computer controls, the C-Plane will be able to adjust depth and position to find the optimum water velocity (Raye, 2002).

2.4.2 Ocean Energy Budget

To understand how much energy can be extracted, it is beneficial to first understand the general energy budget in the ocean circulation. The energy budget in the ocean can be determined from energy sources and sinks at the boundaries. A number of forces acting on the ocean are identified to be capable of generating an energy supply to the fluid, including (a) wind, (b) heating and cooling by the atmosphere, (c) exchange of fresh water with the

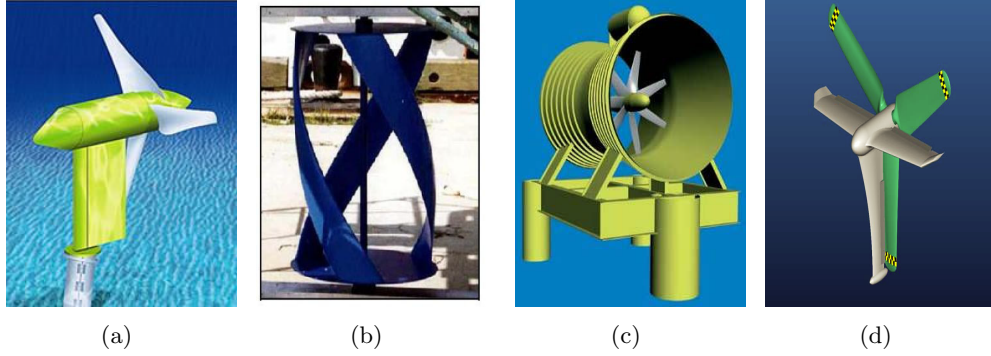


Figure 2.3: Examples of (a): horizontal axis turbine (Verdant Power); (b): vertical axis turbine (GCK Technology); (c): ducted turbine (Lunar Energy); (d): C-plane turbine (Aquantis, LLC)

atmosphere, (d) geothermal heating through the sea floor, (e) tides, and (f) atmospheric pressure loading. Figure 2.4 gives a general map of energy sources and sinks and energy transferring paths in the ocean system, although the numbers given in the figure bears a high level of uncertainty. It is suggested, with incomplete evidence, that the oceanic general circulation is governed by forcing from the wind field (Wunsch and Ferrari, 2004). Lueck and Reid (1984) estimated the net transfer of kinetic energy from the wind field to the ocean surface layer was between 7 and 36 TW, in which only a small portion went to large scale general circulation (Stern, 1975). The global value of wind power input into large scale ocean circulation from wind is estimated as 0.8 TW, with its majority going to the southern ocean (Wunsch, 1998). The remaining 20% (i.e. 160 GW) enters the northern ocean. Since the North Atlantic Ocean is only a portion of the entire northern ocean, the wind power input into the North Atlantic circulation is estimated to be under 100 GW.

Ocean energy potential can be associated with energy dissipation from the circulation. By relating the western boundary upwelling rate with basinwide energy dissipation through parameterization, the natural energy dissipation in the North Atlantic's western boundary current was estimated by Csanady (1989) to be

$$D_t/\rho_0 \approx 7 \times 10^7 \text{m}^5 \text{s}^{-3} \quad (2.3)$$

where D_t is the total energy dissipation in the western boundary current, and ρ_0 is the

(COET) in the Florida Atlantic University (FAU) started a research program aiming to assess the Ocean Current as a potential renewable energy resource. Researchers in FAU have conducted several investigations in quantifying hydrokinetic energy resources in the Florida Current. Based on power density calculation using computer model data, Duerr and Dhanak (2012) estimated the hydrokinetic resource in the Florida Current to be in the range of 20-25 GW, which is on the same order of magnitude with the estimation from ocean energy budget analysis. However, considering engineering constraints, the authors selected “realistic operating areas”, within which only 1-4 GW of power can be extracted.

Conversion efficiency represents the percentage of the kinetic energy flux that can be extracted. The Betz limit (Betz, 1926) is frequently quoted as the theoretical upper limit for energy extraction using turbines, which is about 59% (Khan et al., 2009). Betz efficiency was originally derived in regard to wind turbine efficiency, but is often leveraged as a limit for ocean turbine efficiency too. However, the assumptions Betz made in deriving the Betz efficiency (i.e. ideal rotor with infinite number of blades and incompressible flow) makes this number questionable in many circumstances. Another smaller efficiency limit of 35 % is proposed by Gorban et al. (2001). Garrett and Cummins (2004) calculated that the efficiency should be no more than 38 %. Typical values of underwater turbine conversion efficiency range from 0.35 to 0.5 (Myers and Bahaj, 2006).

This power density based approach is appropriate for preliminary estimates of energy resource potential. However, ocean current energy estimation based on undisturbed ocean power density has been challenged by Garrett and Cummins (2008). For a single or a small number of extracting devices, as long as there is negligible change to the existing flow, such estimation is reasonable. However, when large scale projects are planned, the flow will be reduced as more turbines are added, and the impact on the underlying flow from extracting devices can be critical.

Flow reduction can also incur other environmental consequences, which are still largely unknown. Many researchers have made their own speculations; Von Arx et al. (1974) suggested that a hypothetical array of turbines that extract more than 1 GW kinetic energy

from the Florida Current will seriously disrupt climatic conditions. However, another investigation based on several models, stated that extracting 10 GW of energy from the Florida Current will only cause the current to slow down about 1.2% and the temperature to go up about 10^{-5} °C, a modest influence (Lissaman, 1979).

2.4.4 Assessment Based on Dynamic Models

To incorporate the cumulative effect of reduced flow velocity due to the existence of extracting devices and better predict the amount of extractable energy resources, it is desirable to develop dynamic models, either analytical or numerical, to include that effect.

Garrett and Cummins (2005) have laid the theoretical foundation for a dynamic model of a channelled current flow that includes the effect of resistance due to extracting devices. The driving force in this model is the head difference between the entrance and exit of the channel, therefore, it is a perfect model for flows in tidal streams. However this model has difficulties when applied to the open ocean due to different physical natures. As for basin-wide ocean circulation, such as North Atlantic subtropical circulation, the flow is in quasi-geostrophic balance. Since the head difference is no longer the driving force, the Garrett and Cummins model is no longer applicable.

The quasi-geostrophic balance in the western boundary of the North Atlantic subtropical gyre is a result of the force balance between the pressure gradient, Coriolis effect, wind stress and friction. The power density $\frac{1}{2}\rho V^3$ only characterizes the kinetic energy transport by the flow, but not the generation rate of kinetic energy. The actual extractable rate of kinetic energy can only be estimated by solving models that characterize the quasi-geostrophic nature of the flow and include the impact from extracting devices.

Successful analytical models for assessing current energy potential in the Gulf Stream that include the cumulative effects from turbines presently do not exist. However, similar problems have been investigated for wind power assessment. Keith et al. (2004) used two different atmospheric circulation models to simulate the impact of large scale wind power extraction on the global climate with parameterization of additional drag due to wind turbines. Miller et al. (2011b) created a simple quasi-geostrophic balance model to

represent the dynamics of jet streams in the atmosphere, and evaluated the sensitivity of extractable wind energy with different installation capacities of wind turbines, and their climatic consequences. Miller et al. (2011a) took a different approach by establishing a simple momentum balance to estimate the maximum wind power extractability in the atmosphere and representing wind turbines with an additional friction coefficient.

Various numerical models for tidal currents that include the influence from extracting devices have been developed and tested for different areas. Bryden et al. (2007) evaluated the impact of energy extraction on tidal flow patterns using both analytical and numerical approaches. Sutherland et al. (2007) evaluated the maximum tidal power potential of Johnstone, BC, Canada using a 2-D numerical model (TIDE2D) with turbines simulated as increased drag. Shapiro (2011) did a case study for the Celtic Sea in UK to evaluate the effect of tidal stream power extraction on the regional circulation, and found out that the tidal farm can introduce noticeable changes to the circulation patterns as far as 100 km away from the farm. Defne et al. (2011) modeled tidal currents and effects of power extraction from tidal streams along the Georgia coast of the United States.

2.5 Motivation for Present Study

There are currently no coordinated studies available that provide a complete evaluation of extractable energy potential in the Gulf Stream considering effects of turbines. Past studies mainly focused on energy resource assessments for tidal currents. Although tidal currents and open ocean currents share obvious similarities, resource assessments are significantly different. Most importantly, tidal currents and open ocean currents have different dynamic mechanisms. Existing studies performing open ocean current energy resource assessments, such as the one by Duerr and Dhanak (2012), only consider the mean kinetic power density in a cross-section in the Gulf Stream and assume a fraction of that power is extractable. However, the theoretically recoverable energy resources in the open ocean currents are not directly associated with high current velocities, but governed by the dynamic mechanism of the general circulation system. The maximum extractable energy rate from the Gulf Stream can only be reasonably estimated if the interactions between turbines and the flow

regime are properly included. Other constraining factors including near field and far field effects on the flow and the environment from energy extraction also need to be evaluated. This study serves to fill in the gap and advance knowledge in this area.

CHAPTER III

CHARACTERIZING OCEAN CURRENTS IN THE UNITED STATES

Ocean currents vary greatly in terms of their dominating driving forces, spatial locations, and temporal and spatial scales. Due to this vast and complex nature of the ocean, there is presently no deterministic method for observing or predicting the entire range of ocean currents. Therefore, this study relies on numerical model data to characterize ocean currents because of its high resolution both temporally and spatially as well as its statistically significant duration (7 years). Measurements consisting of observational drifter data are available all over the ocean with adequate temporal resolution, and therefore are used to select the optimal model for regions where several model data are available.

3.1 Ocean Model Data Sources

3.1.1 Available Numerical Model Data

Most operational ocean models use data assimilation methods for improved accuracy of the predictions. Typically they incorporate satellite measurements of sea surface height and temperature as well as in-situ measurements of temperature and salinity profiles over depth. The numerical model data available include: Hybrid Coordinate Ocean Model (HYCOM) from the National Ocean Partnership Program (NOPP), the Navy Coastal Ocean Model (NCOM) from the Naval Research Laboratory (NRL) and the Regional Ocean Modeling System (ROMS) from the Jet Propulsion Laboratory (JPL) OurOcean Portal. Among them, HYCOM provides two versions of data, one with a global coverage (HYCOM Global) and the other covers the Gulf of Mexico (HYCOM GOM). The spatial coverage of the different models is shown in Figure 3.1 and summarized in Table 3.1.

HYCOM is a data-assimilative, hybrid isopycnal-sigma-pressure, primitive equation ocean circulation model that evolved from the Miami Isopycnic-Coordinate Ocean Model (MICOM) (Bleck, 2002; Halliwell, 2004). In the HYCOM online data server (<http://www.hycom.org>), two different sets of real-time modeling data are publicly available. One is

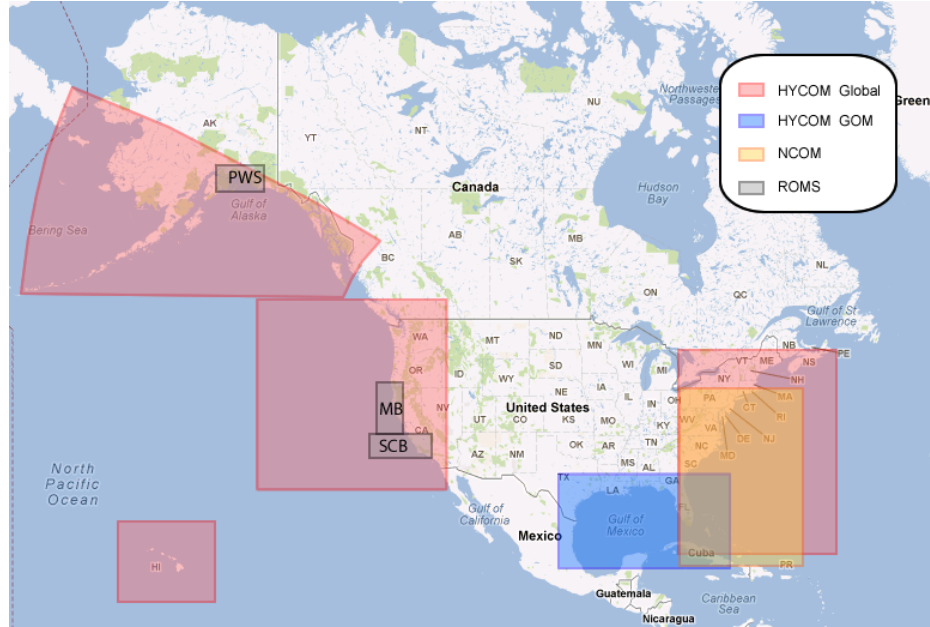


Figure 3.1: Spatial coverage of available ocean models.

Table 3.1: Summary of available numerical model data.

NAME	SPATIAL RANGE	TEMPORAL RANGE	RESOLUTION	TIME STEP
HYCOM Global	East, West & AK coasts	2004-2010	7 km	1 day
HYCOM GOM	Gulf of Mexico	2004-2010	4 km	1 day
NCOM	East US coast	2009-2010	3 km	1 day
ROMS JPL	SCB&WC&PWS	2008-2010	1-1.6 km	1 day

HYCOM-NCODA Global Analysis (GLBa), which has a global coverage, and the other is HYCOM-NCODA Gulf of Mexico Analysis (GOMa), which covers the Gulf of Mexico area only, but with a finer resolution. HYCOM-NCODA GLBa is configured on a Mercator grid between 78 S and 47 N with a 1/12 degree equatorial resolution. In the vertical, it has 32 layers. HYCOM-NCODA GLBa data are available from 2004 to present. The spatial coverage of HYCOM-NCODA GOMa extends from 18N to 32N in latitude and from 98W to 76W in longitude with a 1/25 degree equatorial resolution. In the vertical, it has 40 layers. HYCOM-NCODA GOMa data are available from 2003 to 2010.

NCOM is primarily based on the Princeton Ocean Model (POM) and the Sigma/Z-level Model (SZM). NCOM has free-surface and is based on primitive equations and the hydrostatic, Boussinesq, and incompressible approximations (Barron et al., 2006). The Mellor

Yamada Level 2 (MYL2) and MYL2.5 turbulence models are provided for the parameterization of vertical mixing (Rhodes et al., 2002). The Global NCOM nowcast data have 1/8 degree resolution, and a global coverage. The NCOM model data are not publicly available; however the NCOM data covering the East Coast for 2009-2011 has been obtained from the Naval Research Lab through personal communication.

ROMS is a three-dimensional, free surface, terrain-following numerical model that solves 3-D Reynolds-averaged Navier-Stokes equations (RANS) using hydrostatic and Boussinesq assumptions (Haidvogel et al., 2008). ROMS uses finite-difference approximations on a horizontal curvilinear Arakawa C grid (Duran, 1999) and vertical stretched terrain-following coordinates. JPL’s OurOcean Portal (<http://ourocean.jpl.nasa.gov/>) provides real-time ROMS ocean forecasting for the Southern California Bight (SCB), Monterey Bay (MB), and Prince William Sound (PWS) at resolution from 1 to 1.6 km.

3.1.2 Model Selection

The model selection process used the drifter data that is publicly available from the Global Drifter Program (GDP) (<http://www.aoml.noaa.gov/phod/dac/index.php>). The drifters consist of a surface buoy and a subsurface drogue approximately 15 m beneath the sea surface attached by a long tether. The satellite-tracked ocean drifters have been found to be one of the most economical means to provide near real-time current measurements (Venkatesh et al., 1990). Drifter data is available from 1987 to the present. A map of active drifter buoys around the world is shown in Figure 3.2. An example of drifter data from GDP is shown in Table 3.2.

Table 3.2: Example of drifter data from GDP.

ID	Month	Day	Year	Lat.	Lon.	VE	VN.	SPD.
				Deg	Deg	cm/s	cm/s	cm/s
7702986	9	6.5	2000	36.984	129.827	20.26	-0.43	20.26
7702986	9	6.75	2000	36.972	129.892	23.82	2.76	23.98
7702986	9	7	2000	36.994	129.943	39.14	31.58	50.29
7702986	9	7.25	2000	37.095	130.082	46.86	55.30	72.49

The drifter data are used to evaluate the performance of the different models. For a selected area, drifter data within that area were extracted, and numerical data from models

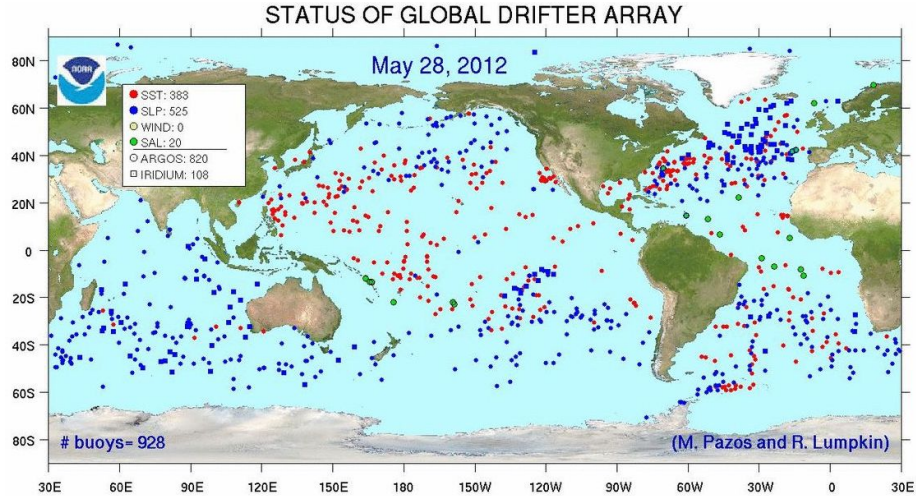


Figure 3.2: Status of global drifter arrays on May 28, 2012 (source: NOAA).

interpolated to corresponding locations and times. The model data have a fixed grid, and one snapshot of data is taken for each day. The drifter data are being collected by hundreds of drifter buoys, and one measurement is taken every 6 hours by an individual drifter which results in 4 available data recordings per day for each drifter. To make the model data and drifter data comparable, drifter data of different hours within a day are compared to the snapshot of the model data from the same day, and current velocities of model data are spatially interpolated to the location of the drifter data (see Figure 3.3).

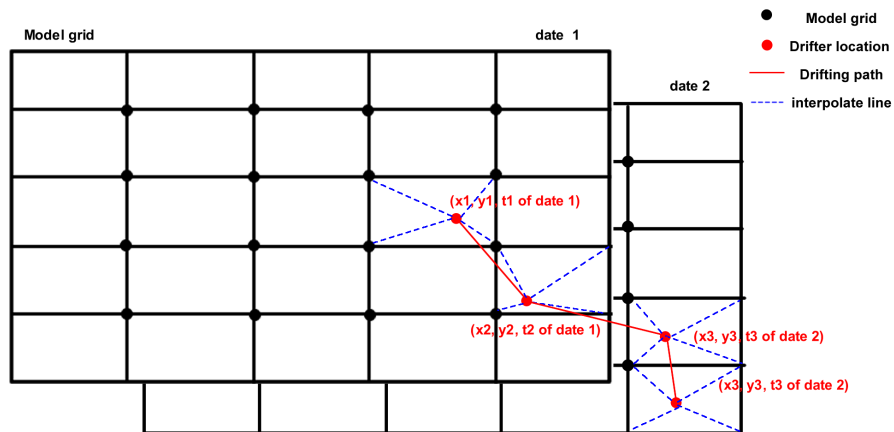


Figure 3.3: Comparing drifter data with interpolated model data.

Different model data covering the same region were compared in terms of their statistical agreement with the drifter data. Several statistical metrics were calculated and a score

suggested in personal communication with Dr. Fabrice Bonjean from SAT-OCEAN (<http://www.sat-ocean.com>) was used to assess the overall performance of each model. The statistical metrics of the velocity comparison include mean difference

$$MD = \frac{1}{N} \sum_{k=1}^N (U_{model}^k - U_{drifter}^k) \quad (3.1)$$

RMS differences

$$RMSD = \sqrt{\frac{1}{N} \sum_{k=1}^N (U_{model}^k - U_{drifter}^k)^2} \quad (3.2)$$

relative standard deviation differences

$$RDSTD = \frac{STD(U_{drifter}) - STD(U_{model})}{STD(U_{drifter})} \times 100 \quad (3.3)$$

and correlation

$$COR = \frac{COV(U_{drifter}, U_{model})}{STD(U_{drifter})STD(U_{model})} \quad (3.4)$$

where U_{model} is the current speed from models and $U_{drifter}$ is the current speed from drifter measurement, STD is the standard deviation and COV is the covariance. MD and $RMSD$ are typical statistical metrics. $RDSTD$ characterizes the difference of variability around the mean between the model and the measurement data, and COR characterizes the tendency in the linear relationship between the model data and the measurement. A metric named $SKILL$ is directly related to $RMSD$ and is given as

$$SKILL = 1 - \frac{RMSD}{\sqrt{\frac{1}{N} \sum_{k=1}^N U_{drifter}^k{}^2}} \quad (3.5)$$

Since $0 < 1 + COR < 2$, $1 + SKILL < 2$, and $1 + \left| \frac{RDSTD}{100} \right| > 1$, a convenient $SCORE$ number (ranges between 0 and 10) that characterizes the agreement between the model data and the measurement data by combining the different statistics is used:

$$SCORE = \frac{(1 + COR) \times (1 + SKILL)}{1 + \left| \frac{RDSTD}{100} \right|} \times 2.5 \quad (3.6)$$

The greater the SCORE number, the better the model data is in predicting the measurement.

The U.S. coast was broken up into individual regions and based on the evaluation of the statistics for each region the best performing model for that region was selected. On the

west and Alaska coasts, regions with more than one model data source available include the Southern California Bight (SCB), Monterey Bay (MB), and Prince William Sound (PWS) as shown in Figure 3.1. The statistical comparison for these 3 regions shows that HYCOM data has a better statistical agreement with measurements and therefore is selected for all 3 regions (Table 3.3).

Table 3.3: Statistical comparison results for the west and Alaska coasts.

Name	Model	MD	RMSD	RDSTD	COR	SKILL	SCORE
		m/s	m/s				
SCB	HYCOM	0.03	0.12	23.46	0.19	0.38	3.31
	ROMS	-0.06	0.17	-26.84	0.09	0.07	2.32
MB	HYCOM	-0.05	0.14	-43.13	0.22	0.13	2.41
	ROMS	-0.04	0.15	-86.95	0.31	0.03	1.80
PWS	HYCOM	0.25	0.29	39.87	0.60	0.34	3.83
	ROMS	0.20	0.27	32.77	0.36	0.38	3.54

The east coast is broken down into 9 subregions shown in Figure 3.4 (E1-E9). For the region of the Florida Current (E1-E3), three sets of model data (Global HYCOM, HYCOM GoM and NCOM) are available and are compared with each other in terms of their statistical agreement with the measurement. The statistical comparison results are summarized in Table 3.4 and the direct comparison results are shown in Appendix A. For the Florida Current region, HYCOM GoM data has a better statistical agreement with the measurement and also a higher resolution than the other two dataset. Therefore HYCOM GoM is selected for the Florida Current region (E1-E3). For a portion of the East coast (E4-E9), both HYCOM-Global and NCOM were selected. Because NCOM only contained 2 years of data, 5 additional years from the HYCOM were included. The selection of different model data for different regions of the coastline is summarized in Table 3.5. SCORE numbers are generally higher for the east coast (Table 3.4) than for the west coast (Table 3.3) since the current velocity is generally higher on the east coast than the west coast which results in better signal to noise ratio on the east coast.

3.2 Variability of the Florida Current

The GIS map of mean surface current speed and power density already shows that the Florida Current has the highest power density ($> 2500\text{W}/\text{m}^2$) along the United States

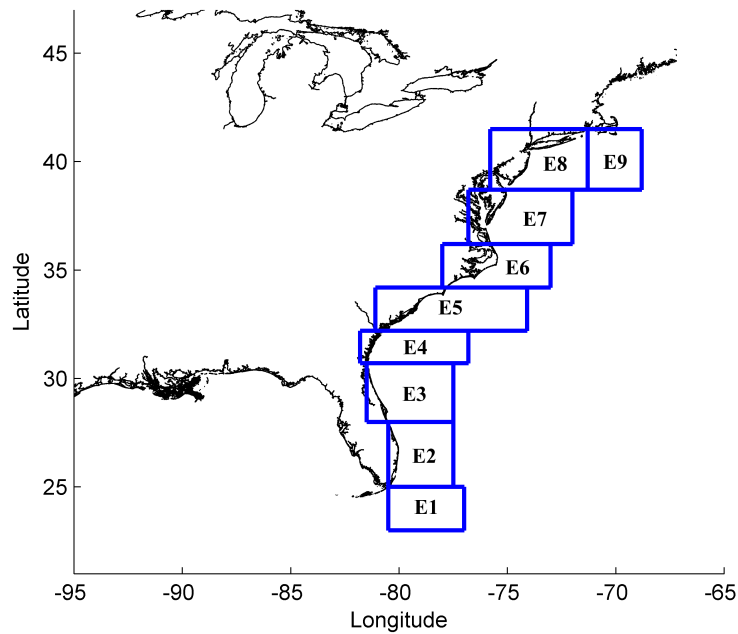


Figure 3.4: Division of east coast area into E1-E9 sub-regions.

coasts (Figure 3.5). Furthermore, the proximity of the Florida Current to the southeastern Florida metropolitan area (< 50km) makes extracting renewable energy from ocean currents in this region particularly attractive for local electricity needs. Therefore, this subsection presents an analysis of the variability of ocean currents in the Florida Current.

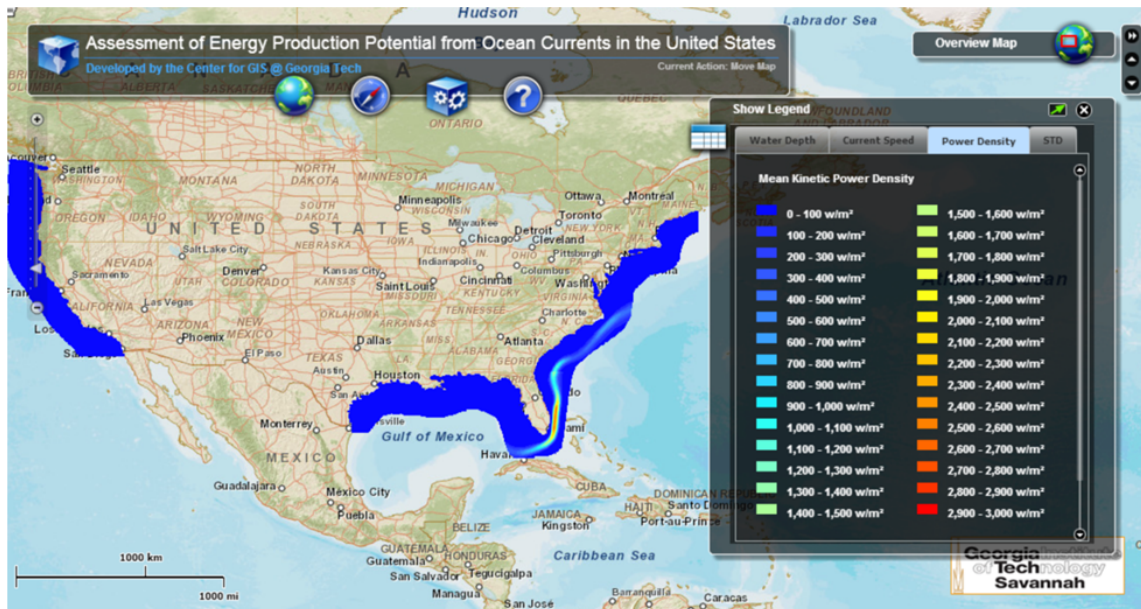


Figure 3.5: GIS map showing the mean surface current power density for the U.S. coast.

Table 3.4: Statistical comparison between models for the east coast

Name	Model	MD	RMSD	RDSTD	COR	SKILL	SCORE
		m/s	m/s				
E1	HYCOM Global	0.096	0.313	24.251	0.757	0.520	5.375
	HYCOM GoM	0.016	0.234	11.764	0.773	0.498	5.939
	NCOM	0.056	0.297	28.301	0.801	0.599	5.609
E2	HYCOM Global	0.146	0.328	22.767	0.831	0.575	5.873
	HYCOM GoM	0.068	0.276	19.075	0.854	0.631	6.351
	NCOM	0.072	0.336	16.903	0.789	0.566	5.992
E3	HYCOM Global	-0.017	0.462	29.326	0.339	0.273	3.295
	HYCOM GoM	0.029	0.320	30.506	0.700	0.485	4.834
	NCOM	0.028	0.368	33.551	0.575	0.405	4.141
E4	HYCOM Global	0.098	0.451	32.604	0.577	0.431	4.255
	NCOM	0.084	0.449	29.450	0.570	0.428	4.329
E5	HYCOM Global	0.060	0.440	25.786	0.413	0.405	3.946
	NCOM	0.029	0.402	19.986	0.534	0.460	4.666
E6	HYCOM Global	0.018	0.560	32.525	0.376	0.419	3.684
	NCOM	-0.054	0.448	33.123	0.645	0.530	4.728
E7	HYCOM Global	0.119	0.549	37.680	0.591	0.445	4.175
	NCOM	0.090	0.497	26.462	0.689	0.499	5.005
E8	HYCOM Global	0.039	0.153	-46.255	0.368	0.552	3.628
	NCOM	0.106	0.146	13.262	0.458	0.572	5.057
E9	HYCOM Global	0.232	0.438	77.791	0.090	0.323	2.028
	NCOM	-0.004	0.200	-12.636	0.877	0.690	7.039

Table 3.5: Ocean model data chosen for different areas

Location	Selected Model
East Coast (E4-E9)	HYCOM Global (5yrs) & NCOM (2yrs)
Florida Strait (E1-E3)	HYCOM GoM (7yrs)
Gulf of Mexico	HYCOM GoM (7yrs)
West and Alaska Coasts	HYCOM Global (7yrs)
Hawaii	HYCOM Global (7yrs)

The telecommunication cables that run almost perpendicularly through the Florida Strait from West Palm Beach, FL to Eight Mile Rock, Grand Bahamas Island are used to measure the volume transport through the current channel. This measurement is based on the working principle that the flow through the earth's magnetic field can induce a voltage in the cable, which after calibration, can measure the volumetric flow (Larsen and Sanford, 1985). The volume flux from the cable data is a useful data resource which can be explored to determine the possible relations between volume flux and kinetic energy flux in the Gulf Stream. The long cable data measurement record (from 1982 to present) provided by the Atlantic Oceanographic and Meteorological Laboratory of NOAA is extremely valuable. Figure 3.6 shows the comparison of the 30-day running averaged volume flux in the Florida

Current between two versions of HYCOM model data and the submarine cable measurement. The mean volume flux is 31.6 Sv for HYCOM GoM and 25.0 Sv for Global HYCOM. The mean volume flux from cable measurement is 31.3 Sv. Apparently the HYCOM GoM data predicts the mean volume flux in the Florida Current fairly accurately while the Global HYCOM data underestimates the volume flux by about 15%. In addition, the correlation coefficient between HYCOM Global and the cable measurement is about 0.68, and the correlation between HYCOM GoM data and cable measurement is about 0.77, indicating a high linear correlation. The vertical current speed profile averaged over one-year period of record from HYCOM GoM data is compared with ADCP data provided by the Southeast National Marine Renewable Energy Center located at Florida Atlantic University for the same period of time in terms of the mean, minimum and maximum current speed, and a high level of agreement is also observed as shown in Figure 3.7. A more detailed validation of the HYCOM model is provided by Neary et al. (2012).

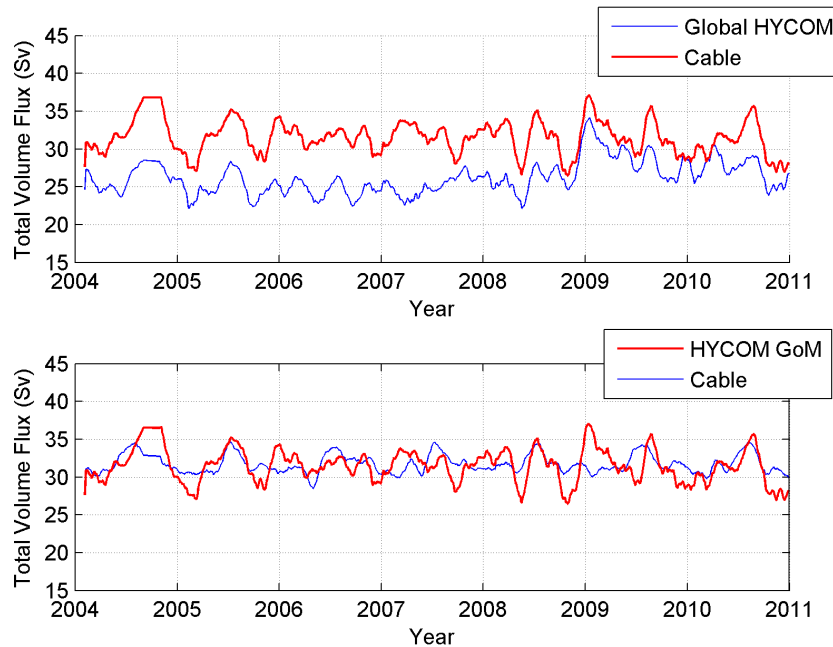


Figure 3.6: Comparison of 30-day running averaged volume flux in the Florida Current between cable measurement and two versions of HYCOM data: (a) Global HYCOM and (b) HYCOM GoM.

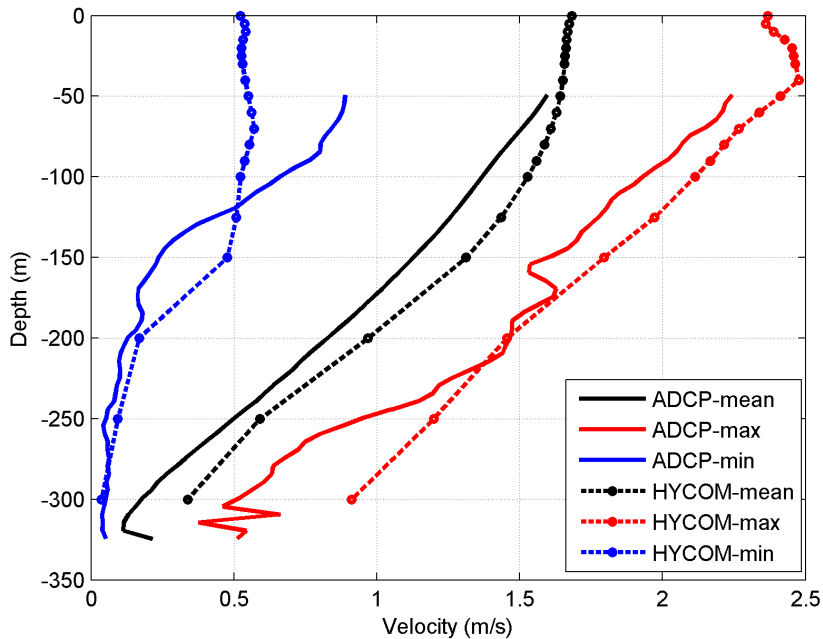


Figure 3.7: Comparison of one-year averaged vertical current speed profiles between ADCP measurement and HYCOM GoM data located at approximately (26.07N, 79.84W).

The spatial variation of the Florida Current was investigated by examining the distributions of the mean and standard deviation (STD) of the current speed on the ocean surface as well as in a vertical cross-section plane. The mean current speed is a proxy for the average kinetic power density since kinetic power is proportional to cubed current speed while STD represents the temporal variation of the power potential. In order to extract stable and sustainable kinetic energy from ocean currents, a high level of kinetic power coupled with a low level of temporal variation is desired. In the Florida Strait, the Gulf Stream (i.e. the Florida Current) is predominantly flowing northward as shown in Figure 3.8. The core of the current where the flow is the strongest is concentrated within about 200 m of the surface layer and spans about half of the width of the channel as seen in Figure 3.9. The core of the Florida Current is slightly offset to the west of the channel centerline, reducing the potential cost of transmitting extracted power to shore, assuming extraction devices are to be deployed near the core of the current flow. Figure 3.8b and 3.9b show the Florida Current has the greatest temporal variation close to the Florida shoreline on the edge of the core of the strongest current. Comparing daily and monthly snapshots of the current speed

distribution shows the high variation near the edge as a direct result of the meandering and seasonal broadening of the core of the current flow. The coefficient of variation, which is the ratio of standard deviation to the mean, shows a low level of variability inside the core of the current and relative high variability outside the core (Figure 3.8c and 3.9c). As the current flows downstream past the Florida Strait, its variability increases, partly due to the decrease of geographical constraint from the coastline and bathymetry.

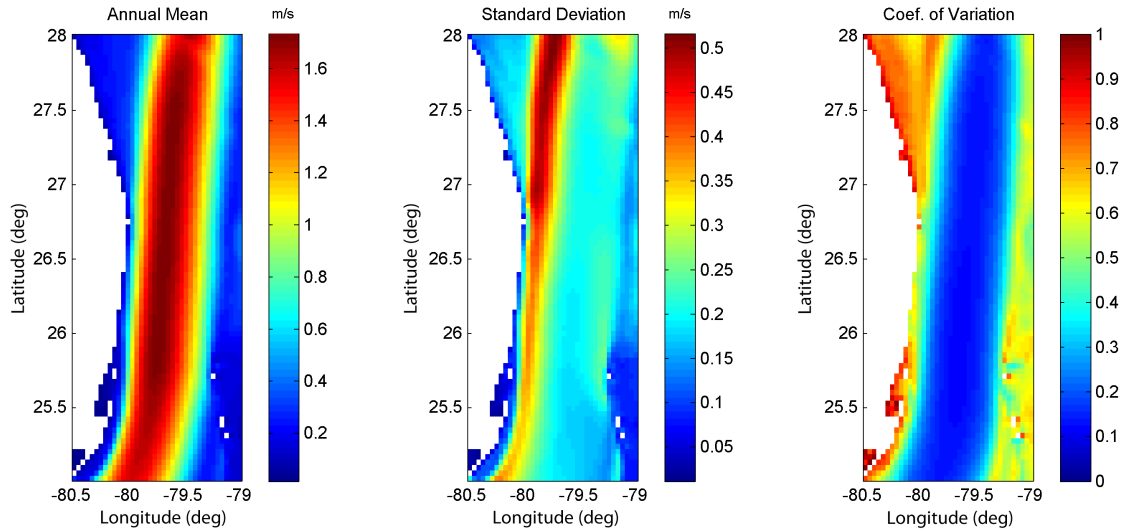


Figure 3.8: Distributions of (a) annual mean surface current speed, (b) standard deviation, and (c) the coefficient of variation in the Florida Current.

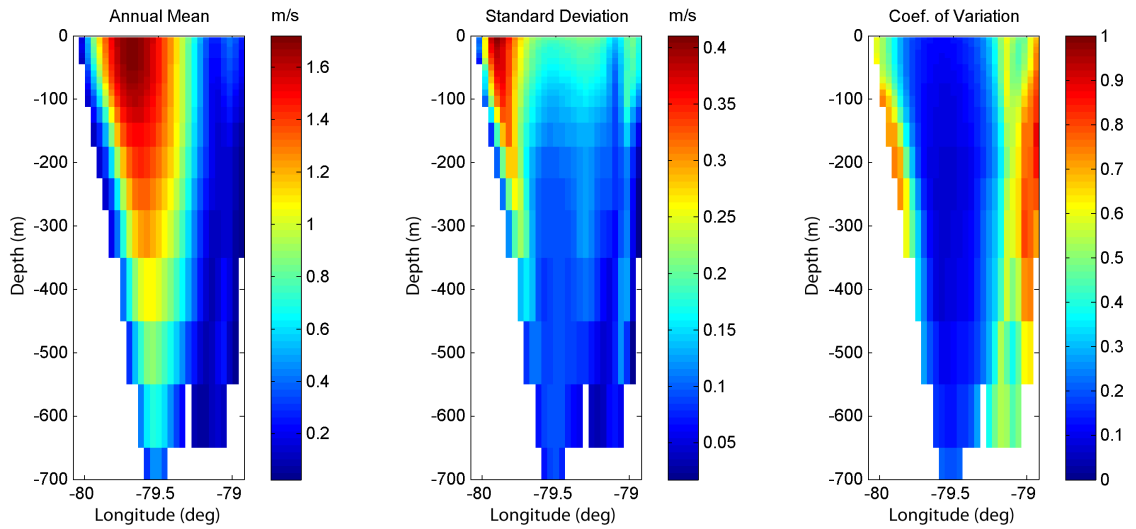


Figure 3.9: Cross-sectional distributions of (a) annual mean current speed, (b) standard deviation, and (c) the coefficient of variation in Florida Current at the latitude of 26.6264N.

3.3 Kinetic Energy Flux in the Florida Current

3.3.1 Characterizing Kinetic Energy Flux in the Florida Current

Kinetic energy flux is a primary indicator of undisturbed kinetic energy reserve in ocean currents. The kinetic energy flux E_f through a vertical section in the Florida Current can also be integrated from HYCOM data as

$$E_f = \frac{1}{2}\rho \int |\vec{V}|^2 \vec{V} \cdot d\vec{A} \quad (3.7)$$

where ρ is the water density, \vec{V} is the velocity vector and $d\vec{A}$ is the differential vertical area. Figure 3.10 shows the time series of calculated kinetic energy flux in the Florida Current from 2004 to 2010. The mean level of energy flux in the Florida Current is approximately 22.6 GW with apparent variability at multiple time scales, from weeks to years.

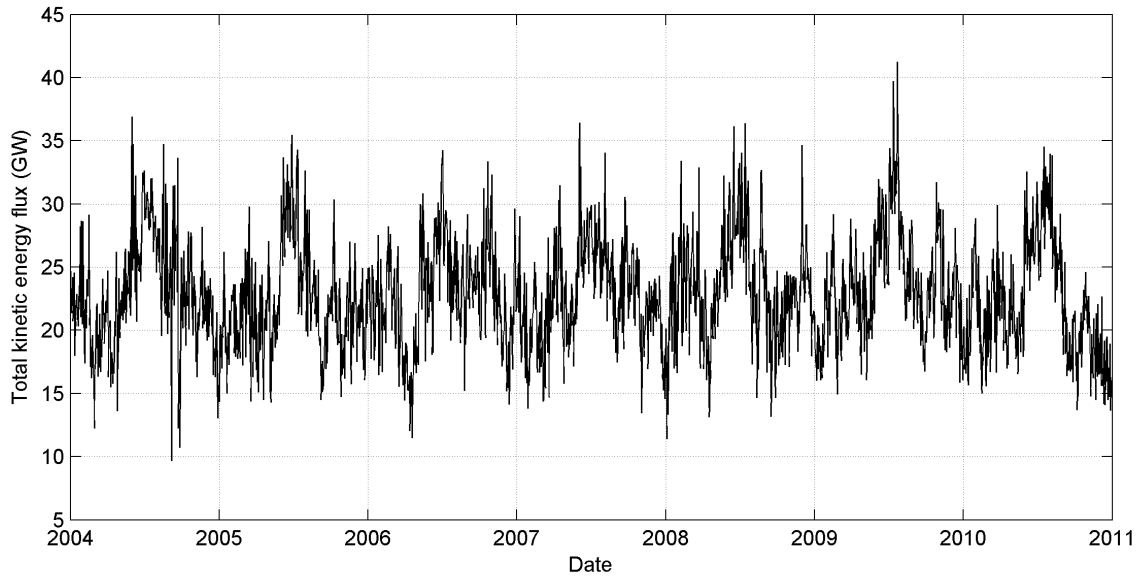


Figure 3.10: Time series of total kinetic energy flux in the Florida Current.

Figure 3.11 shows the annual mean kinetic energy flux for years from 2004 to 2010. It is observed that the annual mean kinetic energy flux is fairly constant over the years. Within each year, the standard deviation varies slightly and the mean standard deviation is approximately 4.3 GW. The variation throughout the year is evident from the monthly averages and STD of kinetic energy flux as shown in Figure 3.12. The months in summer time feature the highest energy flux of the year, greater than 27 GW. Energy fluxes in other

months are much lower and are mostly in the range between 20 and 23 GW. However the standard deviations for different months have a more random pattern with no observable regularity, and are all in the range between 3 and 4 GW. This indicates that the total available kinetic power can vary greatly on a monthly basis.

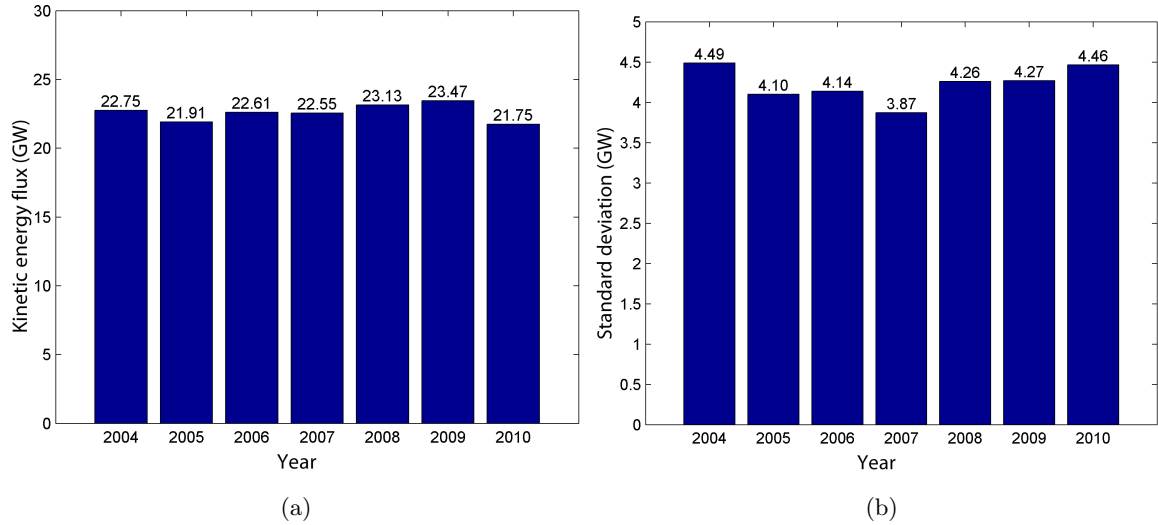


Figure 3.11: Yearly variation of (a) mean kinetic energy flux and (b) standard deviation in the Florida Current from 2004 to 2010.

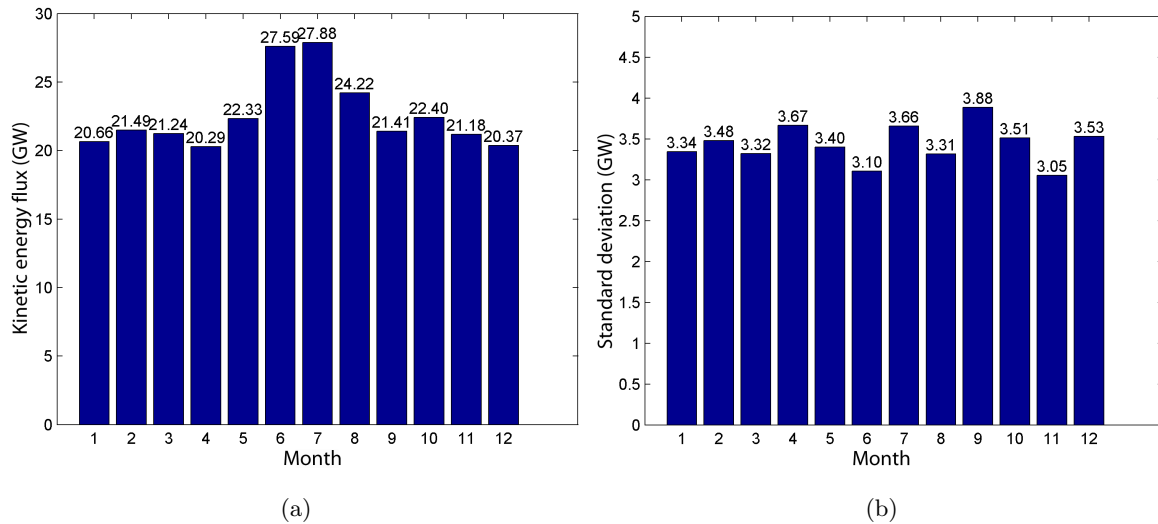


Figure 3.12: Monthly variation of (a) mean kinetic energy flux and (b) standard deviation in the Florida Current.

To quantify the change of kinetic energy flux with depth, it is helpful to examine the change of energy flux at different depths by integrating model data only across the channel (from approximately 80.08 W to 78.93 W in longitude) but not over depth. Figure 3.13 shows the kinetic energy flux density (GW/m) as a function of the depth for 4 different months along with the annual mean. The general shape of the curves is similar to the vertical profile of current speed with the highest value near the surface and lowest near the bottom. But these profiles are quantitatively different from vertical velocity profiles. It is seen that more than half of the total energy flux is concentrated in the upper 200 m of the water column. Strong monthly variability is prevalent in the upper 100 m of water column. The month of July features the highest level of energy flux while November has the lowest. February and May have flux levels that are relatively close to the annual mean. Below 100 m monthly variability becomes negligible. It implies the monthly variability mostly results from surface momentum flux variation.

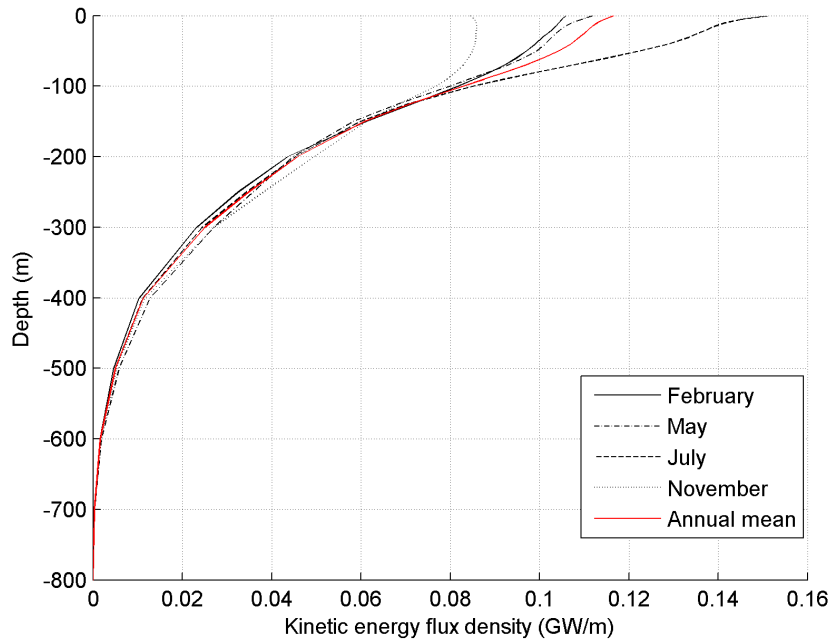


Figure 3.13: Vertical kinetic energy flux density in the Florida Current for selected months (Feb., May, Jul., and Nov.) and annual mean.

3.3.2 Estimating 30 Years of Kinetic Energy Flux

The HYCOM model provides 7 year of data that can be used to calculate both volume flux and kinetic energy flux in the Florida Current. Kinetic energy flux is of greater interest since the purpose of this study is associated with estimating power potential from ocean currents. Therefore a solid relationship between volume flux and kinetic energy flux is sought so that longer record of kinetic energy flux can be projected based on 30 years of historical volume flux data from cable measurement with some level of confidence. In order to test the robustness of this approach, the 7 years of HYCOM data was divided into two groups. One group extends from 2004 to 2006 and the second group extends from 2007 to 2010. The second group of data is used to establish an empirical statistical relationship between volume flux and energy flux in the Florida Current. The volume and kinetic energy flux of 2007-2010 are plotted in Figure 11a. The statistical relationship is established with a least square fit for the following equation

$$E_f = aQ^n \tag{3.8}$$

with coefficients a and n to be determined. The fitted curve is shown in Figure 3.14b where the fitted values of coefficients are $a = 0.001592$, and $n = 2.766$ with correlation coefficient $R^2 = 0.72$.

To test the robustness of this statistical relationship, the volume flux data of 2004-2006 from the cable measurement is used as input of the above empirical relationship. A time series of predicted kinetic energy flux is therefore generated as the output. For comparison, the kinetic energy flux of the same period of time is also calculated from HYCOM model data. Figure 3.15a shows the time series of kinetic energy flux from both the HYCOM model data and from the prediction by cable data. A low pass filter is applied to both signals for smoothness and the result is shown in Figure 3.15b. Some months of cable data are missing, and therefore result in a number of gaps in the red curve. The comparison between the calculated kinetic energy flux from HYCOM (blue) and the projected kinetic energy flux from cable data (red) in Figure 3.15 features a correlation coefficient of approximately 0.7.

This experiment verifies the robustness of the statistical approach of predicting kinetic

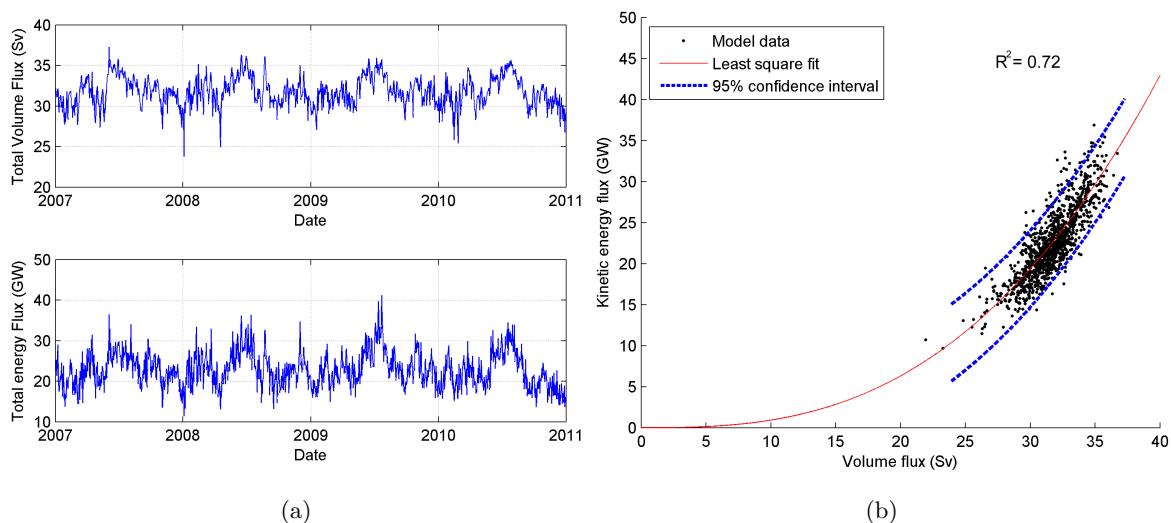


Figure 3.14: (a) Least square fit of the relationship between volume and kinetic energy flux with 95% confidence interval from 2004 to 2010, and (b) projected 30-year low-pass filtered time series of kinetic energy flux based on historical cable data with 95% confidence interval.

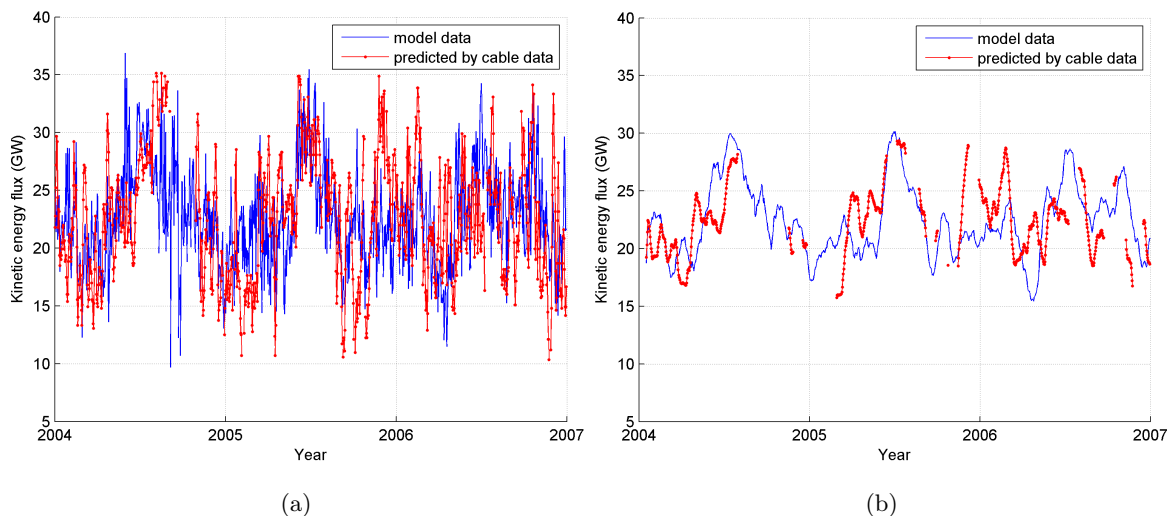


Figure 3.15: Predicted kinetic energy flux from 2004 to 2006 from cable data with the energy flux calculated from HYCOM model data: (a) time series of daily data, and (b) 30-day running averaged time series.

energy flux from volume flux from cable measurement. Therefore, a new and more reliable relationship between volume flux and kinetic energy flux in the Florida Current is computed

based on 7 years of HYCOM data with a correlation coefficient $R^2 = 0.75$ (Figure 3.16):

$$E_f = 0.001598 Q^{2.764} (GW) \quad (3.9)$$

The 30-year time series of kinetic energy flux with low pass filtering is then calculated and plotted in Figure 3.17 together with 95% confidence interval. The predicted mean kinetic energy flux from 30 years of cable data is about 22.8 GW. The standard deviation is about 5.4 GW.

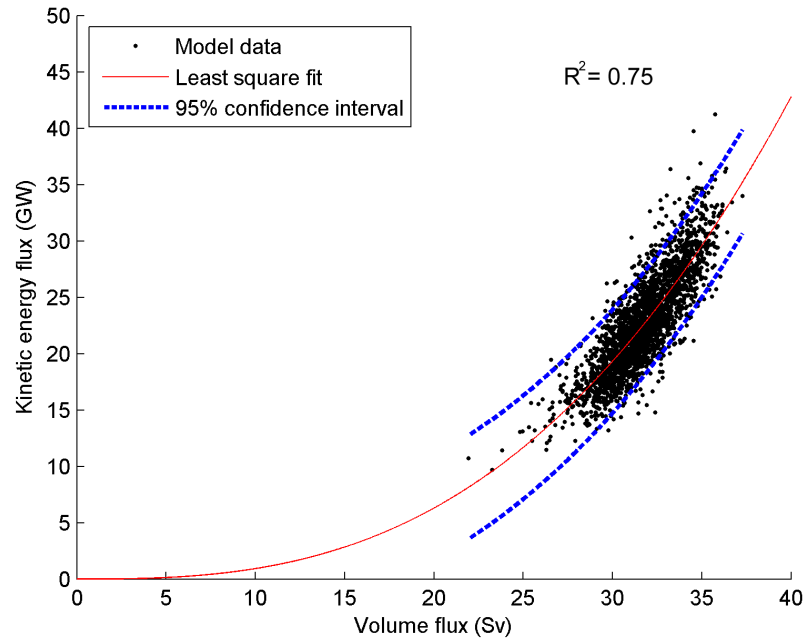


Figure 3.16: Least square fit of the relationship between volume and kinetic energy flux with 95% confidence interval from 2004 to 2010.

Both monthly and yearly variations of kinetic energy flux mean and STD can also be computed based on 30 years of data, as shown in Figure 3.18 and 3.19. It is observed that the mean kinetic energy flux is still the highest in the summer, particularly in July where the peak occurs. The lowest mean energy flux occurs in November, which is in agreement with previous findings. In addition, this data set suggests that the standard deviation is lowest during the summer months when the average power is the highest. The kinetic energy flux also shows very strong year to year variability. The annual mean power ranges as high as 27 GW in 2002, and as low as 18 GW in 1991.

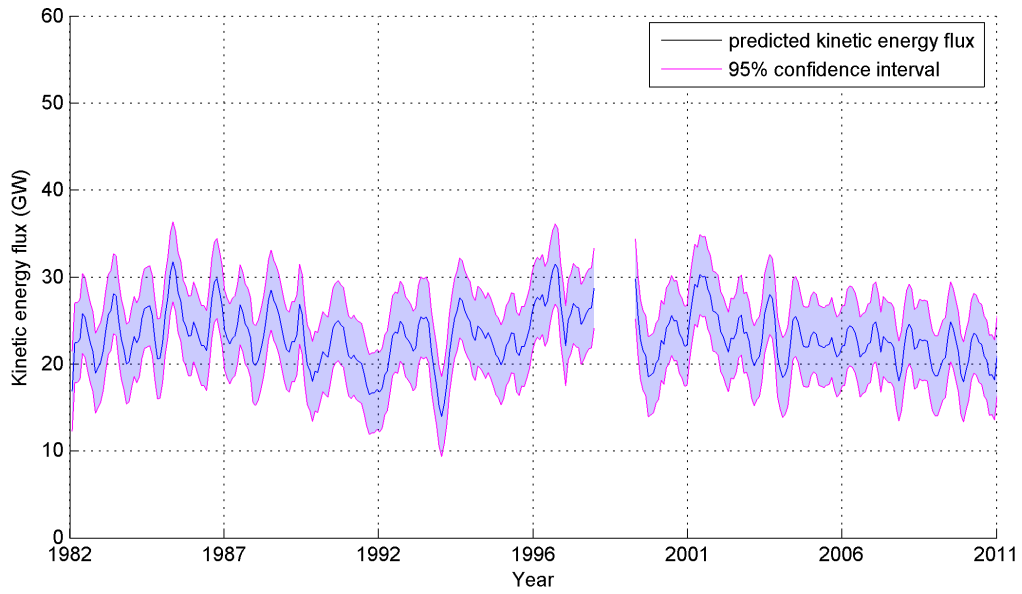


Figure 3.17: Projected 30-year low-pass filtered time series of kinetic energy flux based on historical cable data with 95% confidence interval.

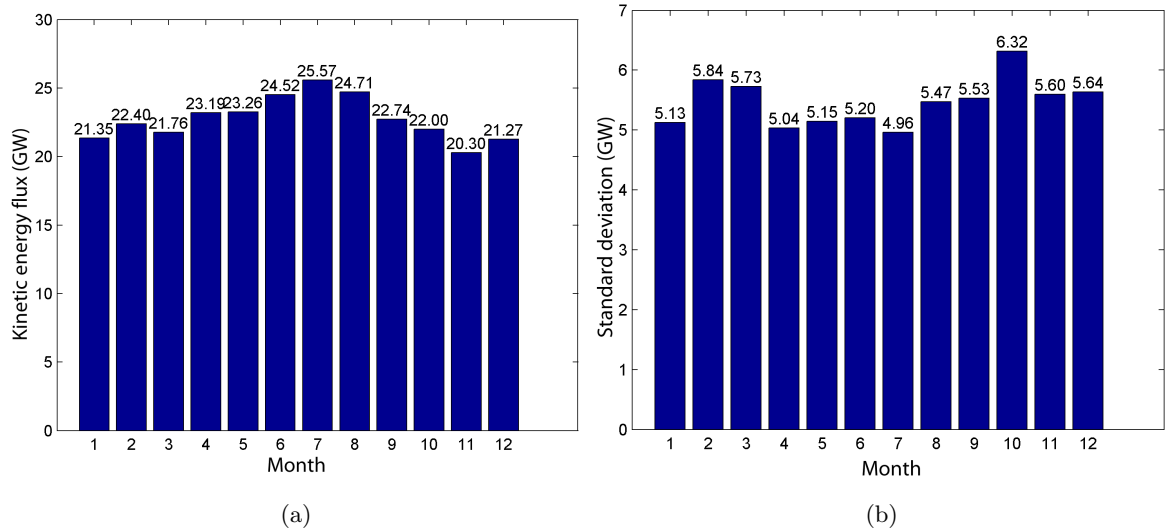


Figure 3.18: Monthly variation of (a) mean kinetic energy flux and (b) standard deviation in the Florida Current based on projected 30 years of kinetic energy flux data.

3.4 Dissemination of Data

An interactive web-based interface has been created by the Georgia Tech GIS center with the GIS database developed from this study to facilitate dissemination of the ocean current

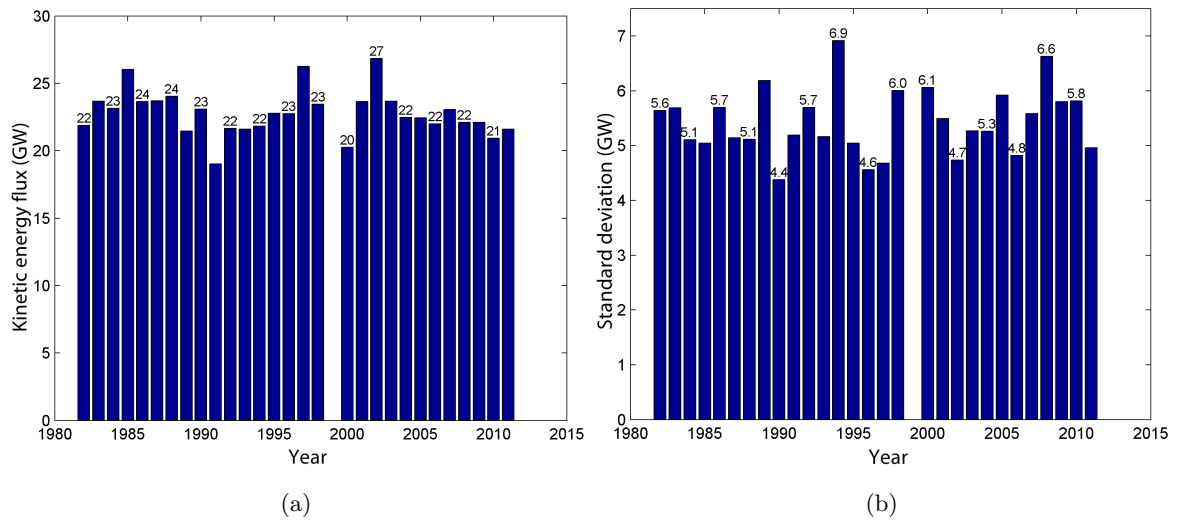


Figure 3.19: Yearly variation of (a) mean kinetic energy flux and (b) standard deviation in the Florida Current based on projected 30 years of kinetic energy flux data.

data to interested users, including electric power utilities, policy makers, regulators and turbine manufacturers. The webpage can be accessed at: <http://www.oceancurrentpower.-gatech.edu/>. The GIS tools allow the user to interact with the ocean current database. The project data is stored in a geodatabase that enables the search query function via a rich internet application (RIA) supported by ArcGIS server. Users can interact with the map using the pull down menus or widgets on the right of the screen. Besides the map navigation functions, the RIA also enables the users to identify the source data to retrieve the ocean current information for the given location and export the selected data specified by the user. This system provides the following capabilities:

- GIS layers and map displays of the monthly and yearly mean currents and power densities.
- Provide the velocity probability distributions along the U.S. coastline at different depths.
- Download monthly and yearly mean surface current velocity and power density for particular regions.

This website is functionally designed similarly to the tidal energy website (<http://www.-tidalstreampower.gatech.edu/>) documented by Defne et al. (2012). However, based on the experience learned from operating that website, key components were modified as described below to enhance the technical capabilities.

Data layers

The web page consists of multiple layers (a data points layer and a set of color mapped raster layers) that can be turned on and off with the data layers widget. The color mapped raster layers include the water depth, the mean current speed for each month and the total and the mean kinetic power density (for example Figure 3.20). These layers are generated by interpolating the model results from computational grids onto an ArcGIS raster grid and are useful for a quick visual examination. On the other hand, the data point layer contains more detailed information that corresponds to actual model grid points and can be queried through the interactive tools, and is therefore more suited for in-depth analyses.

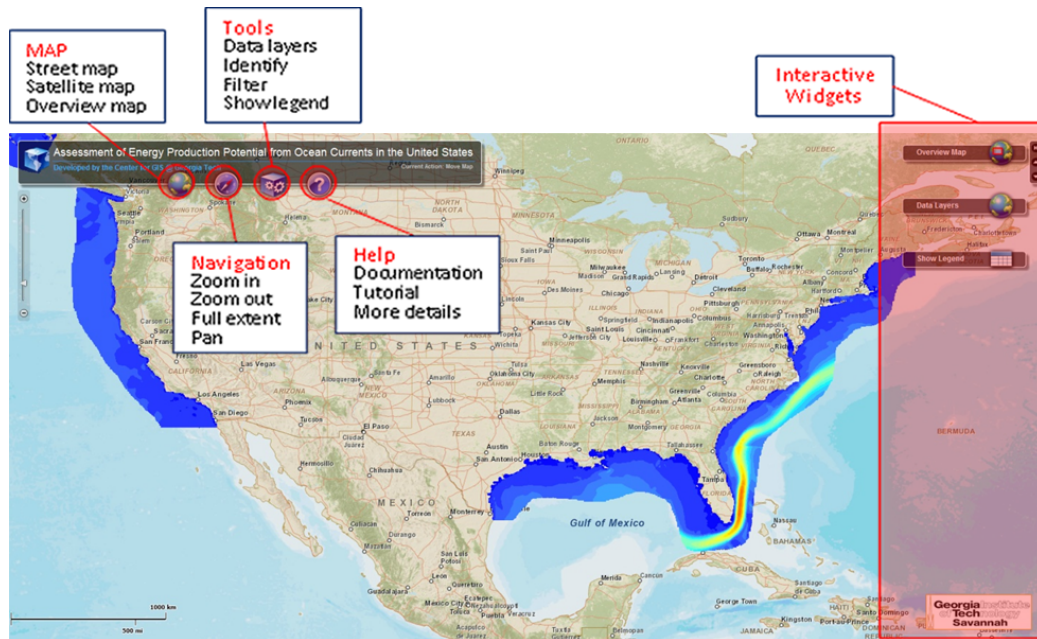


Figure 3.20: GIS map of mean surface ocean current speed with pull down menus on the top and interactive widgets on the right.

Identify tool

This tool is used to identify a single data point either by clicking on the map or by specifying a longitude and latitude. The identify tool returns the model water depth, mean

current speed, mean kinetic power density and the exact longitude, latitude of the selected point. It also shows the vertical current speed profiles for the selected point (for example Figure 3.21). Both joint and marginal histograms for ocean current velocity at a selected point can be plotted for any specific month or the entire year using the identify tool (for example Figure 3.22). These histograms facilitate an overview of the probabilistic nature of the ocean current resource at a location. Similarly, vertical current speed profiles at selected locations can also be plotted with the identify tool.

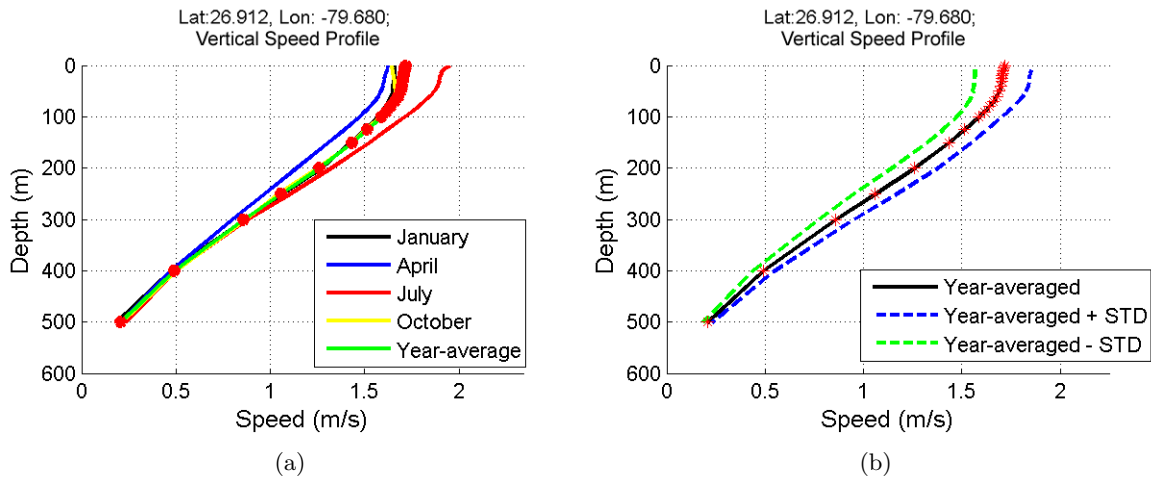


Figure 3.21: Example figures of vertical current speed profiles for location (26.912N, 79.680W): (a) monthly variation and (b) standard deviation.

Filter tool

The filter tool is used to download data at selected grid points. A single point or multiple points can be selected using the filter tool by dragging a window or selecting by polygon. The selected data can be filtered based on the water depth, mean current magnitude or mean power density or a combination of them prior to downloading. This provides the user with the option to only include the areas that meet certain criteria, such as a minimum depth or a minimum speed. The selected data is exported to a spreadsheet and for each point it includes display geographical coordinates, the modeled depth, monthly and annual mean surface current speed, current speed standard deviation and mean power density. Based on the users experience and reflection on the previous tidal stream project, there

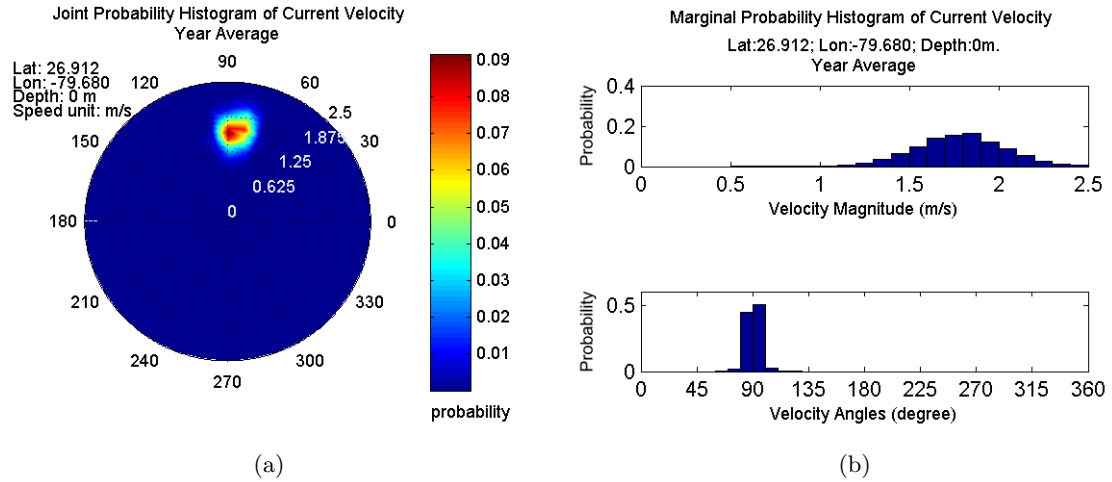


Figure 3.22: Example figures of (a) joint and (b) marginal probability distributions of surface current velocity for (26.912N, 79.680W).

was a bottleneck when exporting the data selected by the users. The solution in the tidal stream project was based on ArcGIS server search query function. When a large volume of data is queried, it has to loop through each feature to retrieve the individual values and re-format the data into a tabular format downloadable as a spreadsheet. To improve the performance of the export function, a SQL Server database was created that stores a copy of the non-spatial tabular data in the geodatabase. A REST Web service was developed through Visual Studio .NET that executes a SQL transaction to implement the search query over the SQL Server database to generate the output spreadsheet. The response time is significantly reduced in this approach.

3.5 Data Probability Uncertainty

The GIS website developed in this project enables the user to select location and provides the probability distribution of current velocity and direction from the database. The distributions are calculated based on 7 years of daily snapshot data, and therefore contains uncertainty that needs to be addressed with a confidence interval.

The probability distribution of current speed shows the chances of current speed in corresponding intervals. In general, the estimator of proportion in each interval \hat{p} is given by

$$\hat{p} = \frac{X}{n} \quad (3.10)$$

where X is the number of elements in the interval, and n is the total number of elements. When n is large, the sample proportion \hat{p} is well approximated as normal with mean \hat{p} and standard deviation $\sqrt{\frac{\hat{p}(1-\hat{p})}{n}}$ (Johnson, 2006). Therefore a confidence interval for \hat{p} is given by

$$\left(\hat{p} - z_{\alpha/2} \sqrt{\frac{\hat{p}(1-\hat{p})}{n}}, \hat{p} + z_{\alpha/2} \sqrt{\frac{\hat{p}(1-\hat{p})}{n}} \right) \quad (3.11)$$

where $z_{\alpha/2}$ denotes the upper $\alpha/2$ point of the standard normal distribution. For a 95% confidence interval, $\alpha=0.05$, $z_{\alpha/2} = 1.96$ and using 7 years of daily data, $n \approx 7 \times 365 = 2555$. Defining $\gamma = z_{\alpha/2} \sqrt{\frac{\hat{p}(1-\hat{p})}{n}}$, γ can be computed as a function of probability \hat{p} , as shown in Figure 3.23a. For example, Figure 3.24a shows the probability of ocean current speed at (26.912E, 79.600W). For a certain speed value (e.g. ~ 1.52 m/s), there is a corresponding probability p' (0.06) as marked by the green dash line in Figure 3.24a.

In Figure 3.23a, $p'=0.06$ corresponds to a value of $\gamma' \approx 0.0095$. Therefore the confidence interval for $p'=0.06$ is approximately $(p' - \gamma', p' + \gamma')$ or $p'(1.52m/s) = 0.06 \pm 0.0095$. The red dashed lines in Figure 3.24a shows the 95% confidence interval for the probability distribution of the current speed. Similarly, for the monthly probability histograms estimated from 7 years of data, the total number of elements $n \approx 7 \times 30 = 210$. The procedure to obtain 95% confidence interval of the probability is the same, but a different curve for the confidence interval shown in Figure 3.23b needs to be used as illustrated by the example provided in Figure 3.24b. Clearly the uncertainty for the monthly distributions is much higher due to the reduction in data.

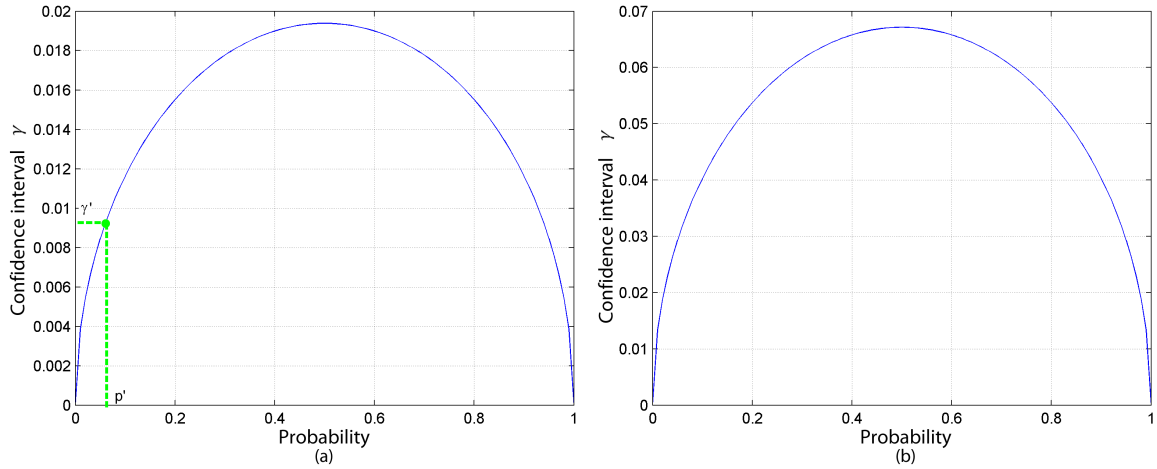


Figure 3.23: Confidence interval profiles for probability estimation based on (a) daily data of 7 years, and (b) daily data for an individual month of 7 years.

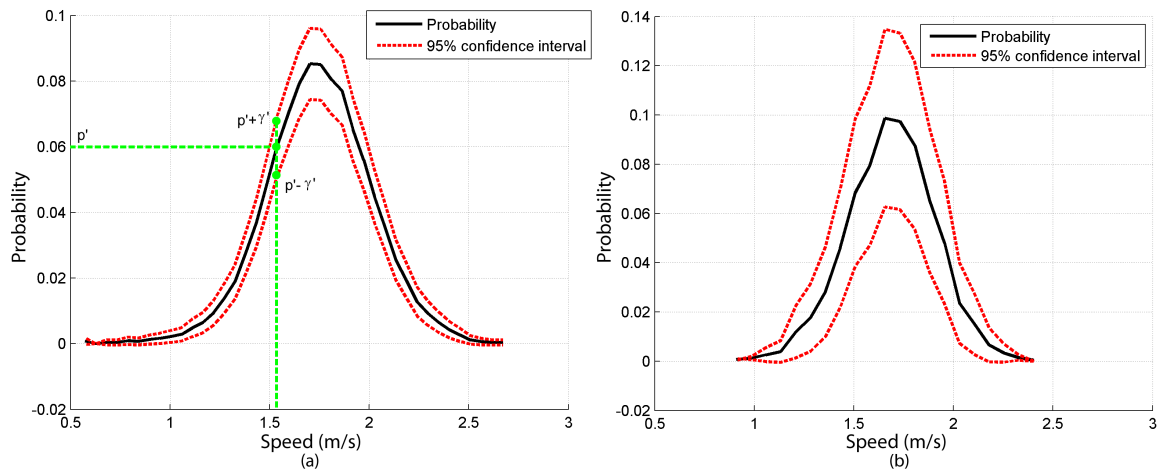


Figure 3.24: An example of the probability distribution and 95% confidence interval of surface current speed at (26.912E, 79.600W) estimated from (a) daily data of 7 years, (b) daily data of only December.

CHAPTER IV

ESTIMATES OF POWER POTENTIAL

The map of the power density has shown that the Gulf Stream, particularly the Florida Current, has the highest power density among ocean currents along the United States coastline, making it the ideal region for ocean current energy extraction. Therefore the assessment of the total extractable power for ocean currents for the United States focuses on the Gulf Stream system. The commonly used approach based on undisturbed power density is useful for identifying high energy regions and preliminary estimates of energy resources. For a single or a small number of devices, as long as there is a negligible change to the existing flow, such an estimate is reasonable. However, power density only characterizes the undisturbed kinetic energy transport by the flow, but not the generation rate of energy by turbines. A large number of devices can block the flow and reduce the current velocity, and hence reduce the generated power from each device. To incorporate the effect of reduced flow velocity due to presence of turbines, it is desirable to study the dynamics of the system in order to estimate theoretically extractable energy. Analytical dynamic models for estimating power potential from tidal streams (Garrett and Cummins, 2005) and atmospheric jet streams (Miller et al., 2011b) have been proposed. Similar analytical modeling approaches may be applicable to open ocean currents. Although tidal currents and open ocean currents share obvious similarities, they are fundamentally different regarding their dynamic mechanisms. Tidal stream currents are primarily driven by the head difference between the entrance and exit of the channel, while ocean currents are in quasi-geostrophic balance driven primarily by surface wind stress. This chapter provides a theoretical estimate of power potential from the Gulf Stream system using a simplified ocean circulation model.

4.1 Simplified Ocean Circulation Model

An analytical model based on the assumptions proposed by Stommel (1948) is applied for the present study to investigate energy dissipation from added turbines, a more realistic

measure of extractable energy resources from the Gulf Stream system. The computational domain is a simplified rectangular basin with a flat bottom representing the North Atlantic Basin. The positive x direction is eastward and the positive y northward. The horizontal extensions of the idealized basin are inspired by the real dimensions of the North Atlantic Basin. Water density is assumed constant and the flow is assumed steady. In the ocean, the advective terms (nonlinear terms) are much smaller than the Coriolis term (i.e. Rossby Number $\ll 1$), and therefore can be neglected (Vallis, 2006) in this simplified model. The reduced shallow water quasi-geostrophic equations consist of two horizontal momentum equations and the continuity equation:

$$-fv = -\frac{1}{\rho} \frac{\partial p}{\partial x} + (F_x + W_x)/\rho \quad (4.1a)$$

$$fu = -\frac{1}{\rho} \frac{\partial p}{\partial y} + (F_y + W_y)/\rho \quad (4.1b)$$

$$\frac{\partial u}{\partial x} + \frac{\partial v}{\partial y} = 0 \quad (4.1c)$$

where ρ is the water density, p is the pressure, f is the Coriolis parameter, W_i is the surface wind stress in i direction, F_i is the opposing forces associated with natural friction, turbulence, and possibly turbine drag in i direction ($i = x, y$). (x, y) are the east-west, north-south coordinates, and (u, v) are two corresponding horizontal velocity components.

The shallow water approximation and hydrostatic pressure are reasonably assumed since the depth of the ocean (on the order of 1 km) is much smaller than the horizontal extensions (on the order of 1000 km). Therefore horizontal pressure gradients are simplified to the following:

$$\nabla_h p = g\rho \nabla_h \eta \quad (4.2)$$

where η is the free surface elevation. Under the β plane approximation, the Coriolis parameter can be approximated as

$$f = f_0 + \beta y \quad (4.3)$$

where f_0 and β are constants defined as $f_0 = 2\Omega \sin \theta_0$ and $\beta = \frac{2\Omega \cos \theta_0}{a}$ with Ω as the

rotation rate of the earth, a as the earth radius and θ_0 as a reference latitude.

By cross-differentiating the two momentum equations and subtracting, the pressure gradient terms are eliminated, resulting in

$$f \left(\frac{\partial u}{\partial x} + \frac{\partial v}{\partial y} \right) + \beta v = \frac{1}{\rho} \left(\frac{\partial(F_y + W_y)}{\partial x} - \frac{\partial(F_x + W_x)}{\partial y} \right). \quad (4.4)$$

The first term above is eliminated using the continuity equation. The number of unknowns can be reduced by defining a stream function as

$$u = \frac{\partial \Psi}{\partial y} \quad (4.5a)$$

$$v = -\frac{\partial \Psi}{\partial x} \quad (4.5b)$$

No slip boundary conditions require that both velocity components are zero at the basin boundaries:

$$u(x, 0) = u(x, b) = u(0, y) = u(a, y) = 0 \quad (4.6a)$$

$$v(x, 0) = v(x, b) = v(0, y) = v(a, y) = 0 \quad (4.6b)$$

where a is the basin length in east-west direction, and b is the basin width in north-south direction.

The circulation in subtropical gyres is almost entirely governed by the forcing of the wind, therefore only wind stress is considered as the driving force in this model. The prevailing wind system on the surface of the North Atlantic ocean include easterly trade winds in the tropics and the westerlies in the middle latitude, exerting a clockwise and negative curl on the ocean surface. A convenient way to represent such wind patterns is to assume a sinusoidal wind profile:

$$W_x(y) = -\frac{\tau_0}{H} \cos\left(\frac{\pi}{b}y\right) \quad (4.7)$$

where H is the uniform depth of the ocean basin and τ_0 is the maximum wind stress.

The drag force is commonly assumed to be proportional to current velocity squared, although it can also be assumed to be proportional to current velocity for mathematical

convenience (i.e. the simplest case in Garrett and Cummins (2005)). Drag forces associated with natural friction and turbulence, and turbines are assumed linearly proportional to the current velocity. The undisturbed natural drag (i.e. without presence of turbines) is written as

$$\vec{F} = -\frac{C_d \rho}{H} \vec{V} \quad (4.8)$$

where C_d is the natural drag coefficient and has the dimension of velocity in the present setting. The final form of the governing equation becomes

$$\left(\frac{\partial^2 \psi}{\partial x^2} + \frac{\partial^2 \psi}{\partial y^2} \right) + \frac{H\beta}{C_d} \frac{\partial \psi}{\partial x} = \frac{\tau_0 \pi}{\rho b C_d} \sin\left(\frac{\pi}{b} y\right) \quad (4.9)$$

Without the presence of turbines, this model essentially simplifies to the Stommel model. The derivation of the solution of the Stommel model is explained in great detail by Stewart (2008). The solution becomes

$$\Psi(x, y) = \frac{b^2}{\pi^2} N \left(\frac{1 - e^{m_2 a}}{e^{m_1 a} - e^{m_2 a}} e^{m_1 x} + \frac{e^{m_1 a} - 1}{e^{m_1 a} - e^{m_2 a}} e^{m_2 x} - 1 \right) \sin\left(\frac{\pi y}{b}\right). \quad (4.10)$$

where $M = \frac{\beta H}{C_d}$, $N = \frac{\tau_0 \pi}{\rho b C_d}$, $m_1 = -\frac{M + \sqrt{M^2 + \frac{4\pi^2}{b^2}}}{2}$ and $m_2 = -\frac{M - \sqrt{M^2 + \frac{4\pi^2}{b^2}}}{2}$. The two velocity components are then derived to be

$$u = \frac{b}{\pi} N \left(\frac{1 - e^{m_2 a}}{e^{m_1 a} - e^{m_2 a}} e^{m_1 x} + \frac{e^{m_1 a} - 1}{e^{m_1 a} - e^{m_2 a}} e^{m_2 x} - 1 \right) \cos\left(\frac{\pi y}{b}\right) \quad (4.11a)$$

$$v = -\frac{b^2}{\pi^2} N \left(\frac{1 - e^{m_2 a}}{e^{m_1 a} - e^{m_2 a}} m_1 e^{m_1 x} + \frac{e^{m_1 a} - 1}{e^{m_1 a} - e^{m_2 a}} m_2 e^{m_2 x} \right) \sin\left(\frac{\pi y}{b}\right). \quad (4.11b)$$

4.2 Model Calibration

Before the model can be applied to calculate energy dissipation, it needs to be calibrated to ensure it reproduces reasonable flow properties. Considering the great complexity and variability of the Gulf Stream system, this simple analytical model is calibrated by time averaged bulk flow properties, ideally volume flux and kinetic energy flux in the western boundary layer representing the Gulf Stream.

The basin is defined as $a = 6000$ km long in x direction, and $b = 3142$ km wide in y direction. The Coriolis parameter β in the middle latitude is approximately $2 \times$

$10^{-13}\text{cm}^{-1}\text{sec}^{-1}$. The “basin depth” H in this model is not the mean physical ocean depth, but the depth of surface layer primarily driven by surface winds (i.e. Ekman layer). Stommel (1948) proposed the basin depth $H = 200$ m, maximum wind stress $\tau_0 = 10^{-5}$ N/cm², or 1 dyn/cm², and natural drag coefficient $C_d = 0.02$ (cm/s), however these parameters are further calibrated here.

The calibrated model needs to be able to reproduce most reasonable bulk flow properties including volume flux and energy flux in the selected cross-section on the western boundary (Figure 4.1) that represents the Gulf Stream. In this study, the seven years of HYCOM data were used to calculate the reference volume and energy fluxes. It has already been demonstrated in previous sections that the HYCOM data is accurate in predicting the bulk flow properties of the Gulf Stream system.

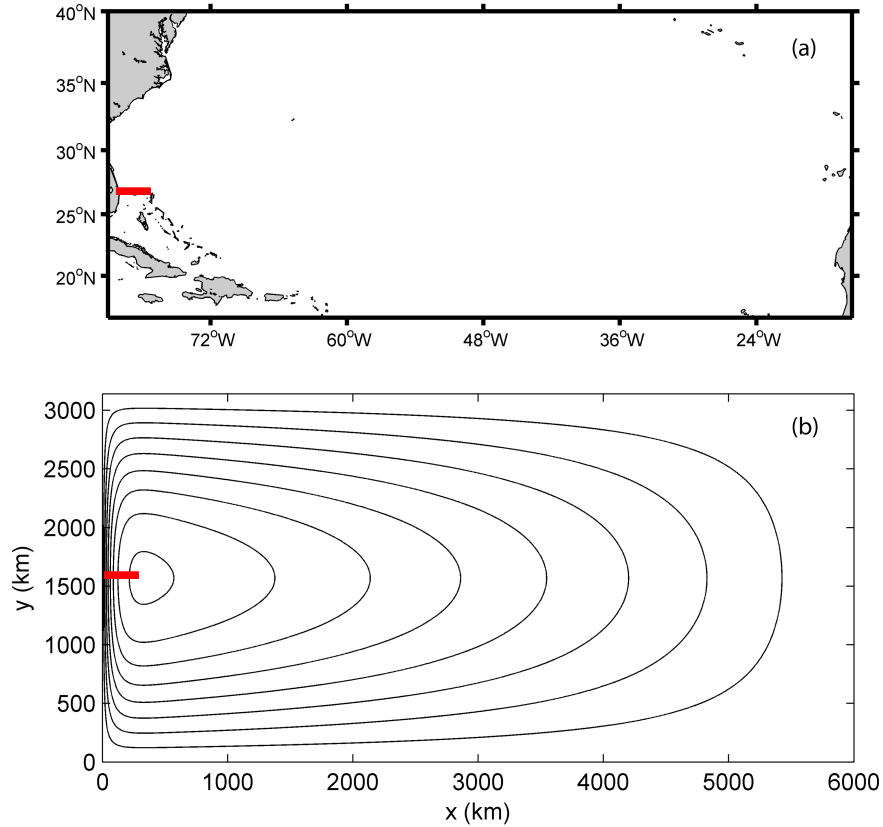


Figure 4.1: Location of the selected cross-section (red line) in the Gulf Stream system, through which volume flux and energy flux are calculated and compared: (a) the North Atlantic Basin, and (b) the simplified basin with analytical streamlines.

For different combinations of basin depth H , maximum wind stress τ_0 , and natural drag coefficient C_d , the model produces different flow solutions, and therefore different volume and kinetic energy fluxes computed as

$$Q = \int \vec{V} \cdot d\vec{A} \quad (4.12a)$$

$$E_f = \int \frac{1}{2} \rho |\vec{V}|^2 \vec{V} \cdot d\vec{A} \quad (4.12b)$$

through the selected cross-section. The goal of calibration is to find model parameters that minimize both $|\frac{Q_a}{Q_m} - 1|$ and $|\frac{E_{fa}}{E_{fm}} - 1|$, where the a and m subscripts represent analytical and HYCOM results respectively. Since these quantities do not always reach minimum at the same time, a compromised strategy is to minimize a new parameter called the ‘‘Error Factor’’ ($E.F.$):

$$E.F. = \left(\frac{Q_a}{Q_m} - 1 \right)^2 + \left(\frac{E_{fa}}{E_{fm}} - 1 \right)^2. \quad (4.13)$$

Figure 4.2 shows the variation of E.F. as a function of model parameters. Results show basin depth $H = 140$ m, wind stress $\tau_0 = 1$ dyn/cm² and natural drag coefficient $C_d = 0.021$ cm/s lead to the optimal model performance in terms of undisturbed volume and energy fluxes in the Gulf Stream cross-section.

4.3 Uniform Turbine Drag

When the turbine drag is added, energy dissipation will be comprised of natural dissipation and dissipation by turbines, a fraction of which can be collected by turbines and converted into electricity. The presence of turbines is incorporated in the model as additional turbine drag. Similar to natural drag, the additional turbine drag \vec{T} is assumed linearly proportional to current velocity in the following form

$$\vec{T} = -\frac{C_t \rho}{H} \vec{V} \quad (4.14)$$

where C_t is the turbine drag coefficient, and similar to C_d , has dimensions of velocity. The total drag force with turbines becomes $-\frac{(C_t + C_d) \rho}{H} \vec{V}$. The solution of the flow has the same

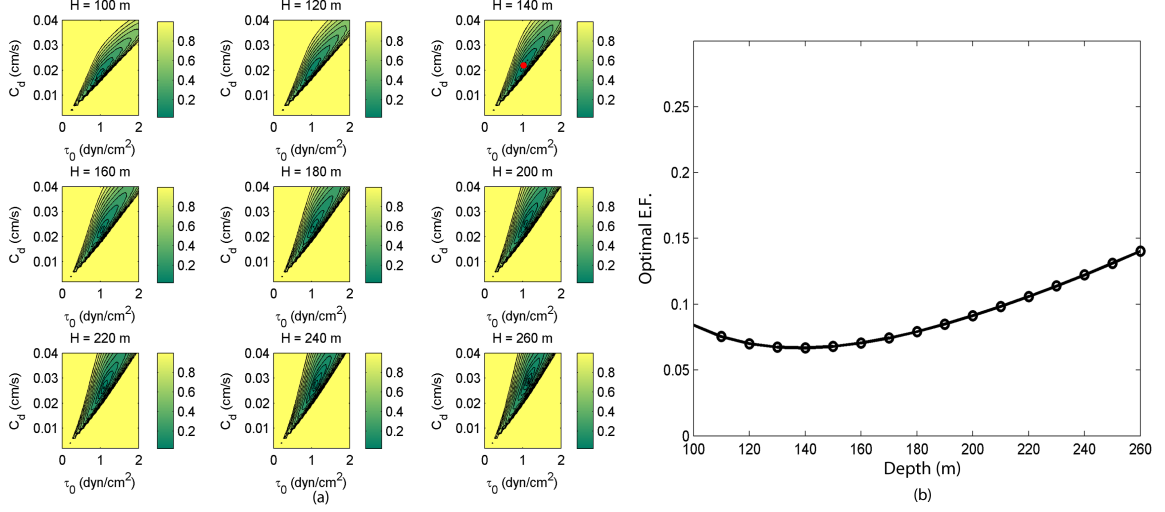


Figure 4.2: (a) Error Factor “E.F.” as a function of varying maximum wind stress τ_0 and natural friction coefficient C_d for different depths, and (b) “E.F.” as a function of depth.

form in Equation 4.11 except that C_d is replaced with $(C_d + C_t)$. At this time there is no explicit relationship between turbine drag coefficient and the actual number of turbines, although increases in the turbine drag coefficient can be thought of as adding more turbines.

The mechanical energy equation may be found by multiplying Equations 4.1a and 4.1b with horizontal velocity components u and v , and adding them together, eliminating the Coriolis terms, resulting in

$$-\frac{u}{\rho} \frac{\partial p}{\partial x} - \frac{v}{\rho} \frac{\partial p}{\partial y} + (F_x + W_x)/\rho u + (F_y + W_y)/\rho v = 0. \quad (4.15)$$

Substituting Equations 4.7, 4.8 and 4.14 for the wind stress and drag force into the equation above and including turbine drag results in the following mechanical energy balance equation:

$$[-uH \frac{\partial p}{\partial x} - vH \frac{\partial p}{\partial y}] + [-\rho C_d(u^2 + v^2)] + [-\rho C_t(u^2 + v^2)] + [-\tau_0 u \cos(\pi \frac{y}{b})] = 0. \quad (4.16)$$

The four terms in the above equation represent work done by pressure gradient P_{pres} , natural dissipation $D_{natural}$, energy dissipation by turbines $D_{turbine}$, and the energy production from surface wind stress P_{prod} , respectively. The ocean basin is considered a closed system, and

Equation 4.16 is integrated over the entire domain. By substituting the solutions from Equations 4.11 into the following integration, it is found that

$$\int_{x=0}^a \int_{y=0}^b \left[-\rho C_d(u^2 + v^2) - \rho C_t(u^2 + v^2) - \tau_0 u \cos\left(\pi \frac{y}{b}\right) \right] dx dy = 0. \quad (4.17)$$

Therefore we also have

$$\int_{x=0}^a \int_{y=0}^b \left[-uH \frac{\partial p}{\partial x} - vH \frac{\partial p}{\partial y} \right] dx dy = 0. \quad (4.18)$$

Equations 4.17 and 4.18 essentially mean in this closed circulation system, energy is solely produced from wind stress (P_{prod}) and dissipated from natural dissipation ($D_{natural}$) and turbines ($D_{turbine}$). Work by pressure gradient P_{pres} only serves to redistribute energy in the basin, but does not produce or dissipate energy.

The turbine drag coefficient C_t is a function of the number of turbines and turbine spacing. Intuitively the greater this turbine drag coefficient, the stronger energy extraction will be. Although an explicit relationship between turbine drag coefficient and the number of turbines does not exist, increases in the turbine drag coefficient can be thought of as adding more turbines or increasing their size thereby further dissipating the flow field and reducing the velocity. The flow speed $|V| = \sqrt{u^2 + v^2}$ as well as the total energy dissipation from turbines are functions of C_t :

$$\int D_{turbine}(C_t) dA = - \int C_t \rho |V(C_t)|^2 dA. \quad (4.19)$$

Therefore the total energy balance from Equation 4.17 in the circulation system is rewritten as

$$- \int \tau_0 \cos\left(\pi \frac{y}{b}\right) u(C_t) dA = \int C_d \rho |V(C_t)|^2 dA + \int C_t \rho |V(C_t)|^2 dA. \quad (4.20)$$

The left hand side represents the energy production, and the right hand side the energy dissipation. In Equation 4.20, as C_t increases, current velocity in the circulation will decrease due to increased friction, which will reduce the left hand side term (i.e. energy production

by wind stress), and hence the sum of two terms on the right hand side (i.e. total dissipation in the system).

Equations 4.1a and 4.1b show the momentum balance of the circulation. In the x (zonal) direction, the undisturbed circulation is under the force balance between Coriolis force (fv), pressure gradient ($-g\frac{\partial\eta}{\partial x}$), drag force ($-(C_d u)/H$) and wind stress ($-\frac{\tau_0}{\rho H} \cos(\frac{\pi y}{b})$). In the y (meridional) direction, the force balance is between Coriolis force ($-fu$), pressure gradient ($-g\frac{\partial\eta}{\partial y}$), and drag ($-(C_d v)/H$). Because of the western boundary intensification resulting from the Coriolis Effect, the meridional velocity component v reaches its peak in the middle of the western boundary layer, leading to a peak Coriolis force in the zonal direction at the same location, as seen in Figure 4.3. It is also seen in Figure 4.4 that the meridional Coriolis force is primarily balanced by pressure gradient due to spatial variation of sea surface elevation. The peak pressure gradient in the x direction is observed on the western boundary, and therefore the steepest water surface inclination in the x direction is expected in the same region. The drag force in the x direction is relatively weak in the momentum balance compared to the Coriolis force and pressure gradient, and so is wind stress in most of the basin except on the southern and northern boundaries where the wind stress is the strongest. In the y direction, the Coriolis force is relatively weaker compared to the x direction because of the relatively weaker zonal velocity component u . However in most of the basin, the meridional Coriolis force is still primarily balanced by the pressure gradient except on the western boundary where the drag force is relatively strong due to fast current velocity in y direction.

It is seen that the primary force balance is between Coriolis force and pressure gradient in both x and y directions in the basin. Therefore the geostrophic characteristic of the circulation is still dominant in most of the basin. Areas of exception include the western, southern and northern boundaries, where external forces are strong and therefore force balance shifts away from the geostrophic balance.

The total energy dissipation by turbines is shown in Figure 4.5 as a function of turbine drag coefficient C_t . Because the flow features seasonal variation, the strongest in summer and the weakest in winter, Figure 4.5 also shows three curves with markers that correspond

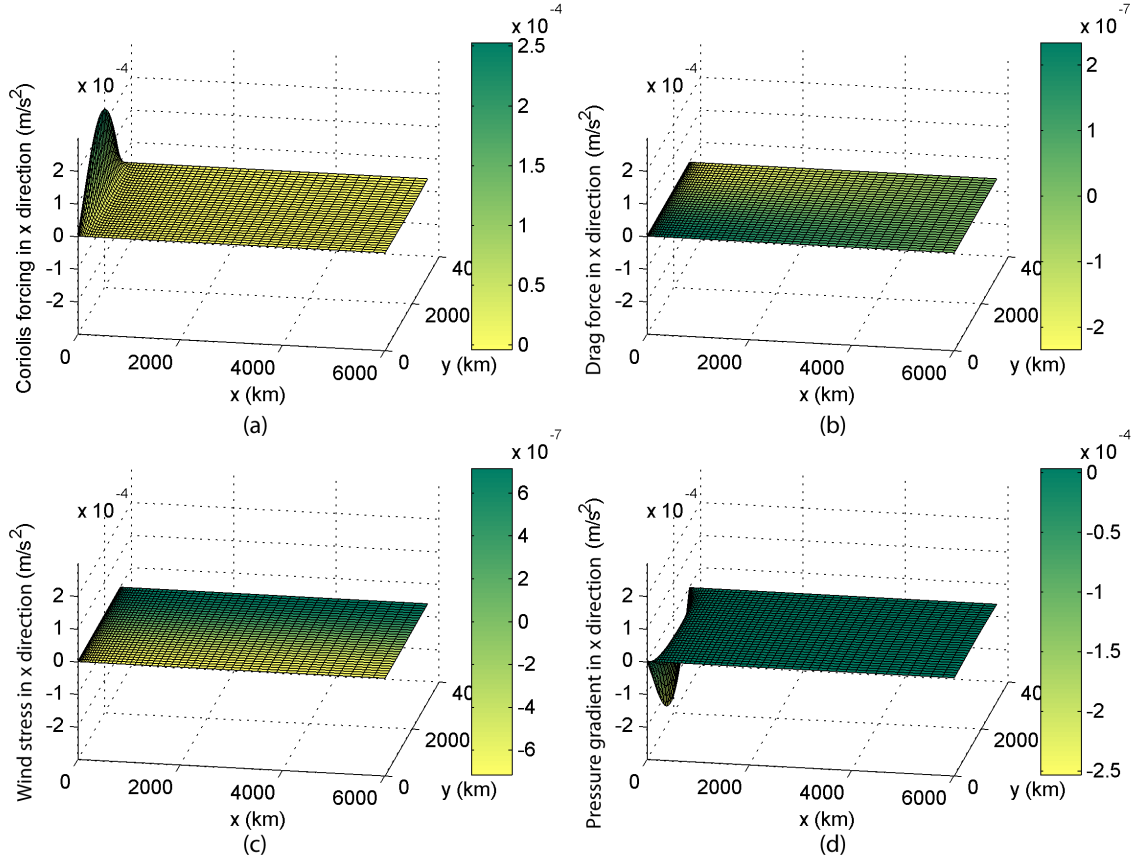


Figure 4.3: Spatial variation of each term in the x momentum equation: (a) Coriolis forcing, (b) drag force, (c) wind stress, (d) pressure gradient.

to the minimum, mean and maximum flow conditions due to seasonal variability. The curve of the mean flow condition is highlighted in red. The trend of energy dissipation from turbines is very obvious. When no turbines are added (i.e. turbine drag coefficient $C_t = 0$), the ocean current is undisturbed and energy dissipation by turbines is zero. Under this condition, the natural dissipation is highest (≈ 94 GW). This number is not far from the estimate by Csanady (1989), which is about 70 GW. As the turbine drag coefficient C_t increases from zero, the energy dissipation by turbines also increases until C_t reaches about 0.04, where energy dissipation from turbines D_t reaches its maximum level (≈ 44 GW). As C_t increases to beyond 0.04, D_t starts to decrease with C_t , which means adding more turbines in this condition does not result in more total dissipation from the turbines, but simply further blocks the current flow. Physically it means that although the number of

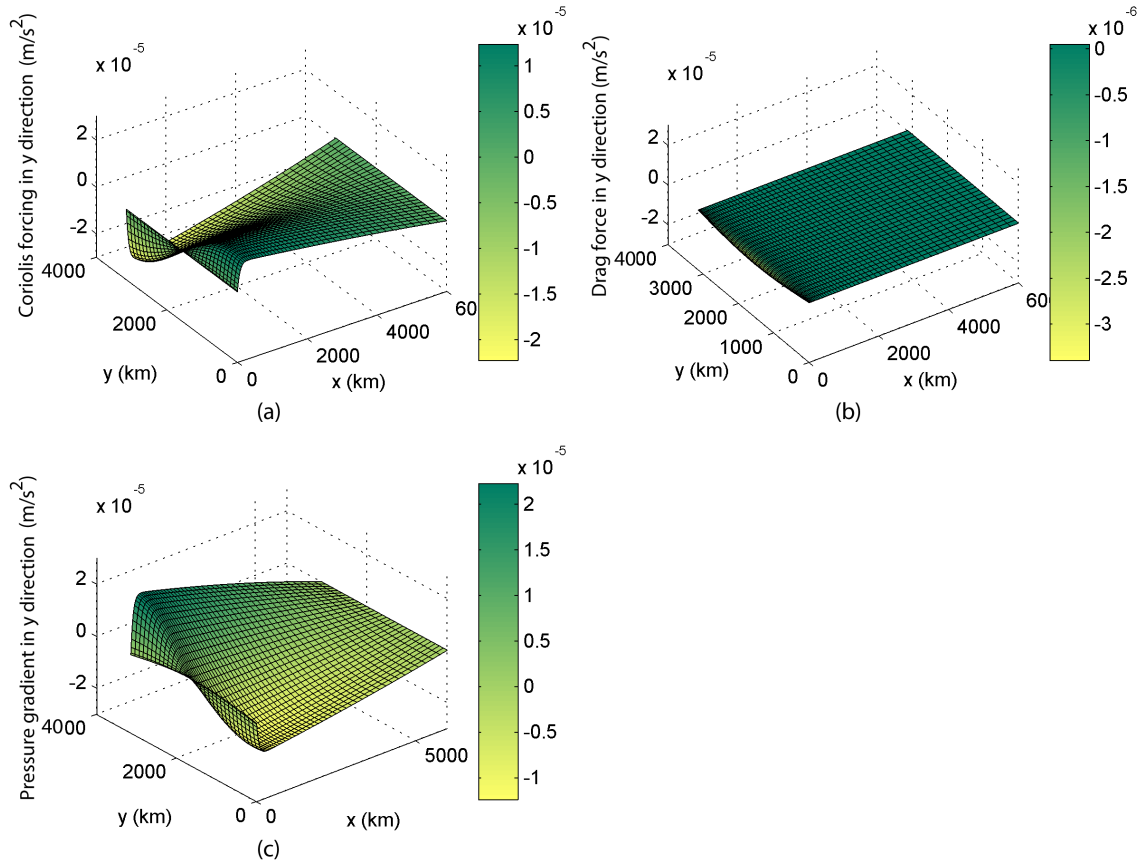


Figure 4.4: Spatial variation of each term in the y momentum equation: (a) Coriolis forcing, (b) drag force, (c) pressure gradient.

turbines increases, the energy dissipation from each turbine decreases. The product of those two, namely, the total dissipation from the turbines, also decreases. It is shown that maximum total energy dissipation by turbines is achieved when turbine drag coefficient is about twice the natural drag coefficient. This means the upper limit results in about twice as much energy dissipated by turbines as is dissipated by natural friction. The natural dissipation rate decreases monotonically as turbine drag increases (blue curve in Figure 4.5). The sum of the natural dissipation and dissipation by turbines, namely the total energy dissipation, also decreases with the turbine drag coefficient, since higher turbine drag slows down the current speed in the circulation reducing the total energy input from the wind stress.

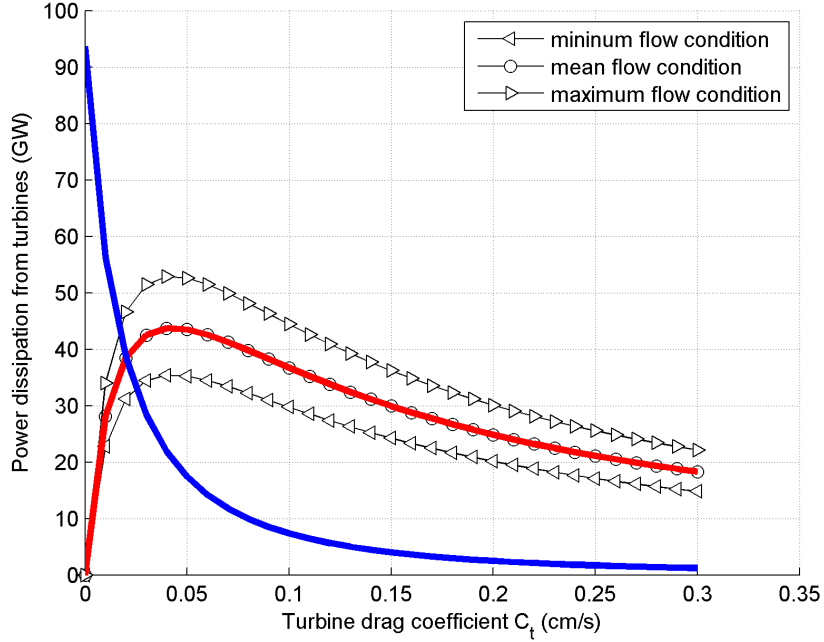


Figure 4.5: Power dissipation from turbines for three different flow conditions as a function of the turbine drag coefficient; energy dissipation by turbines for the mean flow condition is highlighted in red and the corresponding natural dissipation is highlighted in blue.

4.4 Localized Turbine Drag

The model thus far established a relationship between uniform turbine drag coefficients and the energy dissipation by turbines and determined that peak energy dissipation rates from turbines exist. To more realistically simulate the scenario of specifically extracting power only from the Gulf Stream area, it is necessary to modify the model to address the locally high energy dissipation in the Gulf Stream due to turbines. It is desirable to have a spatially varying turbine drag coefficient instead of a constant value. Therefore C_t is formulated as a function of both x and y instead of a simple constant.

In this case, differentiating x and y momentum equations with respect to y and x respectively and subtracting result in a slightly different equation

$$f \frac{\partial u}{\partial x} + u \frac{\partial f}{\partial x} + \left(f \frac{\partial v}{\partial y} + v \frac{\partial f}{\partial y} \right) = \frac{1}{H} \left(u \frac{\partial C_{total}}{\partial y} + C_{total} \frac{\partial u}{\partial y} \right) - \frac{1}{H} \left(C_{total} \frac{\partial v}{\partial x} + v \frac{\partial C_{total}}{\partial x} \right) - \frac{\tau_0}{\rho H} \frac{\pi}{b} \sin\left(\frac{\pi}{b} y\right), \quad (4.21)$$

where $C_{total} = C_d + C_t$ and represents the total of natural and turbine drag. The above

equation is further simplified as

$$\beta v = \frac{C_{total}}{H} \left(\frac{\partial u}{\partial y} - \frac{\partial v}{\partial x} \right) + \frac{1}{H} \left(u \frac{\partial C_{total}}{\partial y} - v \frac{\partial C_{total}}{\partial x} \right) - \frac{\tau_0}{\rho H} \frac{\pi}{b} \sin\left(\frac{\pi}{b}y\right) \quad (4.22)$$

After introducing the streamfunction ψ , the governing equation becomes

$$\left(\frac{\partial^2 \psi}{\partial x^2} + \frac{\partial^2 \psi}{\partial y^2} \right) + \alpha_1(x, y) \frac{\partial \psi}{\partial x} + \alpha_2(x, y) \frac{\partial \psi}{\partial y} = \frac{\tau_0 \pi}{\rho b C_{total}} \sin\left(\frac{\pi}{b}y\right) \quad (4.23)$$

where $\alpha_1(x, y) = \left(\frac{1}{C_{total}} \frac{\partial C_{total}}{\partial x} + \frac{H\beta}{C_{total}} \right)$, and $\alpha_2(x, y) = \left(\frac{1}{C_{total}} \frac{\partial C_{total}}{\partial y} \right)$.

To more accurately represent the scenario of extracting power from the fastest western boundary currents (i.e. the Gulf Stream), it is desirable to design a spatially varying turbine drag profile that peaks in the middle of the western boundary where the current is the strongest and declines rapidly to zero away from the Gulf Stream region. The turbine drag coefficient profile is formulated as

$$C_t(x, y) = C_{t0} e^{-\frac{x^2 + (y - \frac{1}{2}b)^2}{\epsilon}} \quad (4.24)$$

where C_{t0} is the peak value of the turbine drag coefficient, and ϵ is a parameter controlling the approximate area of the turbine region. An example illustrating the spatially varying C_t is shown in Figure 4.6.

Equation 4.23 is a second order partial differential equation with variable coefficients. Because of the spatially varying drag coefficient, analytical solutions are no longer possible and a numerical solution is obtained. Considering the simplicity of the model domain, a finite difference approach is used to approximate the derivatives in the differential equation. The computational domain is discretized into a Cartesian mesh, and the differential equation is replaced by difference equations at each mesh point. At each mesh point (i, j) the partial derivatives are replaced by central difference quotients:

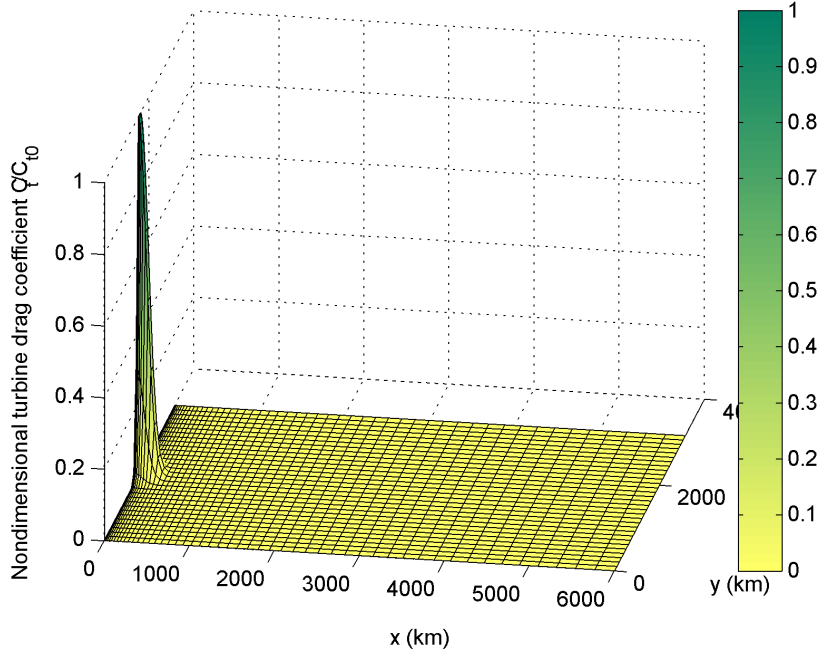


Figure 4.6: Distribution of the non-dimensional localized turbine drag in the Gulf Stream ($\epsilon = 10^4 km^2$).

$$\frac{\partial \psi}{\partial x} = \frac{\psi_{i+1,j} - \psi_{i-1,j}}{x_{i+1,j} - x_{i-1,j}} \quad (4.25a)$$

$$\frac{\partial \psi}{\partial y} = \frac{\psi_{i,j+1} - \psi_{i,j-1}}{x_{,j+1} - x_{,j-1}} \quad (4.25b)$$

$$\frac{\partial^2 \psi}{\partial x^2} = \frac{\frac{\psi_{i+1,j} - \psi_{i,j}}{x_{i+1,j} - x_{i,j}} - \frac{\psi_{i,j} - \psi_{i-1,j}}{x_{i,j} - x_{i-1,j}}}{x_{i+\frac{1}{2},j} - x_{i-\frac{1}{2},j}} \quad (4.25c)$$

$$\frac{\partial^2 \psi}{\partial y^2} = \frac{\frac{\psi_{i,j+1} - \psi_{i,j}}{x_{i,j+1} - x_{i,j}} - \frac{\psi_{i,j} - \psi_{i,j-1}}{x_{i,j} - x_{i,j-1}}}{x_{i,j+\frac{1}{2}} - x_{i,j-\frac{1}{2}}} \quad (4.25d)$$

where i and j are indices in x and y directions. Indices $\{i \pm 1/2\}$ and $\{j \pm 1/2\}$ in the subscripts represent the midpoints between two adjacent grid points. The approximation for partial derivatives in this study is accurate to second order. Approaches to solve similar problems on a uniform grid with constant coefficients exist (e.g. Melek-Madani (2012)). A higher resolution near the western boundary is desired since the formation of a narrow western region with fast moving currents is expected. Therefore a non-uniform mesh is designed to discretize the domain such that mesh points have a higher density on the western boundary with a reduction in density to the east. In the x direction, a transitional

uniform mesh is first defined as $z = 0, z_1, z_2, \dots, z_n, a$, where $\Delta z = z_{i+1} - z_i = \frac{a}{n+1}$. Then the actual horizontal mesh is defined as

$$x = z^t / a^{t-1} \quad (4.26)$$

where t is a free parameter controlling the density of points on the western boundary. This maps the uniform mesh to a non-uniform mesh also defined within the same interval of $\{0, a\}$, where $x = \{0, x_1, x_2, \dots, x_n, a\}$. In the y direction, the mesh is kept uniform and $y = \{0, y_1, y_2, \dots, y_m, b\}$, where $\Delta y = y_{i+1} - y_i = k = \frac{b}{m+1}$. Therefore the network of the grid is established as $(x_{i,j}, y_{i,j}) = (\frac{(i\Delta z)^t}{a^{t-1}}, jk)$, where $1 \leq i \leq n, 1 \leq j \leq m$. In non-uniform grid mesh, points with “ $i \pm 1/2$ ” indices will not be located at the geometrical center of two adjacent grid points, but slightly biased to the lower end according to the conversion in Equation 4.26. Figure 4.7 shows the non-uniform mesh grid with $t = 3, n = 50$ and $m = 30$.

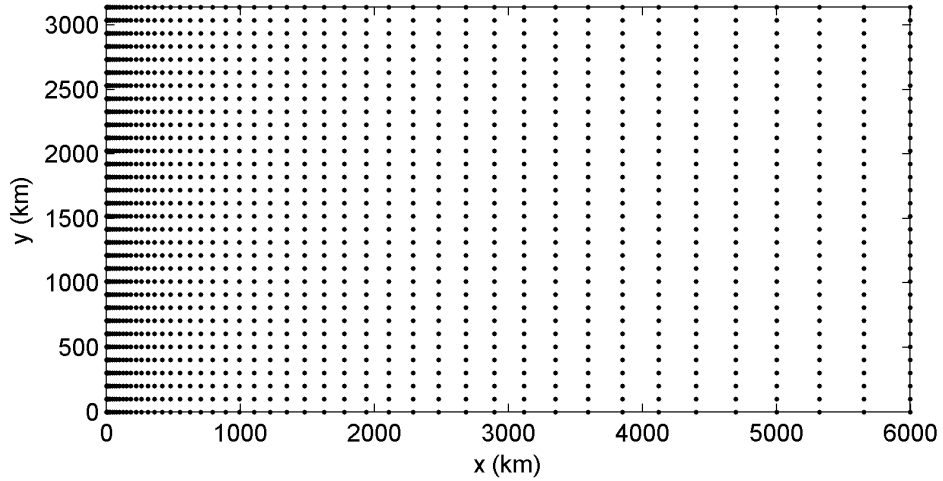


Figure 4.7: Non-uniform mesh grid for the domain with $t=3, n=50$, and $m=30$.

Substituting Equation 4.25 into the governing Equation 4.23, the governing equation can be rearranged to the following form

$$\psi_{i,j}[A_1] + \psi_{i+1,j}[A_2] + \psi_{i-1,j}[A_3] + \psi_{i,j+1}[A_4] + \psi_{i,j-1}[A_5] = F_{i,j} \quad (4.27)$$

where coefficients $A_1 \sim A_5$ are all functions of x and y :

$$A_1 = -\frac{1}{x_{i+\frac{1}{2},j} - x_{i-\frac{1}{2},j}} \left(\frac{1}{x_{i+1,j} - x_{i,j}} + \frac{1}{x_{i,j} - x_{i-1,j}} \right) - \frac{1}{x_{i,j+\frac{1}{2}} - x_{i,j-\frac{1}{2}}} \left(\frac{1}{x_{i,j+1} - x_{i,j}} + \frac{1}{x_{i,j} - x_{i,j-1}} \right) \quad (4.28a)$$

$$A_2 = \frac{1}{\left(x_{i+\frac{1}{2},j} - x_{i-\frac{1}{2},j}\right) (x_{i+1,j} - x_{i,j})} + \frac{\alpha_1(x_{i,j}, y_{i,j})}{x_{i+1,j} - x_{i-1,j}} \quad (4.28b)$$

$$A_3 = \frac{1}{\left(x_{i+\frac{1}{2},j} - x_{i-\frac{1}{2},j}\right) (x_{i,j} - x_{i-1,j})} + \frac{\alpha_1(x_{i,j}, y_{i,j})}{x_{i+1,j} - x_{i-1,j}} \quad (4.28c)$$

$$A_4 = \frac{1}{\left(y_{i,j+\frac{1}{2}} - y_{i,j-\frac{1}{2}}\right) (y_{i,j+1} - y_{i,j})} + \frac{\alpha_2(x_{i,j}, y_{i,j})}{y_{i,j+1} - y_{i,j-1}} \quad (4.28d)$$

$$A_5 = \frac{1}{\left(y_{i,j+\frac{1}{2}} - y_{i,j-\frac{1}{2}}\right) (y_{i,j} - y_{i,j-1})} + \frac{\alpha_2(x_{i,j}, y_{i,j})}{y_{i,j+1} - y_{i,j-1}} \quad (4.28e)$$

The terms on the right hand side $F_{i,j}$ represents the wind forcing and is only a function of y or j in our model. Equation 4.27 is series of linear algebraic equations, which can also be written in matrix form,

$$\mathbf{A}\boldsymbol{\psi} = \mathbf{F}. \quad (4.29)$$

The stream-function is solved by taking the inverse of the coefficient matrix:

$$\boldsymbol{\psi} = \mathbf{A}^{-1}\mathbf{F}. \quad (4.30)$$

Equation 4.30 is solved as an implicit numerical solution of the streamfunction, which is used to calculate the flow field using Equation 4.5.

4.5 Numerical Model Validation

In order to validate the numerical method, the solution is compared with the analytical solution for cases with uniform turbine drag coefficients. To quantify the error between analytical and numerical solutions, the ratios of Root Mean Square (*RMS*) of the difference between analytical and numerical energy dissipation to the mean value of analytical energy dissipation (*MEAN*) are calculated for 3 different grid resolutions (50×30 , 100×30 , and 150×30) and 3 different non-uniform schemes (t=1, 2 and 3). Table 4.1 shows

RMS/MEAN (%) for the case with maximum energy dissipation by turbines using different grid resolutions and schemes. It is found that denser grid points on the western boundary produces better agreement between numerical and analytical solutions, and the numerical solution converges towards the analytical solution as spatial resolution increases. The case with $t = 3$ and resolution of 150×30 (named case T3 hereafter) produces a numerical solution with error *RMS/MEAN* less than 1%. Although higher resolution might be able to produce better results, the computational expense increases greatly for the implicit solution and case T3 is already shown capable of producing results with reasonable accuracy. Therefore the model settings from case T3 are used in the subsequent analysis. Figure 4.8a shows the comparison of analytical and numerical total energy production/dissipation for case T3. Since the energy dissipation is comprised of natural dissipation and dissipation by turbines, Figure 4.8b shows the comparison of natural dissipation and dissipation by turbines from both analytical and numerical solutions for case T3. It is clear from these figures that the numerical model is able to reasonably reproduce the analytical results.

Table 4.1: The relative error (*RMS/MEAN*) between analytical and numerical total energy dissipation for different spatial resolutions and different t values.

RMS/MEAN error (%)	50x30	100x30	150x30
t=1	4.24%	3.91%	3.64%
t=2	1.82%	1.48%	0.97%
t=3	1.22%	1.16%	0.94%

4.6 Total Energy Dissipation by Localized Turbines

The total energy dissipation from the turbine drag is evaluated by

$$D_{turbine} = \int C_t(x, y, C_{t0}) |V(C_t(x, y, C_{t0}))|^2 dA \quad (4.31)$$

which is a function of C_{t0} . In Equation 4.31, V is the current speed and is equal to $\sqrt{u^2 + v^2}$, and u and v have already been numerically solved. The sensitivity of energy dissipation by turbines to the peak turbine drag coefficient C_{t0} is shown in Figure 4.9. Curves of different colors in Figure 4.9 correspond to different values of ϵ in Equation 4.24, and therefore different surface areas of turbines. Figure 4.9a shows the approximate areas of localized turbine regions (boundaries defined as lines of 50% of the peak drag

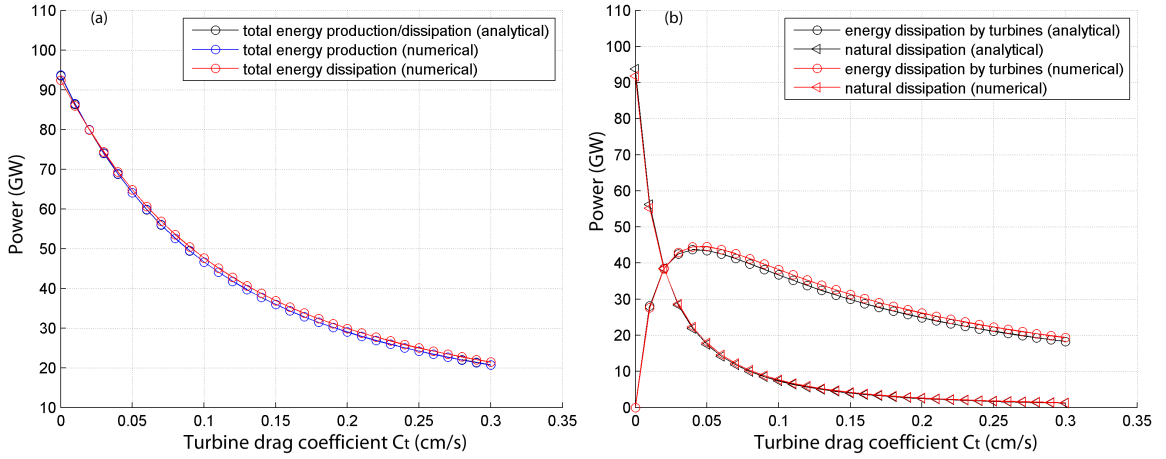


Figure 4.8: (a) Analytical and numerical total energy production/dissipation, and (b) energy dissipation by turbines and natural dissipation from both analytical and numerical solutions for case T3.

coefficient) for 5 different scenarios, ranging from about 0.1% (scenario A) to approximately 23% (scenario E) of the entire basin surface area. Different scenarios can be related to different realistic spatial coverage. For example, scenario A has an approximate area of $2 \times 10^4 \text{km}^2$, which is similar to the actual surface area of the Florida Strait. Scenario C has an area of approximately $1.7 \times 10^5 \text{km}^2$, which is similar to the surface area of the Gulf Stream along the entire U.S. east coast extending from Florida to Cape Hatteras. For different scenarios, the energy dissipation from localized turbines with respect to different levels of turbine drag coefficients all share similar trends. As the turbine drag coefficient increases from zero, the energy dissipation by turbines increase until it reaches its peak. Beyond the peak, further increasing the turbine drag coefficient reduces the total energy dissipation from turbines. As the area of the turbine region increases from scenario A to scenario E, the peak energy dissipation by turbines increases accordingly and approaches an upper bound associated with uniform turbine drag coefficient (yellow curve in Figure 4.9b).

As shown in Table 4.2, for scenario A, the peak power removal from the flow by turbines is found to be about 5.1 GW, occurring at $C_{t0} = 0.08$. The peak power removal increases to approximately 10.1 GW in scenario B and 18.6 GW in scenario C. In scenario D, the turbine area covers almost the entire western boundary with fast currents, and the peak

power removal reaches about 34 GW at $C_{t0} = 0.14$. In scenario E, the turbine area covers almost the entire western quarter of the basin, and the peak energy removal rate (40.9 GW) is very close to the case with uniform turbine drag coefficient (44 GW). The current flow in the Gulf Stream features seasonal variation, and is found to be the strongest in summer and the weakest in spring. Figure 4.10 shows curves that correspond to the minimum and maximum flow conditions due to seasonal variability. The peak dissipation ranges between 4 and 6 GW with a mean around 5 GW for scenario A. The corresponding peak powers from the different flow conditions are shown in Table 4.2.

Table 4.2: The values of approximate turbine region area, peak turbine drag coefficient, and peak power for all scenarios.

Scenario	Area percent	Area (km^2)	C_{t0} (cm/s)	Mean peak power (GW)	Peak power range (GW)
A	0.10%	1.8×10^4	0.08	5.1	4.0-6.0
B	0.23%	4.3×10^4	0.10	10.1	8.2-12.3
C	0.92%	1.7×10^5	0.12	18.6	15.1-22.5
D	3.7%	6.9×10^5	0.14	34.0	27.5-41.1
E	23%	4.3×10^6	0.06	40.9	33.1-49.2
Uniform	100%	1.8×10^7	0.04	44.0	36.4-54.1

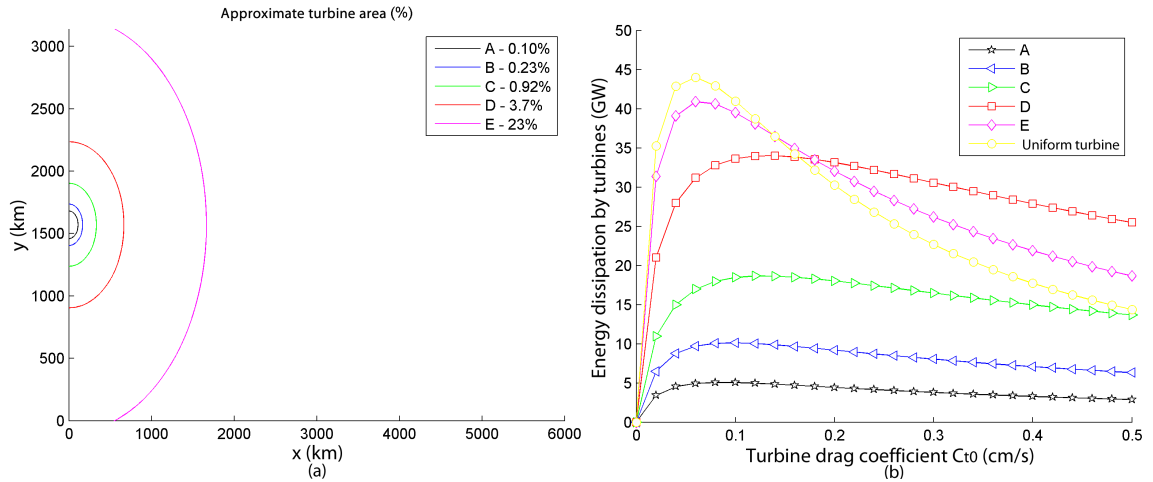


Figure 4.9: (a) Approximate areas of turbine regions for 5 different scenarios, (b) energy dissipation by turbines as a function of the peak turbine drag coefficient C_{t0} for different scenarios.

4.7 Effects of Localized Turbine Drag

The effects on the flow field of turbine dissipation for the different scenarios with varying surface areas are found to be qualitatively similar, and only differ quantitatively for impact areas and strength. Therefore, only scenario A is analyzed extensively and conclusions on the other scenarios are only summarized.

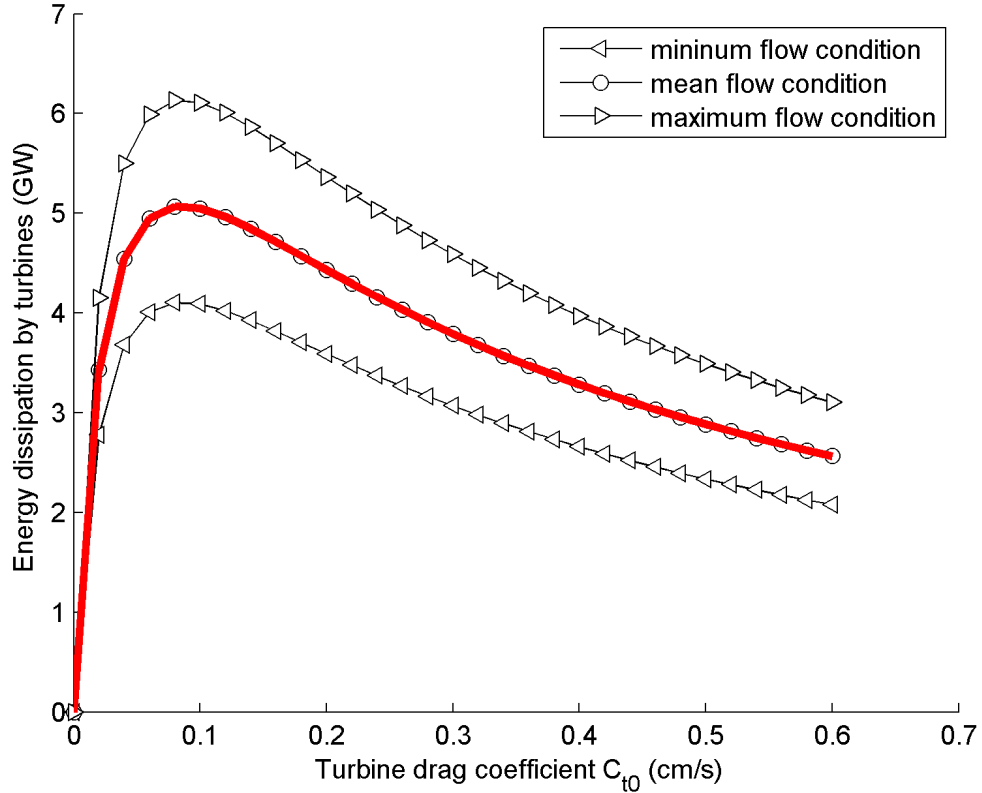


Figure 4.10: Energy dissipation by turbines as a function of turbine drag coefficient for three different seasonal flow conditions for scenario A (red curve highlighting the mean flow condition).

The effect of turbines for Scenario A on the flow field in the Gulf Stream is found to be primarily confined in the neighborhood of the turbine region while its impact on the far field is negligible. Figures 4.11 and 4.12 show the detailed changes within the western boundary of the two velocity components in response to the localized turbine drag in the Gulf Stream. The meridional velocity in the turbine region decreases significantly due to the high resistance from turbines. The meridional velocity is reduced to a quarter of the

original magnitude at the location with peak energy dissipation by turbines. Outside the turbine region, the meridional velocity change is negligible, therefore forming two residual meridional velocity peaks immediately up and down stream of the turbine region along the western boundary. The zonal velocity responds differently to the additional turbine drag. The zonal velocity changes direction in both the upstream and downstream of the turbine region along the western boundary. The zonal velocity magnitude increases due to the turbine presence. In the upstream, the undisturbed current flow has a westward zonal velocity component. Additional turbine drag inhibits the flow from continuing westward and guides it eastward to bypass the high resistance area. Similarly the downstream zonal velocity is redirected from the undisturbed eastward to westward with the addition of turbines.

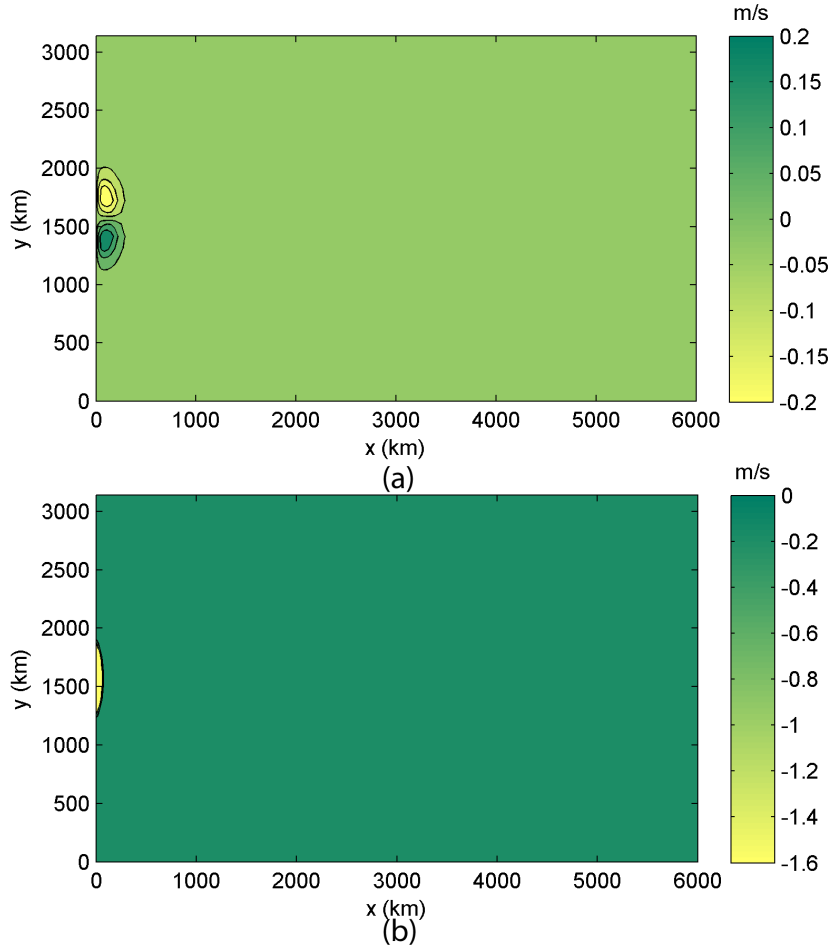


Figure 4.11: Changes of (a) zonal velocity component, (b) meridional velocity component due to additional localized turbine drag (scenario A).

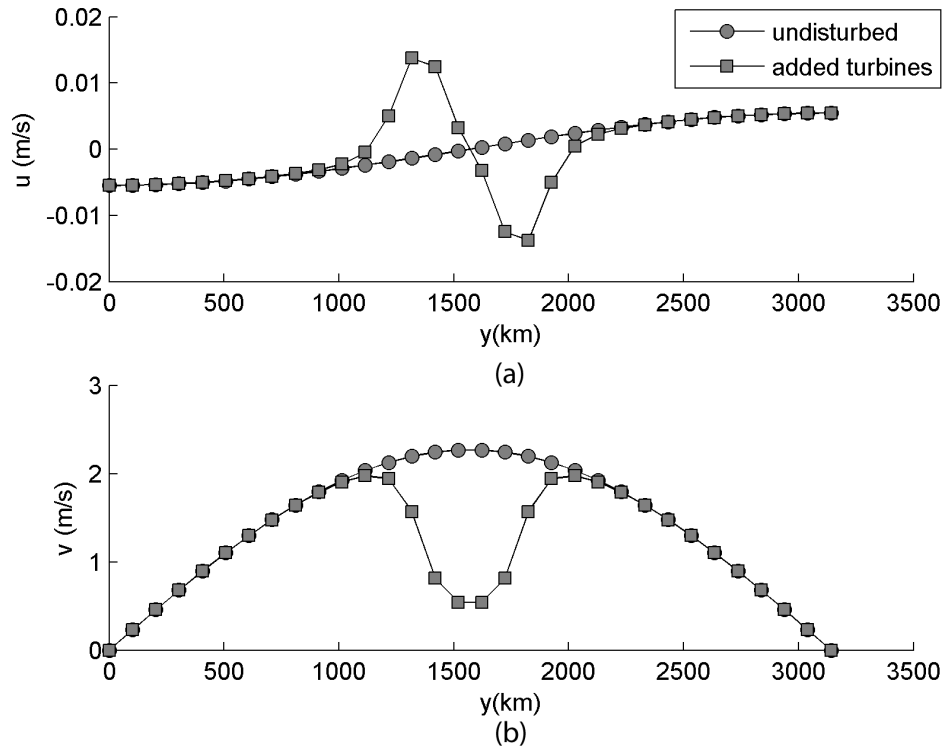


Figure 4.12: Comparing (a) zonal (u), and (b) meridional (v) current velocity components along the western boundary layer ($x \approx 2km$) for undisturbed circulation and circulation with localized turbine drag (scenario A).

Since the additional turbine drag significantly reduces meridional velocity in the Gulf Stream, and both Coriolis force and natural drag force are linearly related to the velocity magnitude, a corresponding reduction in Coriolis force in zonal direction and reduction in natural drag in meridional direction is seen in Figure 4.13. However the added turbine drag compensates for some of the reduction in natural drag, and therefore a significant change in total drag does not occur. It is observed from Figure 4.13 that addition of turbine drag reduces the pressure gradient in the middle of the western boundary, which consequently modifies the sea surface level. Once integrated, the pressure gradient can provide the sea surface elevation change due to the addition of the turbine drag. Figure 4.14 shows the undisturbed sea surface level (Figure 4.14a), sea surface level with additional turbine drag (Figure 4.14b) and their difference (Figure 4.14c). In the region with additional turbine drag, a significant drop ($> 0.5m$) in the sea surface level is observed. The sea surface level elsewhere sees a negligible rise to maintain the basin-wide water mass balance.

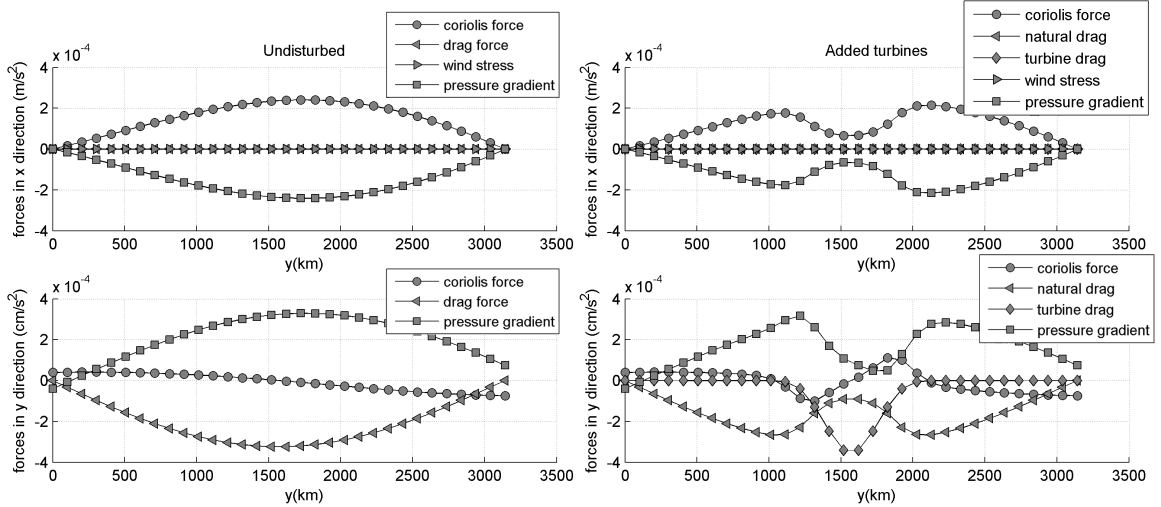


Figure 4.13: Force balance along the western boundary layer ($x \approx 2km$) for (a) undisturbed case and (b) the case with localized turbine drag (scenario A).

The changes in zonal and meridional velocities along the western boundary are also inferred from the streamline patterns, which highlight the redirection of the Gulf Stream due to the additional turbine drag (Figure 4.15). The streamlines in the vicinity of the turbine region are affected by the turbine drag. The meridional velocity component decreases and the relatively weaker zonal component changes direction, resulting in bending of the streamlines within the turbine region. Current flow redirects eastward instead of going straight north to avoid the high drag region. In a physical interpretation, the Gulf Stream flow could ultimately avoid flowing through the Florida Strait by rerouting flow along the east of the Bahamas if the drag force in the Florida Strait significantly increases due to turbines.

The local energy balance equation (Equation 4.16) is shown in Figure 4.16 for each term with localized turbine drag applied for Scenario A. Extremely high energy dissipation by turbines in the middle of the western boundary is observed, as expected. The highest natural dissipation occurs at the immediate up and down streams of the turbine region along the western boundary. The presence of localized turbine drag has very negligible impact on the energy balance outside the turbine region. Near the southern and northern boundaries, the energy balance is similar to the undisturbed case, primarily between energy production by wind stress and energy adjustment by the pressure gradient with natural

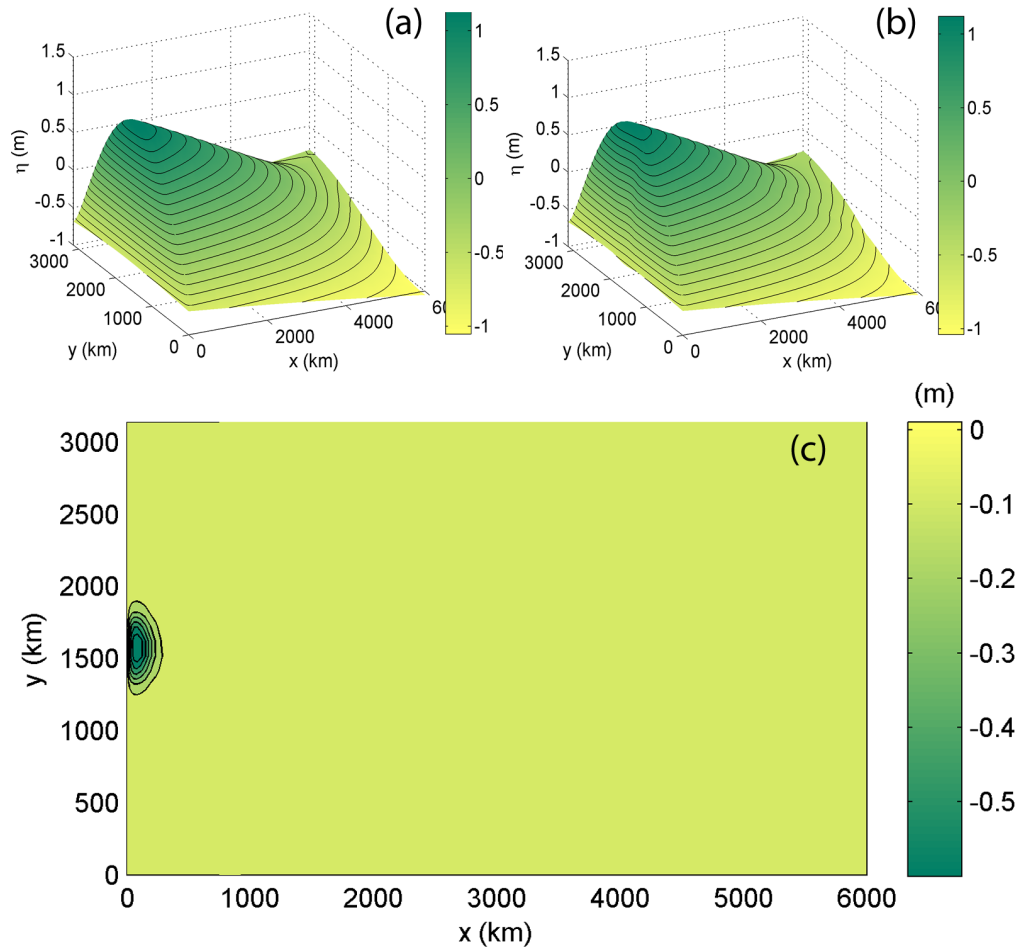


Figure 4.14: Ocean surface elevation with lines of constant pressure for (a) undisturbed case, (b) case with additional turbines, and (c) the sea surface change after additional turbine drag is added.

dissipation playing a minor role. Overall, the energy production by the wind stress is very similar to the undisturbed case except for two regions approximately 100km eastward of the center of the turbine region. Because of the extra resistance from turbine drag, the zonal component of the current flow velocity in those two regions changes direction from westward to eastward. Therefore currents in that particular region change from moving along the wind to against the wind, resulting in negative energy production by wind stress in those two particular regions, effectively slowing down the currents in those two small areas. Away from the southern and northern boundaries, the energy production by wind stress reduces due to decreased wind stress. Close to the western boundary, the natural

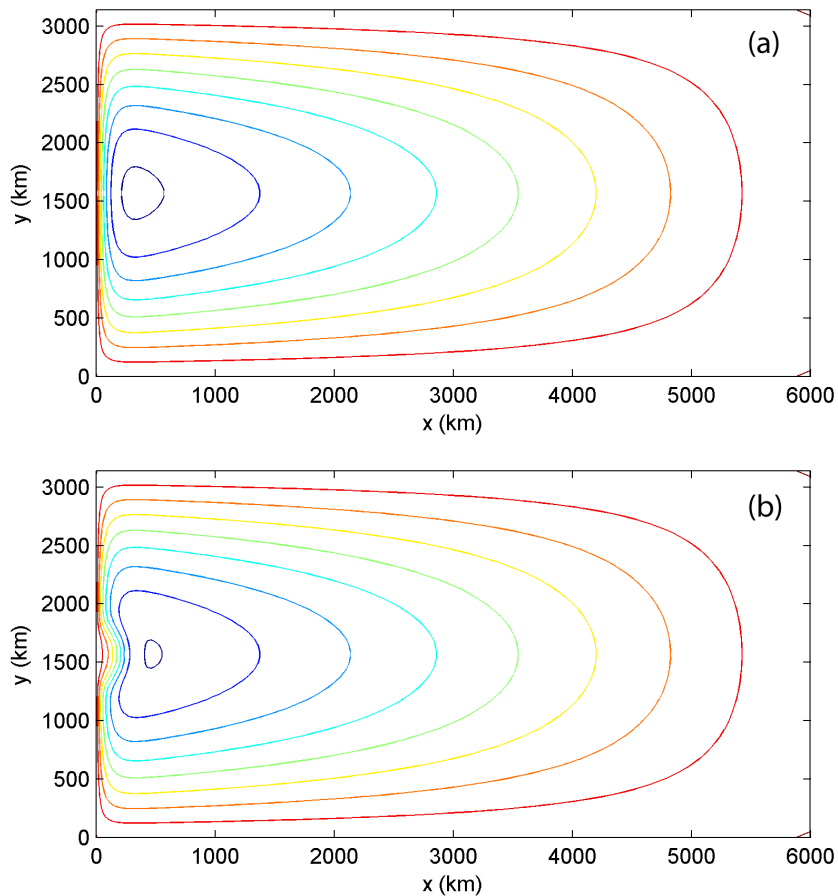


Figure 4.15: Streamlines for (a) undisturbed circulation, (b) circulation with localized turbine drag.

dissipation rate grows significantly in response to increased current velocity. Within the western boundary dissipation from natural friction and turbines takes more weight in the energy balance while energy production by wind stress becomes less significant. As a result, the pressure gradient adjusts accordingly to keep the local energy balanced by adjusting sea surface level, resulting in a local sea surface elevation drop shown in Figure 4.14. Local energy production by wind stress and local energy dissipation remain imbalanced. The pressure gradient functions to redistribute energy so that energy remains locally balanced. The peaks of work done by pressure gradient occur at the same locations where natural dissipation is the highest.

The addition of localized turbine drag significantly affects the residual energy flux in the circulation. The effect is evaluated by looking at the changes of residual energy flux through

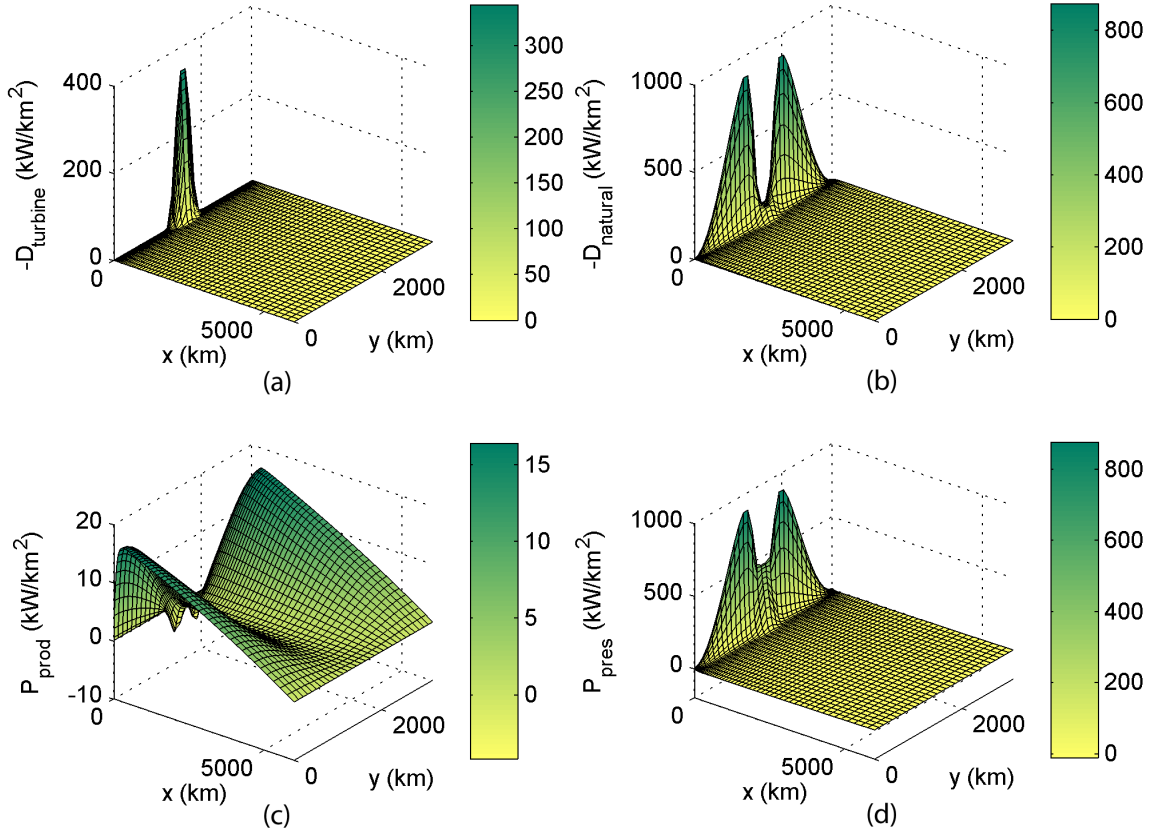


Figure 4.16: Spatial variation of each term from Equation 4.16 with localized turbine drag (scenario A): (a) density of energy dissipation by turbines; (b) density of natural energy dissipation; (c) density of energy production by wind; (d) work done by pressure gradient.

different cross-sections of the circulation with different levels of energy dissipation. Figure 4.17a shows the undisturbed streamlines with multiple cross-sections and Figure 4.17 shows the residual kinetic energy flux through individual cross-section. The residual energy flux drops significantly in the western boundary as turbine drag coefficient increases. As the turbine drag coefficient gradually increases, the peak residual energy flux shifts from the middle of the boundary (zero degree) toward approximately 40-60 degrees, corresponding to the locations with the strongest residual current speed shown in Figure 4.12.

The effects of localized turbines in the different scenarios share obvious similarities, but they are also physically distinct in several aspects. Due to conservation of mass, the volume flux through each cross-section stays constant for each particular case. Figure 4.18

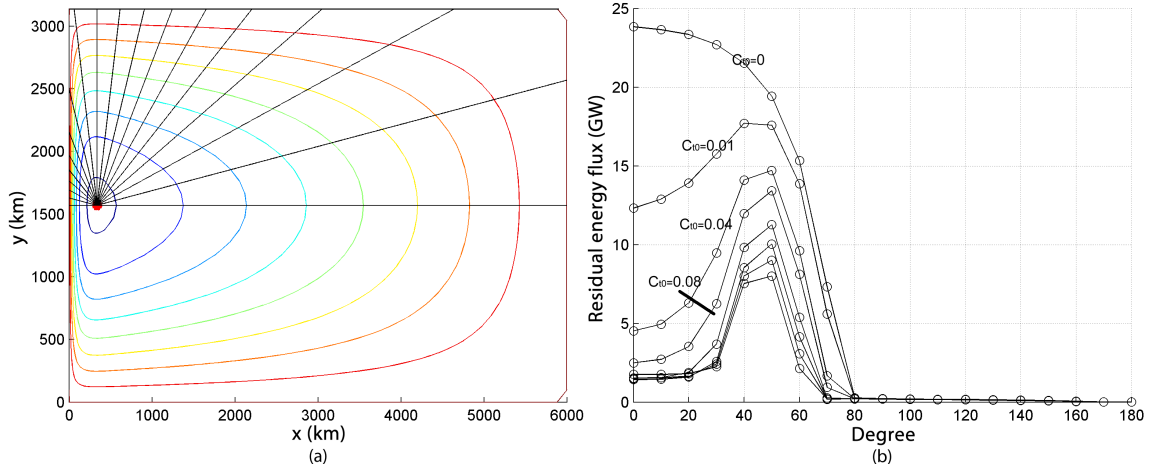


Figure 4.17: (a) Undisturbed streamlines with multiple cross-sections every 10 degrees, (b) residual energy flux for each cross-section on left with different level of localized energy dissipation from the Gulf Stream by turbines.

shows the residual volume flux with different turbine drag coefficients for scenarios A-E and the case with uniform drag coefficient. When the turbine region is relatively small (e.g. scenarios A and B), the residual volume flux is mostly sustained even if turbine drag coefficient increases significantly. However, when the turbine region becomes much larger, a noticeable drop in residual volume flux is observed, and the residual volume flux curve is approaching the curve associated with uniform turbine drag coefficient, in which case a significant decrease in residual volume flux occurs with increased turbine drag coefficient.

Figure 4.19a shows the energy input in the system and Figure 4.19b shows the natural dissipation for different scenarios. For scenarios with small turbine region (e.g. scenarios A and B), the energy input remains almost constant, similar to the residual volume flux. The natural dissipation drops slightly with increased turbine drag coefficient. As the turbine region increases, the energy input starts to drop more rapidly with the turbine drag coefficient and approaches the case associated with uniform turbine drag coefficient. A similar trend is observed for natural dissipation.

It is noted from the previous discussion that the energy input from the wind stress is predominantly on the southern and northern boundaries where the wind is the strongest. The impact of turbines is primarily confined in the turbine regions with negligible far field effect. For cases with relatively small turbine regions, the additional turbine drag does not

extend far into the southern/northern boundaries such that no significant flow reduction occurs in the areas with the primary energy production. Therefore the energy input does not change significantly, neither does the residual flow rate. As the turbine region grows much larger, the region with reduced flow also grows accordingly and extends further both to the south and north, causing energy production from wind stress to decrease. Therefore, a significant drop in energy input, as well as natural dissipation is observed. This also leads to considerably reduced flow rate. The extreme case with uniform turbine drag coefficient slows the flow universally across the entire basin resulting in a significant reduction in energy production rate. The residual flow rate is consequently reduced accordingly.

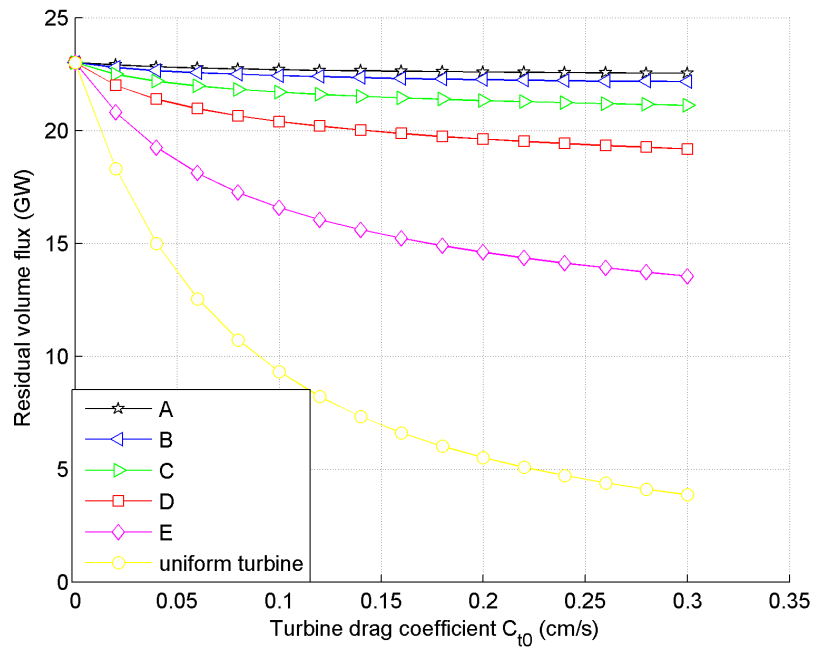


Figure 4.18: Residual volume flux as a function of peak turbine drag coefficient C_{t0} for different scenarios.

4.8 Total Available Power from Undisturbed Power Density

The previous power estimates provide the theoretical upper limit for recoverable energy resource from the Gulf Stream system for various scenarios. From a practical point of view, it is helpful to quantify the undisturbed kinetic power from hypothetical turbine arrays deployed in similar areas to determine the validity of the theoretical approach. This will

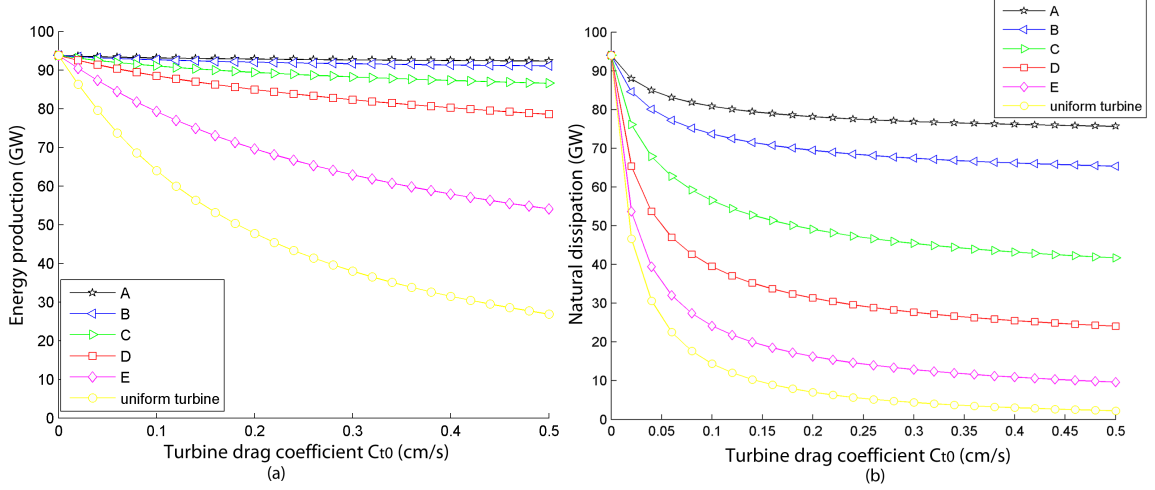


Figure 4.19: Changes of (a) energy production, and (b) natural energy dissipation in the circulation with turbine drag coefficient for different scenarios.

also help to determine the approximate size and capacity of arrays necessary to extract the maximum theoretical power. To examine the undisturbed kinetic power from hypothetical turbine arrays, it is assumed that turbines are uniformly deployed 50 m below the sea surface in the Gulf Stream and current velocities from the database are used to calculate the power. The principle velocity component in the Florida Current is northward along the channel, and the undisturbed kinetic power (P_k) from this turbine array is estimated using

$$P_k = \sum \frac{1}{2} \rho |V|^3 E_f A_s A_c N \quad (4.32)$$

where V is the velocity from the HYCOM GoM simulation at the assumed turbine depth, ρ is the water density (1025 kg/m^3), E_f is the Efficiency (40%), A_s is the swept area of device (400 m^2), A_c is the surface area of computation cell ($\sim 16 \text{ km}^2$) and N is the number of devices per unit surface area ($1/1 \text{ km}^2$) corresponding to 1 km spacing between devices. Open ocean turbine technology is not yet fully developed and tested; therefore it is not possible to obtain all the technological details of turbines to be used for the Florida Current. Estimates are based on assumed turbine parameters, which are subject to change but any modification would produce a corresponding linear change in the total power estimate.

In the first case, the turbine region is selected within a box area spanning from Florida to the Bahamas (Figure 4.20). Assuming turbines are uniformly deployed in this area with

the assumed parameters, the mean annual kinetic power from this hypothetical turbine array is 5.6 GW with the number of devices on the order of 35,000 in place, making the mean power per device approximately 0.16 MW.

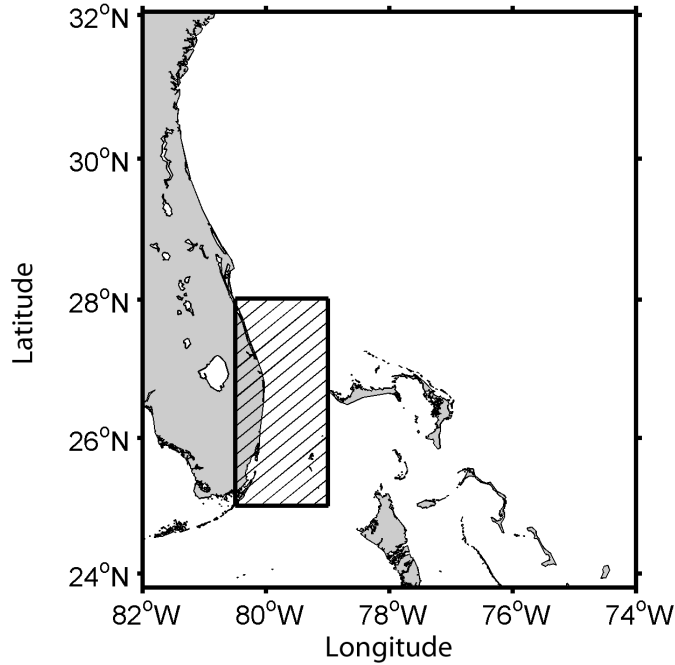


Figure 4.20: The area in the Florida Current where the hypothetical turbine array will be deployed.

The Florida Current's very strong monthly variability is reflected in the total kinetic power from the hypothetical turbine array as shown in Figure 4.21a. The peak power occurs in July and reaches more than 7 GW, and its lowest power occurs in November and is about 4.6 GW. That results in maximum power per device of about 0.2 MW in July and minimum power per device of about 0.13 MW in November.

To make the estimate more realistic, it is reasonable to assume the devices are only deployed in areas with high current velocity. From a technological point of view, most devices require a minimum cut-in flow speed at which devices will start producing power. Therefore devices should only be deployed in areas where the mean speed exceeds a certain threshold. For this analysis the threshold is set to 1 m/s which results in turbines being deployed in the areas with black dots in Figure 4.22. The approximate surface area of the turbine region in this case is $2.0 \times 10^4 \text{ km}^2$.

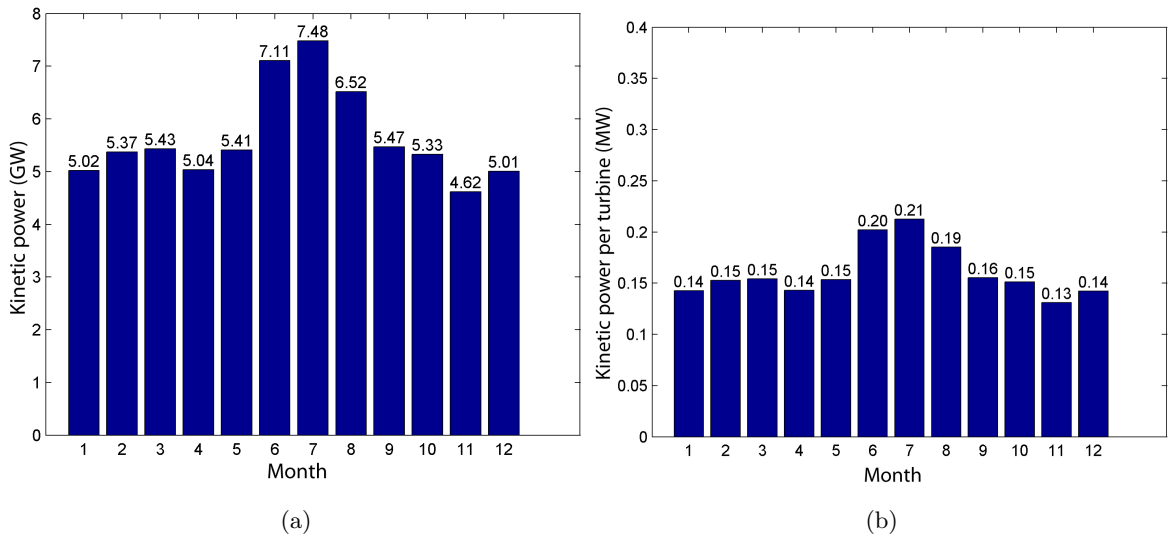


Figure 4.21: Monthly variation of (a) total kinetic power and (b) power per device from the hypothetical turbine array.

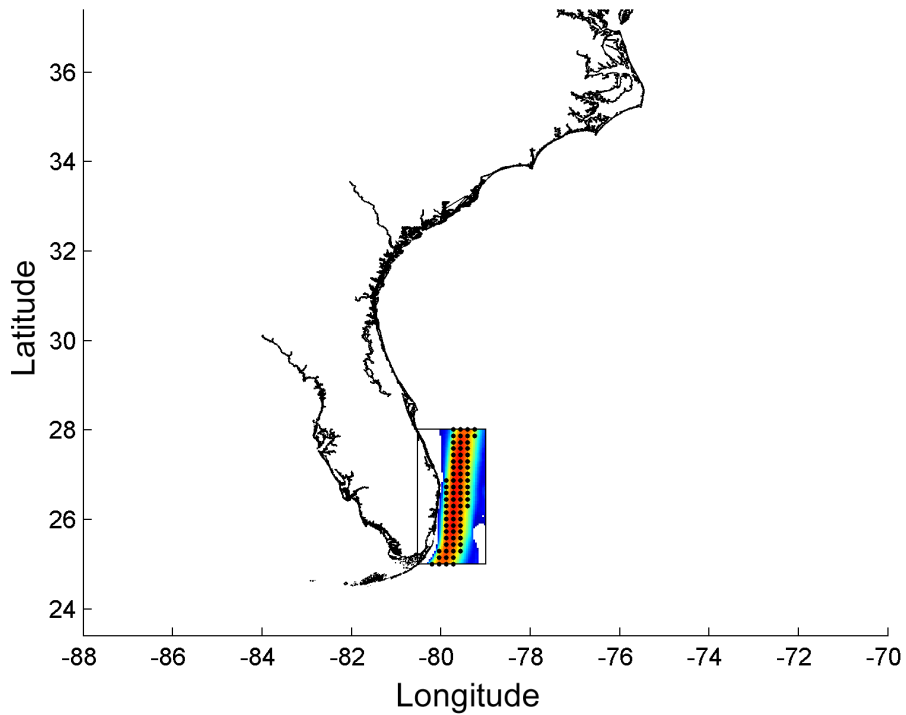


Figure 4.22: Area with black dots representing the area with mean current speed exceeding 1 m/s.

Applying the threshold for minimum current speed, the mean kinetic power slightly drops to about 5.2 GW corresponding to a decrease around 7% (Figure 4.23a). However, the number of devices is reduced by nearly half from roughly 35,000 to 18,000, thereby increasing the mean power per device to about 0.28 MW (Figure 4.23b). This represents nearly a 70% increase in power per device from the original scenario. The maximum power per device increases to 0.37 MW in July and the minimum increases to about 0.23 MW in November. Therefore this is a much more cost effective and thus realistic deployment scheme resulting in much higher per device power without significantly reducing the total power.

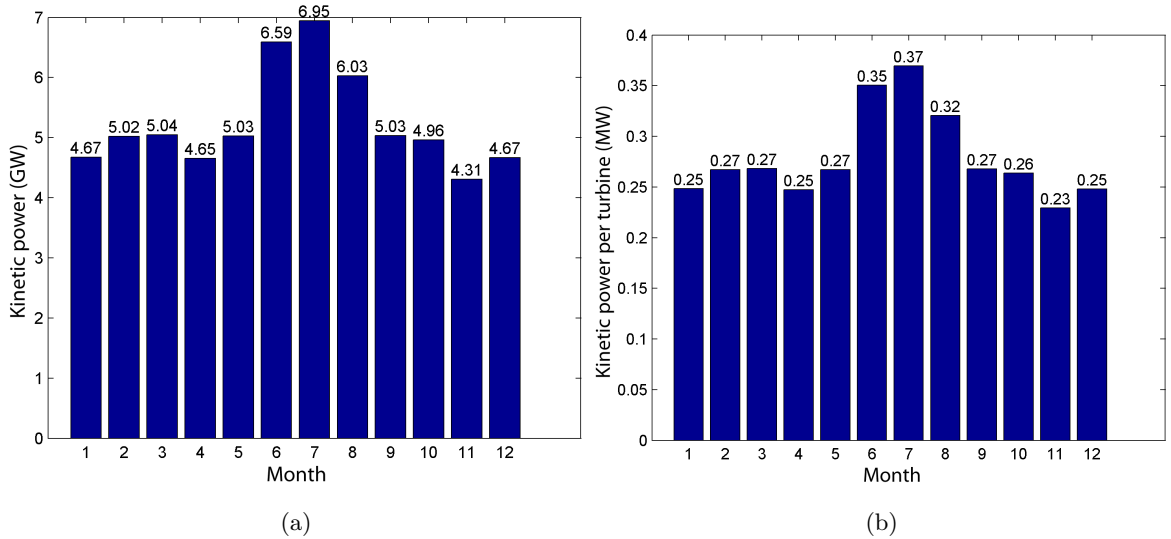


Figure 4.23: Monthly variation of (a) total kinetic power and (b) power per device with devices only deployed in areas with mean speed exceeding 1 m/s.

We further extend the turbine region beyond the box limit to a larger area ($\approx 4.5 \times 10^4 \text{km}^2$) with the turbines still only deployed in areas with mean speeds greater than 1 m/s (Figure 4.24a). In this case the average total kinetic power from the turbines increases to approximately 8.0 GW (Figure 4.24b), and the turbine number increases to the order of 30,000 and the average power per device decreases to about 0.26 MW. If the turbine region is expanded to include the offshore area of Cape Hatteras (Figure 4.25a), the surface area of the turbine region increases to about $1.4 \times 10^5 \text{km}^2$, and the total kinetic power goes up to

about 15.4 GW (Figure 4.25b). In this case, the turbine number goes up to approximately 88,000 and the average power per devices drops to about 0.17 MW.

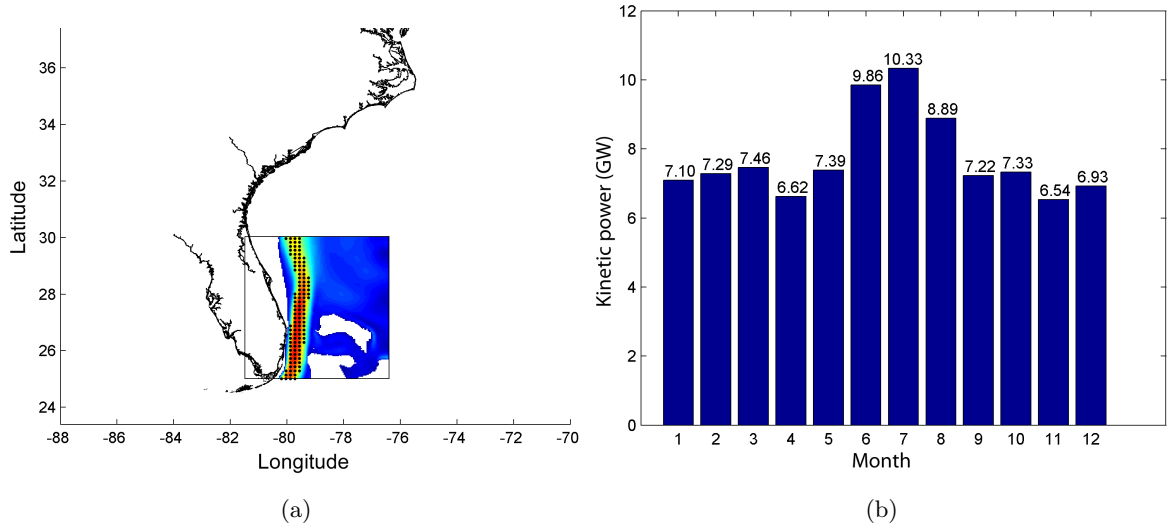


Figure 4.24: (a) The turbine region including sections up and down stream of the Florida Current, and (b) the monthly variation of total kinetic power.

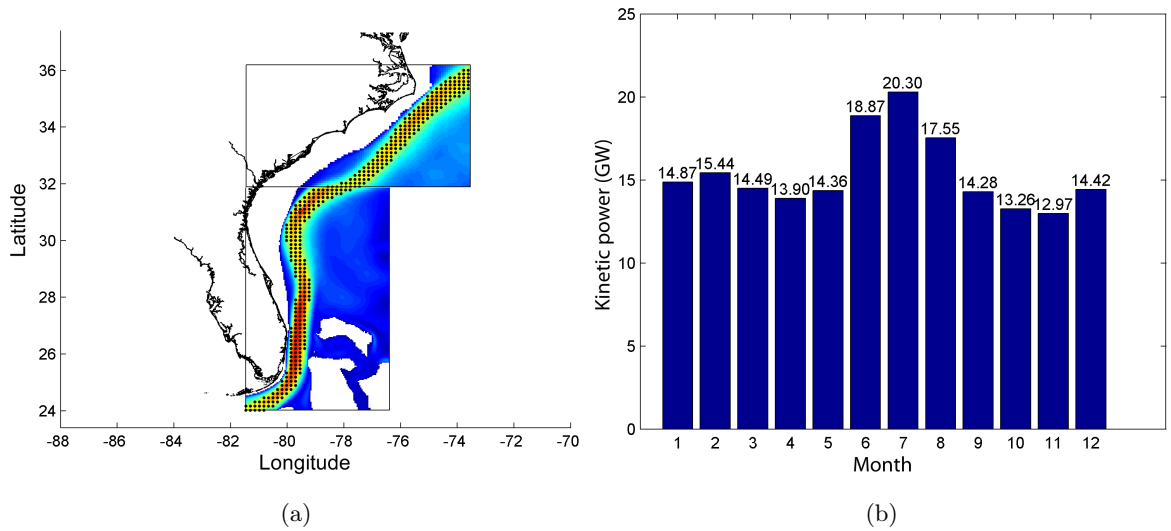


Figure 4.25: (a) The turbine area including offshore of Cape Hatteras, and (b) the monthly variation of total kinetic power.

Table 4.3 compares the power estimates from the previous chapter with the power estimate based on undisturbed kinetic power for three different scenarios with similar surface areas of the turbine region. Scenario A in the previous subsection has a similar area of turbines with the first case here, and the estimated power is also very similar. Scenario B and C from the previous subsection are comparable to the second and third cases here regarding the area of the turbine region. The comparison shows that the theoretical power limit is practically achievable by the commonly used approach based on undisturbed power density when proper turbine parameters are used. However, the estimate of P_k carries uncertainty and could vary significantly by adjusting the turbine parameters. In the meantime, the estimate of P_k based on undisturbed power density is only meaningful when the number of turbines and the cumulative effects on the existing flow are small. Velocity will be reduced when large amount of energy is extracted and larger number of turbines will be needed to extract the same amount of power. Therefore the estimate of P_k based on the undisturbed velocity field is questionable when a large number of turbines is used.

Table 4.3: Comparing power estimate in theory with the estimate based on undisturbed kinetic power.

	Approx. surface area of turbine region (km^2)		Estimated power (GW)	
	Theoretical model	Undisturbed kinetic power estimate	Theoretical model	Undisturbed kinetic power estimate
Scenario A	1.8×10^4	2.0×10^4	5.1	5.2
Scenario B	4.3×10^4	4.5×10^4	10.1	8.0
Scenario C	1.7×10^5	1.4×10^5	18.6	15.4

4.9 Total Power Summary

The ocean current energy potential from the Gulf Stream system has been estimated by investigating the theoretical energy balance of a simplified quasi-geostrophic ocean circulation model, and the theoretical upper limit of recoverable energy resource is evaluated as the energy dissipation from additional turbine drag. The analysis has shown that considering extraction over a region comprised of the entire Florida Current portion of the Gulf Stream system, the average power dissipated ranges between 4-6 GW with a mean around 5.1 GW. This corresponds to an average of approximately 45 TWh/yr. However, if the extraction area comprises the entire portion of the Gulf Stream within 200 miles of the US

coastline between Florida and North Carolina, the average power dissipated ranges between 15.1-22.5 GW with a mean around 18.6 GW or 163 TWh/yr. As defined by the National Research Council (NRC, 2013), the theoretical resource is the amount of power contained in the natural system. The values provided here may be regarded as the theoretical resource. However, the technically recoverable resource is defined as the resource extraction realizable within the limitations of presently available devices and site-specific resource intensities, and should be significantly below the theoretical estimate provided here. Such limitations include wake losses, turbine and transmission efficiencies, and other engineering and technological constraints. The exact percentage of the theoretical resource that can be converted into electricity considering turbine related efficiencies needs more research to determine. However, providing an estimate by assuming a 30% power conversion efficiency for energy removal from the flow to electrical power (Bahaj and Myers, 2003) yields an average potential for electricity production of about 1.5 GW from the Florida Current and 5.6 GW from the entire US portion of the Gulf Stream system or 13 and 49 TWh/yr, respectively.

CHAPTER V

MODELING EFFECTS OF POWER EXTRACTION WITH HYCOM

A 2D analytical model was created and calibrated as described in the previous chapter to evaluate the energy potential from ocean currents in the Gulf Stream in theory. This 2D model, although capable of solving for the bulk flow, is insufficient in resolving time variations of the flow field. The simplification of the 2D ocean model also makes it impossible to include the impact of actual coastline and bottom topography on the currents. A full numerical modeling considering both spatial and temporal changes of ocean currents due to power extraction is necessary to gain a more realistic representation of the ocean circulation and a more precise evaluation of the effects of power extraction. In this chapter, a full numerical simulation of the ocean circulation in the North Atlantic ocean is performed with HYCOM. The power extraction with turbines is incorporated in the model's momentum equations as an extra momentum sink and the effects of power extraction is studied.

5.1 Model Configurations

HYCOM is a finite difference, hydrostatic, Boussinesq primitive equation ocean circulation model evolved from the Miami Isopycnic Coordinate Model (MICOM)(Bleck, 2002; Halliwell, 2004), which has already been subjected to numerous ocean circulation related studies (e.g. Chassignet et al. (1996); Roberts et al. (1996); New and Bleck (1995); Xu et al. (2012); Yao and Johns (2010)). HYCOM uses orthogonal grids in the horizontal and hybrid coordinate in the vertical. The vertical coordinate is isopycnal in the open, stratified ocean, and smoothly transitions to a terrain-following coordinate in shallow coastal regions. In the mixed layer or unstratified seas, it uses z-level coordinate. The hybrid coordinate system provides flexible and dynamic options for different regions of the ocean, and extends the geographic range of applicability of traditional ocean circulation models. Several different vertical mixing algorithms are readily included in HYCOM, including the KPP scheme (Large et al., 1994), the Kraus-Turner scheme (Niiler and Kraus, 1977), the Mellor-Yamda

level 2.5 scheme (Mellor and Yamada, 1982) and the dynamic instability scheme of Price et al. (1986). The model is fully parallelized and can be run with multiple processors using shared or distributed memory architectures such as Open Multi-Processing (OpenMP) or Message Passing Interface (MPI).

The domain is selected to include the majority of the North Atlantic ocean, extending from 98W to 20E in longitude and from 10S to 55N in latitude as shown in Figure 5.1, such that the model is able to capture the entire subtropical gyre of the Gulf Stream system. The grid points are projected onto a mercator projection. Considering the computational resources available to this study, the horizontal resolution is set to be 1/5 degree at the equator, which is fine enough to resolve the Gulf Stream current. The number of vertical layers is set to be 22. For each vertical layer, a target isopycnal is assigned. The model continually checks and compares the grid point with its target isopycnal, and move the grid point vertically to improve alignment. The target densities for the vertical layers range from 18 to 28 in sigma unit. In shallow regions vertical grid migration is constrained to avoid excessive crowding of different layer surfaces, and grid points are allowed to remain at fixed depths. In the mixed layer, grid points are positioned vertically to allow smooth transition of layer surfaces from isopycnal to constant depth surfaces. The minimum layer depth is set to 3 m. Five-minute resolution global ocean depth and land surface elevation data is used to construct the bathymetry of the computational domain. The ocean depth dataset is developed from multiple data sources and compiled at NGDC (National Geophysical Data Center)(NGDC, 1995). The 5-minute bathymetry data was first interpolated to HYCOM bathymetry, and the ocean depths at the HYCOM grid was averaged over (3×3) grid patch for smoothness. In order to simplify the model domain and remove oceans and inland seas with negligible impact on the subtropical circulation, the Pacific Ocean and the Mediterranean Sea have been landmasked (or removed) from the model domain.

The model domain has closed eastern and western boundaries, and has the open ocean boundary located in the southern and northern ends. At the closed lateral boundaries, namely the coastlines, a no-slip boundary condition is applied. At the open lateral boundaries (i.e. the southern and northern lateral boundaries), the boundary conditions are

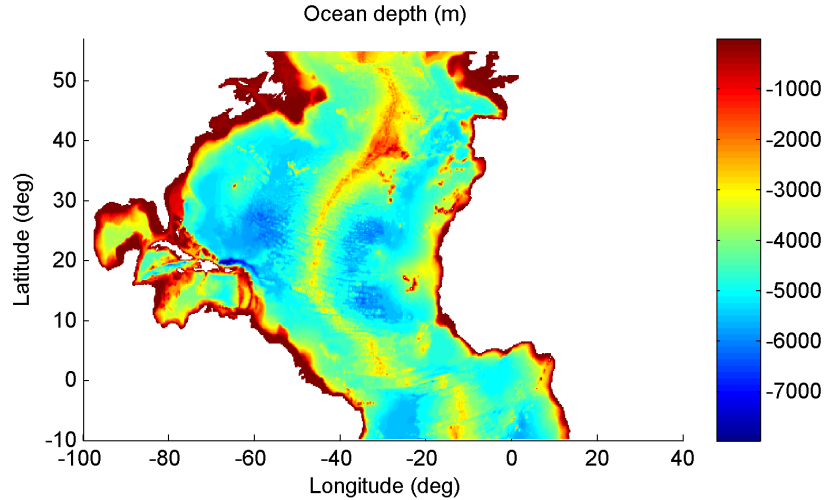


Figure 5.1: HYCOM computational domain with bathymetry

derived from “closing” the open boundaries by forcing zero flow across the boundaries but to strongly relax temperature and salinity to climatology data near the open boundaries. This approach may cause non-physical solution near the boundary, but is usually suitable for modeling an ocean-size basin and the solution outside the relaxation zone is usually very good. For the model configuration in this study, the domain is selected to reach more than 10 degrees farther north and south of the interested area (i.e. the Gulf Stream system), and therefore it is reasonable to use this type of boundary condition and assume that the non-physical solution near the boundary has negligible effects on the main circulation. Within a buffer zone of about 5 degrees from the northern and southern boundaries, the model potential temperature and salinity are restored to a monthly ocean climatology obtained from the Naval Research Laboratory (NRL) LEVITUS climatology files (Levitus and Boyer, 1994).

The atmospheric forcing includes surface momentum flux from wind stress, heat flux and fresh water flux. Monthly climatological forcing from the European Center for Medium-Range Weather Forecasts reanalysis (ERA15 (Gibson et al., 1997)) is used to provide surface flux. The ERA-15 archive contains global analyses for all relevant weather parameters from year 1979 to 1994. Surface heat and mass fluxes in HYCOM are first absorbed in the first model layer, and then are parameterized using the bulk formula by Kara et al. (2000). The ocean state is initialized by the salinity and temperature fields interpolated

from the Levitus climatology (Levitus and Boyer, 1994). The North Atlantic subtropic gyre is primarily driven by surface wind stress, and Figure 5.2 shows the annual mean surface wind stress on the North Atlantic Ocean with prominent northeast trade wind in the tropics and westerlies in the middle latitude driving the general circulation. Although the mean transport of the Gulf Stream represents the northward return flow of wind-driven southward flow over the interior of the basin, the seasonable variation of the Florida Current is largely due to the variation of the meridional wind stress along the coast (Boning et al., 1991). Figure 5.3 shows the monthly mean surface wind stress for both July and January in the Florida Current region for comparison of the different wind patterns from summer and winter. It is shown that the meridional wind stress along the coast is dominated by a northward component blowing along the Florida Current in summer time, and by a southward component blowing against the current in winter time. To get a closer look at the wind stress variability along the coast, three locations (F1, F2 and F3) are selected along the coast (see Figure 5.3) and the monthly variation of the wind stress at those locations are plotted in Figure 5.4. It is shown in Figure 5.4 that at all three locations the meridional wind stress is northward from May to August, and southward from September to February. This is in agreement with field measurement data and ocean model data that both show stronger transport in summer in the Florida Current. The wind strength along the coast is also observed to increase as the latitude increases for these three locations.

The simulation was first performed on a Linux cluster computer located at Georgia Tech Savannah campus, which has 7 functional nodes. Each node has 3942 MB RAM and 4 Intel(R) Xeon(TM) CPU 3.20 GHz processors. For the baseline case (i.e. the undisturbed case), different time steps have been tested and the model using a combination of baroclinic time step of 240 sec and barotropic time step of 15 sec produces the most stable results without blowing up. A one-year simulation takes approximately 80 hours to complete using all 7 nodes. Five years of simulation was performed on this computational cluster before the cluster failed due to technical issues. The remaining simulations were completed on a HP Z820 workstation with 24 Intel(R) Xeon(R) CPU 2.00GHz processors. An additional

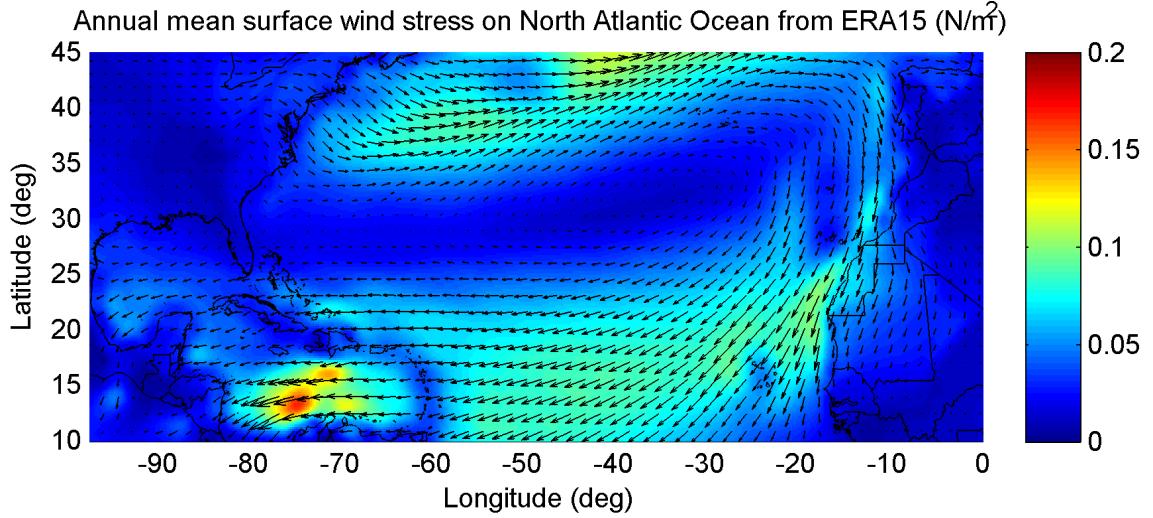


Figure 5.2: The annual mean surface wind stress on the North Atlantic Ocean derived from ERA15 dataset.

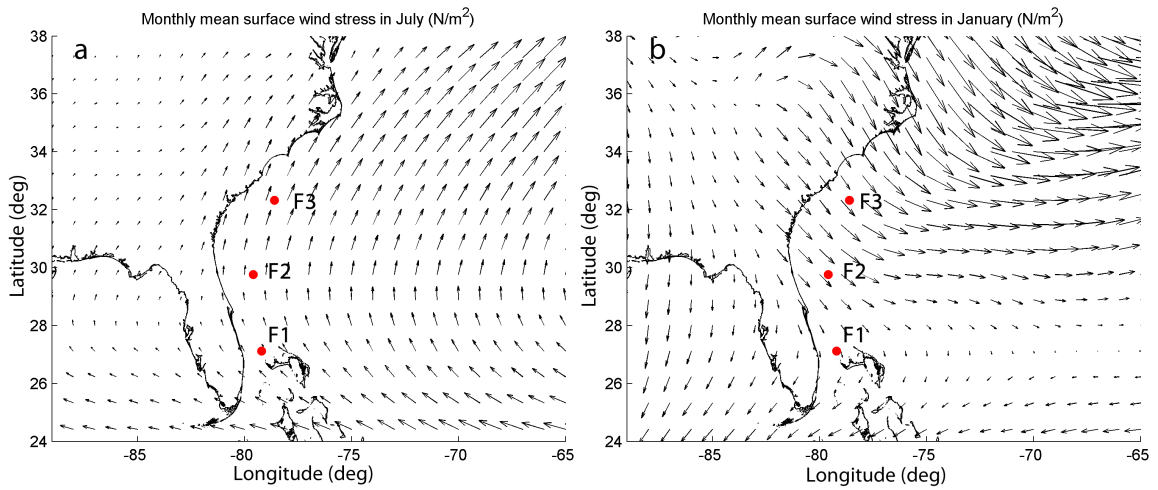


Figure 5.3: The monthly mean surface wind stress for the Florida Current from ERA15 dataset for (a) July and (b) January, with red dots showing the locations of F1, F2 and F3.

year of baseline case simulation was performed on the HP workstation with 20 CPUs taking approximately 60 hours to complete. For the cases with local power extraction, both baroclinic and barotropic time steps have to be further reduced to avoid the model blowing up, and the simulation for power extraction cases therefore takes much longer time on the HP workstation, approximately 100-400 hours per year.

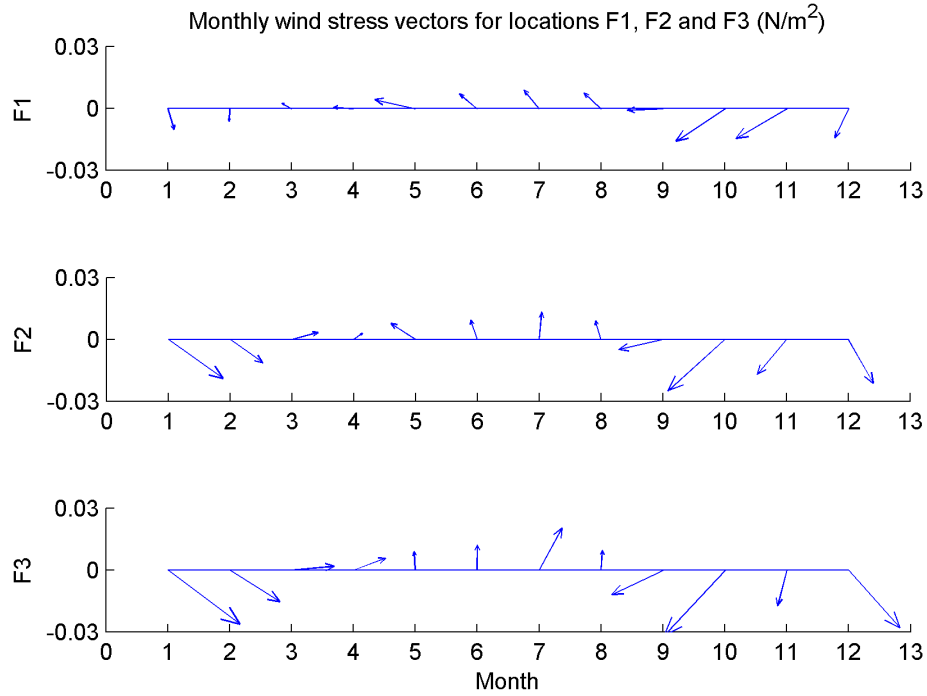


Figure 5.4: The monthly mean wind stress vectors of 12 months for 3 different locations (F1, F2 and F3) located along the U.S. east coast.

5.2 Baseline Results

The quasi-geostrophic currents in the North Atlantic ocean spin up and reach equilibrium fairly quickly. Figure 5.5 shows the evolution of the region-wide mean kinetic energy for 7 years of the baseline case run from a cold start as a proxy of the adjustment process. The region-wide mean kinetic energy starts with an initial spike, which comes from the initial relaxation to climatology at the open boundaries. The mean kinetic energy then decays and reaches a fairly stable state with fluctuations after approximately one year. Therefore the quasi-geostrophic currents are considered to have reached equilibrium state after 6 years of run based on Figure 5.5. A full year simulation is run for the 7th year as the baseline (or undisturbed) case. Cases with the power extraction by turbines are also run for the same 7th year, so that the effects of power extraction can be evaluated by comparing to the baseline case.

The model results in the baseline case show higher current speed and hence higher power

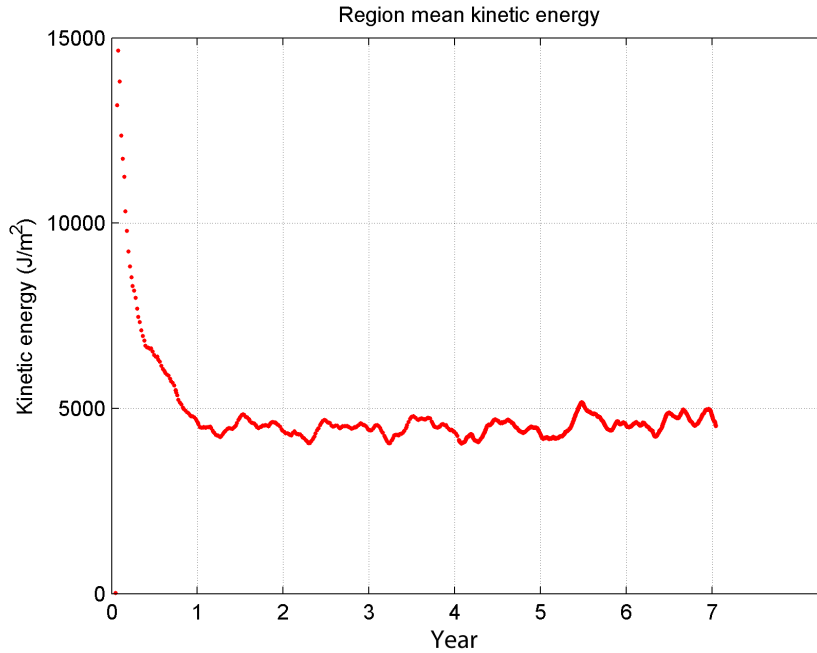


Figure 5.5: Time series of region mean kinetic energy.

density in the Gulf Stream current than ocean currents elsewhere, especially the portion of the Gulf Stream system within the Florida Strait region usually referred to as the Florida Current (Figures 5.6 and 5.7). The annual mean power density is calculated by finding the depth integrated average daily power density between surface and 200 m deep, and then averaging over 1 year of time. The annual mean surface current speed is nearly 2 m/s in the Florida Current, and the top 200m of the water column in the Florida Current features a mean power density up to 1500 W/m². The current flow with high power density is observed to flow northward along the U.S. east coast and starts to separate from the coast near Cape Hatteras.

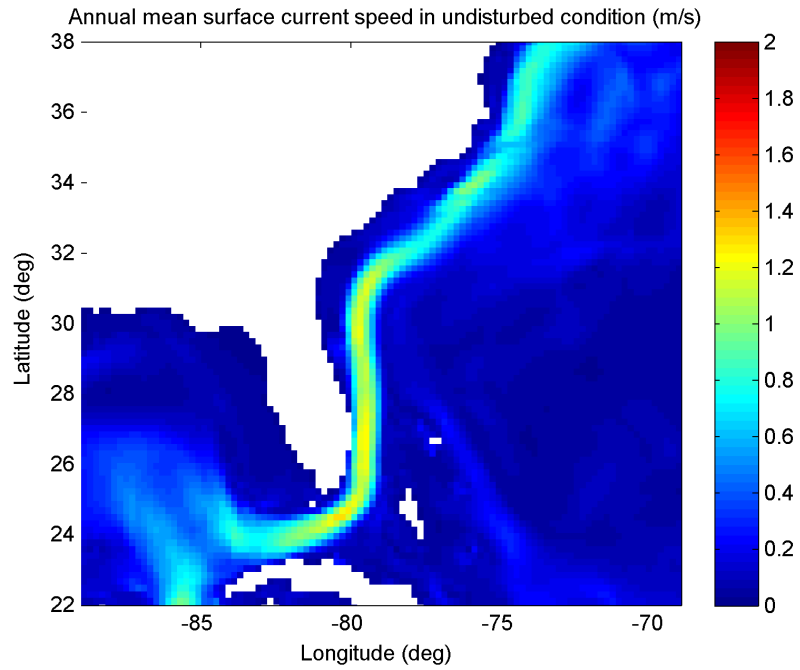


Figure 5.6: Annual mean surface current speed for undisturbed condition (m/s).

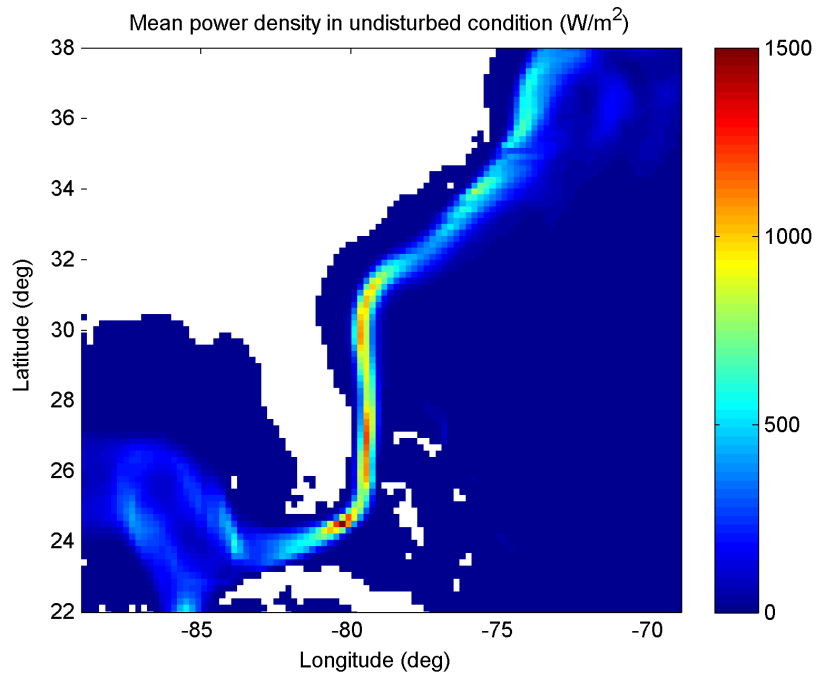


Figure 5.7: Annual mean power density of the top 200m water column for undisturbed condition (W/m^2).

The model results are validated against measurement data available in the Florida Strait in terms of its capability to reproduce bulk flow with reasonable strength in the Florida Current. The same submarine cable data that measures the volume transport in the Florida Strait channel used in previous chapters for validation purpose is also used here to compare with the volume flux calculated from the model results. Figure 5.8 shows the comparison of the monthly mean volume flux from both submarine cable measurement and from the model. The monthly mean volume flux from cable measurement is averaged from 7 years of cable data. The model result shows a very similar monthly variation of the bulk flow as the cable measurement and they have a correlation coefficient of 0.76 which implies high linear correlation. However, the model result shows an under-prediction in the mean volume transport of the Florida Current (24.7 Sv) compared with the cable data (31.3 Sv). The HYCOM GoM (1/25 deg horizontal resolution) data introduced in a previous chapter is shown to predict the volume flux fairly accurately, while the Global HYCOM which has a coarser horizontal resolution is found to also under-predict the volume flux in the Florida Current by a similar amount as this model (Neary et al., 2012). Such underestimation has also been documented by Duerr and Dhanak (2012). Therefore the error is very likely to be associated with insufficient horizontal grid resolution. However increasing horizontal resolution will require further reducing the baroclinic and barotropic time steps to comply with the CourantFriedrichsLewy condition. Therefore running simulations with higher horizontal resolution will require much longer computational time, or upgrading to more power computational hardware, which are not currently available. Therefore, it is anticipated that the power estimation from this chapter will be low. While we expect a lower power potential estimate from the model, the model results still provide sufficient data to shed light on the effects of power extraction from the Florida current on the flow field. Hence the discussions in this chapter focus more on the relative effects of the power extraction on the flow field than on estimating the total amount of power extraction.

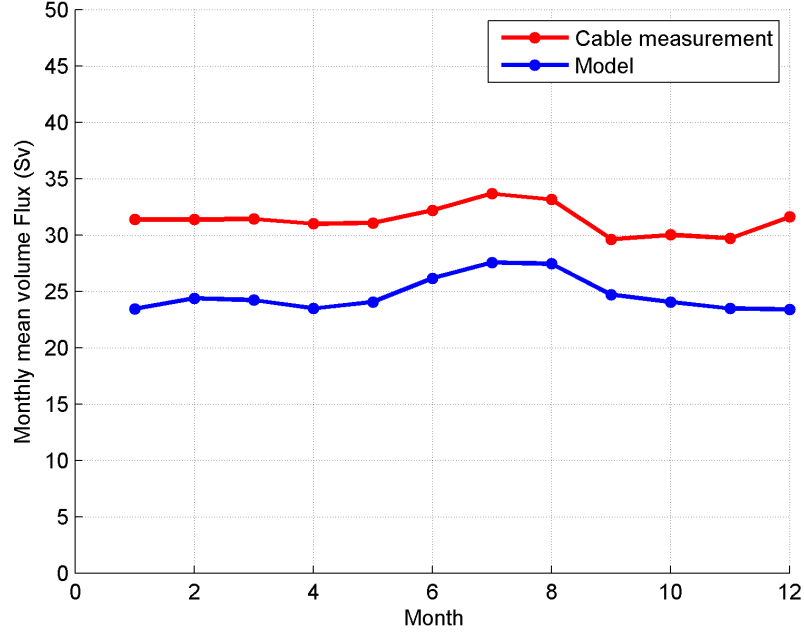


Figure 5.8: Monthly mean volume flux in the Florida Current from both model results (blue) and submarine cable measurement (red).

5.3 Modeling Turbines

Deploying an array of turbines into the flow field is expected to have both near and far field effects. In order to evaluate the effect of power extraction on the flow, the momentum equations of the model in locations where devices are to be deployed need to be modified. Additional momentum sink by the turbines is included in the governing equations at the computational cells where conversion devices are located. Applying the same method used by Defne (2010), the retarding force from turbines per unit cross-sectional area is

$$T_i = -\frac{1}{2}C_{ext}\rho u_i |\vec{V}| \quad (5.1)$$

where C_{ext} is the extraction coefficient, u_i is one velocity component ($i = x, y$), and $|\vec{V}|$ is the flow speed. The coefficient C_{ext} controls the amount of dissipation due to turbines in the computational cell. The retarding force per unit volume that is included into the model equations to simulate additional turbine drag is

$$T'_i = -\frac{1}{2} \frac{C_{ext}\rho}{\Delta h} u_i |\vec{V}| \quad (5.2)$$

where Δh is the model layer thickness, which varies with depth. The total extracted power by turbines from one vertical layer is then

$$P_l = - \sum_{i,j} \vec{T}_{i,j}^t \cdot \vec{V}_{i,j} \Delta x_{i,j} \Delta y_{i,j} \Delta h = \sum_{i,j} \frac{1}{2} C_{ext} \rho |\vec{V}_{i,j}|^3 \Delta x_{i,j} \Delta y_{i,j}. \quad (5.3)$$

where i and j are horizontal computational grid indices, $\Delta x_{i,j}$ and $\Delta y_{i,j}$ are horizontal grid spacings in x and y directions, and P_l is the extracted power from one computational layer. Δh is cancelled out in Equation 5.3. The total power extraction from the turbine farm will be the summation of Equation 5.3 from all layers:

$$P_{total} = \sum_l P_l = \sum_{i,j,l} \frac{1}{2} C_{ext} \rho |\vec{V}_{i,j}|^3 \Delta x_{i,j,l} \Delta y_{i,j,l}. \quad (5.4)$$

where l is the computational layer index.

Turbines should not be placed in the upper 50 m of water column to prevent navigational hazards, and they should not be placed in water deeper than 200 m since the majority of energy flux in the cross-section is concentrated in the upper 200 m of the water column (Duerr and Dhanak, 2012). Therefore, in the following experiments, additional momentum sink due to turbines is only added to computational cells between approximately 50 m and 200 m deep in the water, although the depth range of turbine deployment may not be exact given that the HYCOM model uses a combination of non-uniform coordinates including isopycnal, terrain-following and z-level coordinates in the vertical.

In this study, two different turbine layouts are discussed. One layout represents an extreme scenario in which the horizontal extent of the turbine region occupies the majority of the surface area in the Florida Current. The turbine region extends from about 79.8W to 79.2W in longitude, and from approximately 25.8N to 28.0N in latitude, covering a surface area of approximately $2.1 \times 10^4 \text{km}^2$. This is a hypothetical case dedicated to studying the extreme possible effects of energy extraction on the flow field. The other layout represents a more realistic scenario in which an array of turbines is deployed at approximately 60-100 m deep and extends from 80W to 79W in longitude covering a surface area of approximately $1.6 \times 10^3 \text{km}^2$. In latitude the array is located at 26.9N and covers the spacing of one grid cell (approximately 0.2 degree). The approximate layouts of turbines for two scenarios

are plotted in Figure 5.9. For each layout, two different extraction coefficients are used to investigate the effects of power extraction on the flow field: $C_{ext} = 0.2$ and $C_{ext} = 0.02$. The extraction coefficient C_{ext} is not equivalent to the turbine efficiency, therefore it does not represent the percentage of the undisturbed power being extracted. For a constrained flow, C_{ext} may even exceed 1. An explicit relationship with real turbine parameters is beyond the scope of this study, and therefore is not provided here. However, increasing this coefficient can be thought of as adding more turbines or increasing turbine size thereby increasing power dissipation and further reducing the flow velocity. Therefore cases with $C_{ext} = 0.2$ can be considered as having turbines more densely deployed than cases with $C_{ext} = 0.02$.

The power extraction is added into the model starting from the 7th year of the simulation. Considering the flow field needs to adjust to the additional turbine drag force to reach an equilibrium state again, the first 3 month of simulation with power extraction is not used for analysis. The analysis starts from April of the 7th year, and lasts one year until the end of the 3rd month of the 8th year. In this study, 4 different cases have been simulated. Cases 1 and 3 use the first turbine layout as shown in Figure 5.9a with different extraction coefficients. Cases 2 and 4 use the second turbine layout shown in Figure 5.9b with different extraction coefficients. A summary of power extraction details is given in Table 5.1. In this chapter, only the results from case 1 and case 2 are extensively discussed, and the results from the other cases are summarized at the end of the discussion.

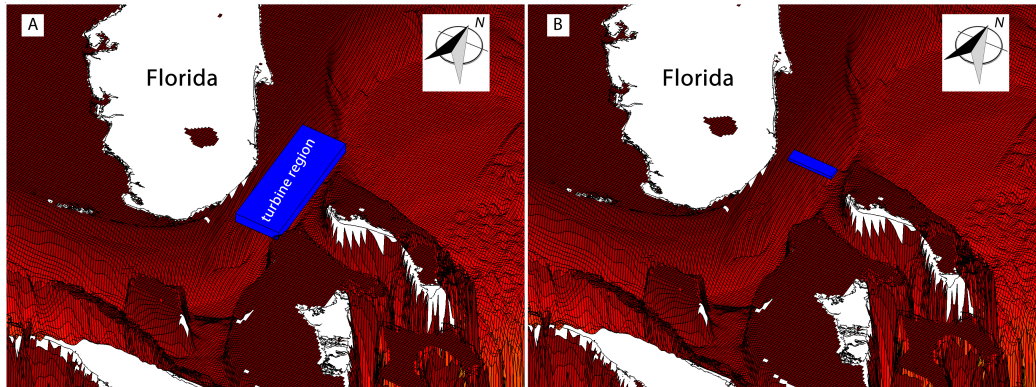


Figure 5.9: Two layouts of turbines in the Florida Strait with blue areas representing the approximate locations of turbine region; layout (a) is used in cases 1 and 3, while layout (b) is used in cases 2 and 4.

Table 5.1: Summary of 4 different power extraction cases.

Cases	Approx. surface area (km^2)	Approx. depth (m)	Ext. coef.	Mean power (GW)
case 1	$2.1 \times 10^4 km^2$	50-200	0.02	2.4
case 2	$1.6 \times 10^3 km^2$	60-100	0.2	0.4
case 3	$2.1 \times 10^4 km^2$	50-200	0.2	3.8
case 4	$1.6 \times 10^3 km^2$	60-100	0.02	0.06

5.4 *Effects of Power Extraction from the Florida Current*

The effects of the power extraction in the near vicinity of the turbine region as well as far fields are examined by analyzing the spatial and temporal changes in the mean power density, surface current speed, and water level for different power extraction cases. Since the cell size in the simulation is much greater than the size of commonly used turbines, the turbine resolution as well as interactions between turbines cannot be resolved in this simulation and therefore are not discussed here.

5.4.1 **Change in Mean Surface Current**

The effect of power extraction on the hydrodynamics of the flow field is analyzed through the change of surface current magnitude. Figure 5.6 already shows the mean surface current speed in undisturbed condition as the baseline case. Figure 5.10 shows the mean surface current speed in case 1 and the difference from the baseline. The rerouting of the surface current flow is very obvious from the comparison. The peak mean current speed drop in the Florida Strait is approximately 1 m/s, which agrees with the estimate from the analytical model result in the previous chapter. As the upper portion of the water way in the Florida Strait is partially blocked by the presence of the turbines, the surface flow entering the Florida Strait changes direction and moves toward the southeast to go through the channel between Cuba and the Bahamas. Further downstream it flows along the east coast of the Bahamas to the north and merges back with the original Gulf Stream. The ocean current speed increase on the east of the Bahamas due to the rerouting can be as high as 0.8 m/s. Therefore the current exiting from the Florida Strait slows down and the newly formed strong flow occurs to the east, resulting in a slight shift of the path of the Gulf Stream to the east. The surface current speed along the Gulf coast also features a relatively

insignificant drop no greater than 0.2 m/s.

For case 2, due to the lower strength of power extraction, a prominent rerouting of the surface ocean current does not occur (Figure 5.11). The effect of the power extraction has a much smaller spatial extent and most of the flow modification is located in the vicinity of the turbine region. Immediately downstream of the turbine region features the greatest current speed drop of about 0.6 m/s. Immediately upstream of the turbine region close to the Florida coast, a local increase in the surface current magnitude occurs. The surface current speed downstream of the turbine region on the right of the Gulf Stream path also increases as the flow seeks to bypass the area with high turbine resistance. The current speed increase reaches its peak of about 0.3 m/s to the east of the turbine region.

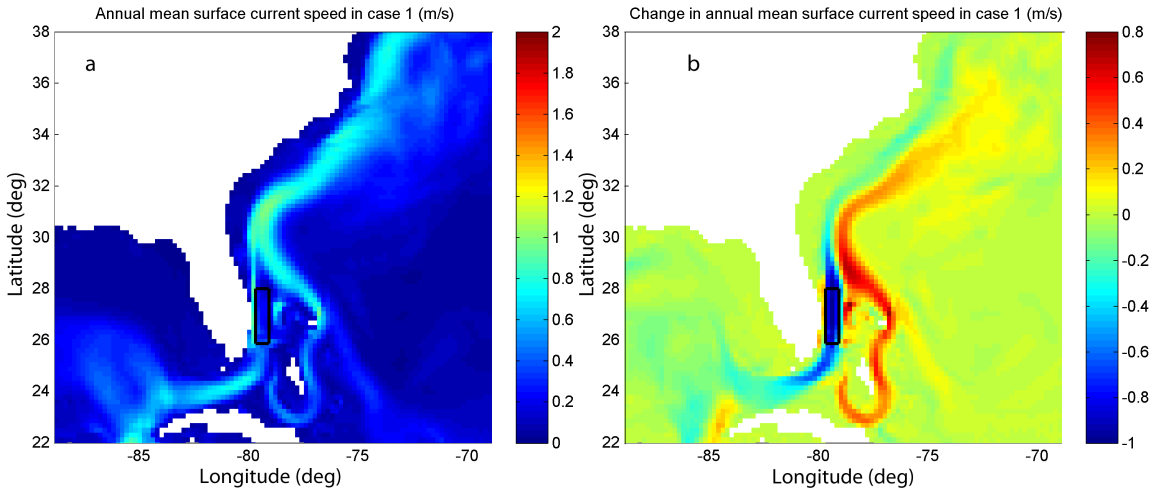


Figure 5.10: (a) Annual mean surface current speed in power extraction case 1, (b) change in mean surface current speed in case 1 relative to the baseline (m/s); black box outlines the location of turbines.

The impact of power extraction on the near-field hydrodynamics also features an obvious seasonable variability, which can be seen in Figure 5.12 for case 1 as an example. Figure 5.12 shows the difference between the mean surface current speed change in summer time and in winter time. It is clearly seen that the change of the mean current speed due to power extraction in the Florida Current and its immediate downstream is stronger in summer time compared to winter. The enhancement of the rerouted flow east of the Bahamas also features an apparent seasonable variability, stronger in summer and weaker in other times.

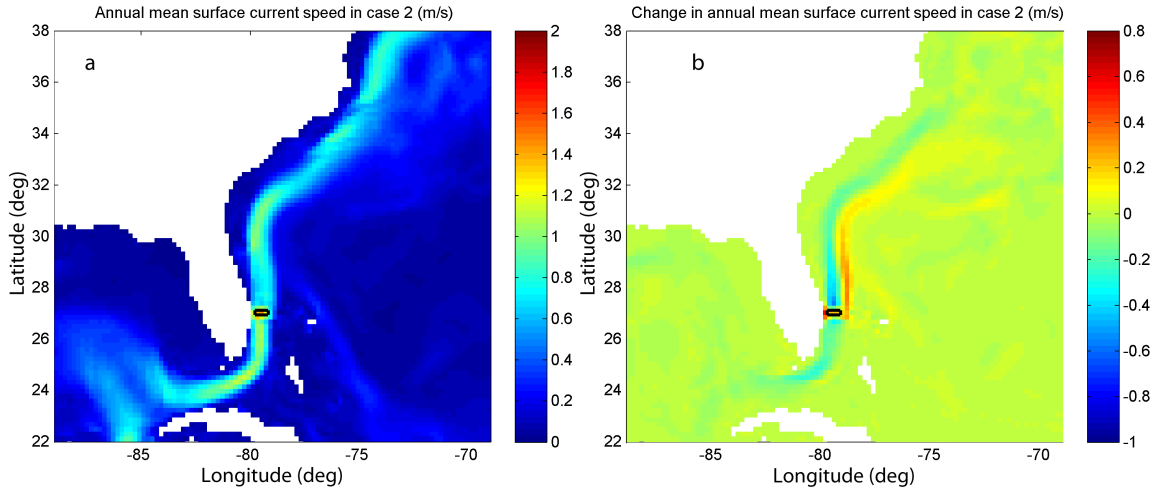


Figure 5.11: (a) Annual mean surface current speed in power extraction case 2, (b) change in mean surface current speed in case 2 relative to the baseline (m/s); black box outlines the location of turbines.

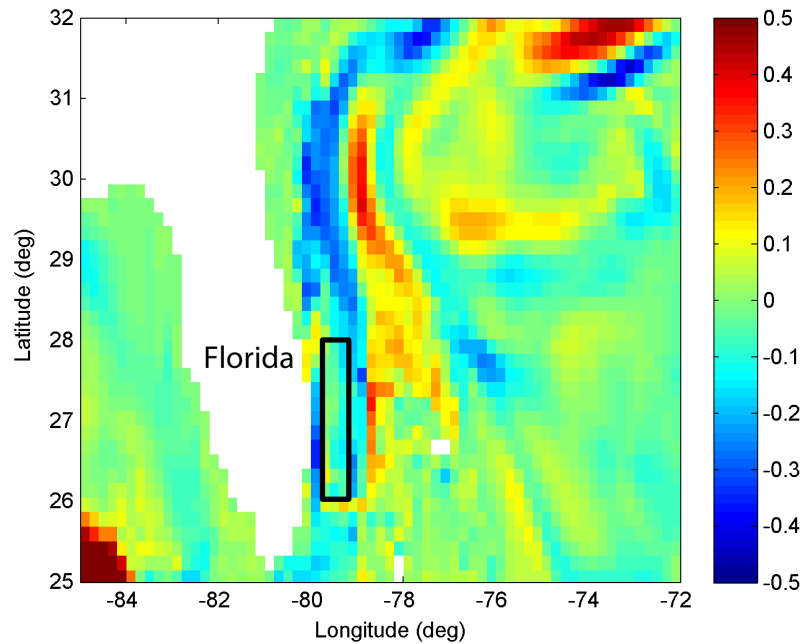


Figure 5.12: The difference of the surface mean current speed between summer (30-day average in July) and winter (30-day average in December) for case 1; black box outlines the location of turbines.

The differences in ocean current magnitude at the depth of 10 0m between undisturbed condition and two cases with energy extraction are also shown in Figures 5.13 and 5.14,

which feature very similar patterns of change, but with slightly different magnitude. Therefore, although the extra turbine drag is only added to computational cells approximately between 50-200 m, the impacts on the surface current and current at 100 m are very similar and are both prominent. Similar redirection of the Florida Current is observed at both the surface and at 100 m. Hence, the additional turbine drag applied below 50 m depth has significant influence on shallower depths all the way up to the surface.

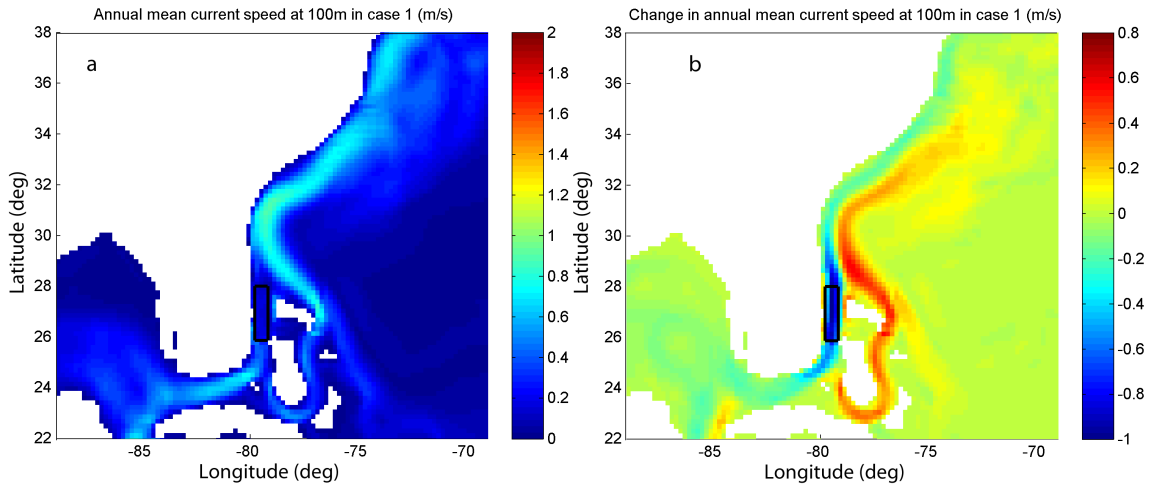


Figure 5.13: (a) Annual mean current speed at 100 m in power extraction case 1, (b) change in mean current speed at 100 m in case 1 relative to the baseline (m/s) ; black box outlines the location of turbines.

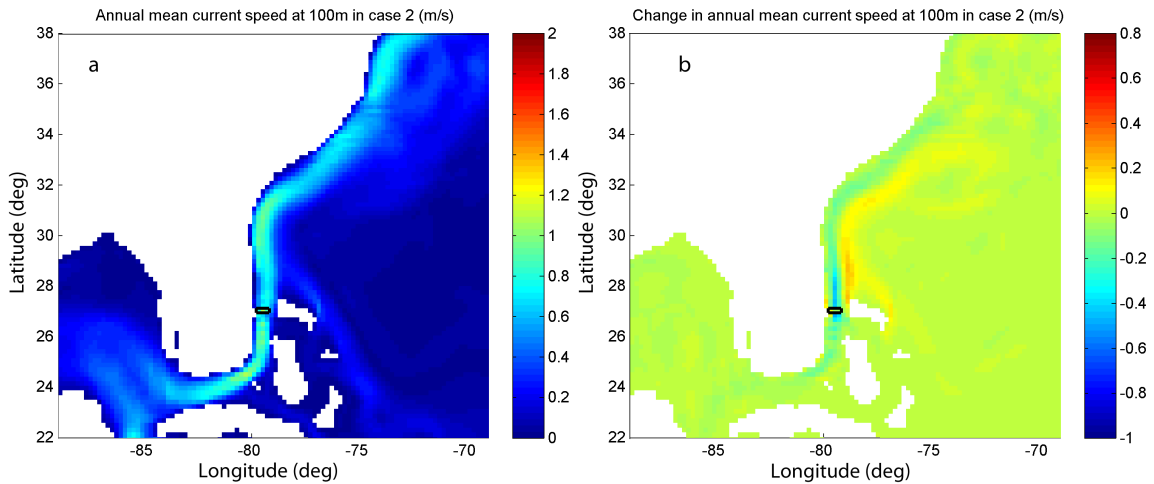


Figure 5.14: (a) Annual mean current speed at 100 m in power extraction case 2, (b) change in mean current speed at 100 m in case 2 relative to the baseline (m/s); black box outlines the location of turbines.

Figure 5.15 shows the undisturbed volume flux in the Florida Current compared with the residual volume flux in two different power extraction scenarios. In case 1, due to power extraction, the residual volume flux in the Florida Current drops from 24.7 Sv to about 11.3 Sv, a more than 54% decrease. In case 2, since the impacted area is much smaller, the reduction in volume flux is weaker accordingly, dropping from 24.7 Sv to about 22.2 Sv corresponding to approximately 10% decrease.

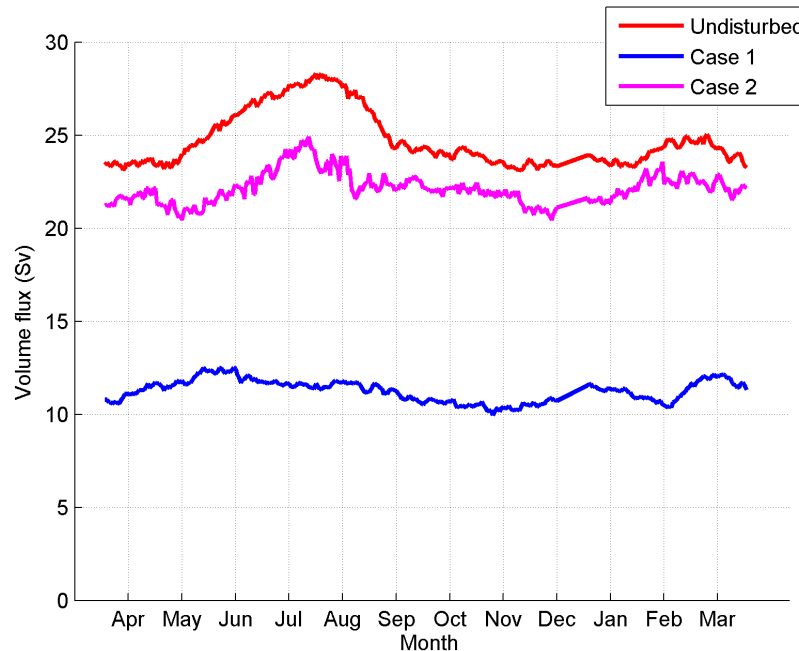


Figure 5.15: The volume flux in the Florida Current for undisturbed case (red), power extraction case 1 (blue) and power extraction case 2 (magenta).

5.4.2 Change in Sea Surface Height (SSH)

The effect of power extraction on the hydrodynamics of the flow field can also be demonstrated by the water level change. Figure 5.16 shows the SSH distribution in the undisturbed baseline case. The maps of water level difference between the undisturbed case and two cases with power extraction are shown in Figures 5.17 and 5.18. As turbine drag is added in the Florida Current in case 1, we observe a significant water level drop in the vicinity of the turbine region and the maximum water level drop is nearly 0.5 m. The analysis in the previous chapter based on an analytical 2D circulation model gives a similar prediction of

water level change in the turbine region. Furthermore, a general water level rise along the coast of the Gulf of Mexico and Florida is also seen. The greatest water level increase occurs on the west side of Florida and reaches as high as 0.2 m. Other areas of the Gulf coast feature an water level increase of approximately 0.1 m or less. The change in mean SSH due to power extraction downstream of the turbine region extends as far as Newfoundland, although the effect becomes very mild after the flow has passed Cape Hatteras.

For case 2, since power is extracted from a much smaller area of the Florida Current, the effect in terms of water level change is of similar nature but relatively weaker than in case 1. The area downstream of the turbine region with significant water level drop becomes smaller, and the maximum water level drop is approximately 0.13 m. The greatest water level rise occurs along the Florida coast upstream of the turbine region and reaches about 0.1 m, which is only half of the level in case 1. Similarly a water level rise is seen along the most of the Gulf coast, with a magnitude no greater than 0.05 m.

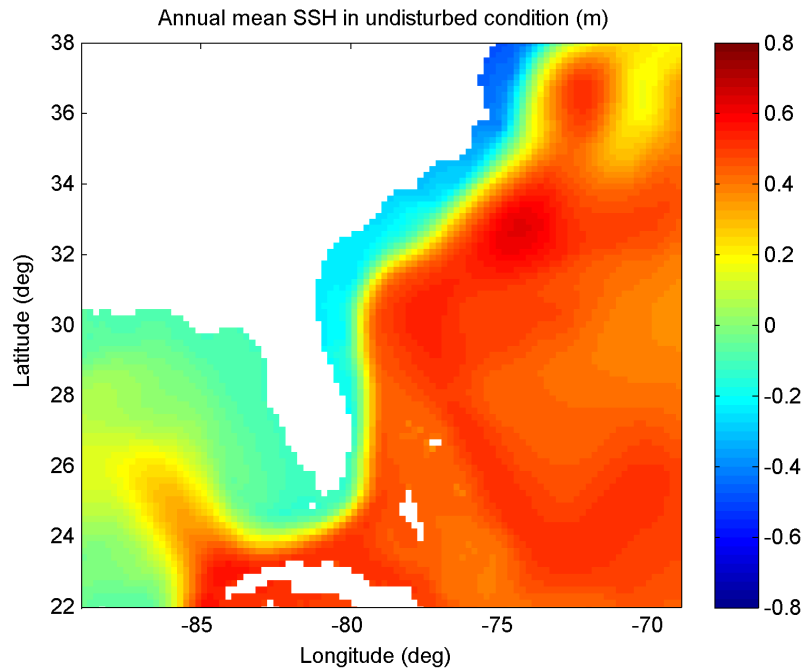


Figure 5.16: Annual mean SSH for the baseline case.

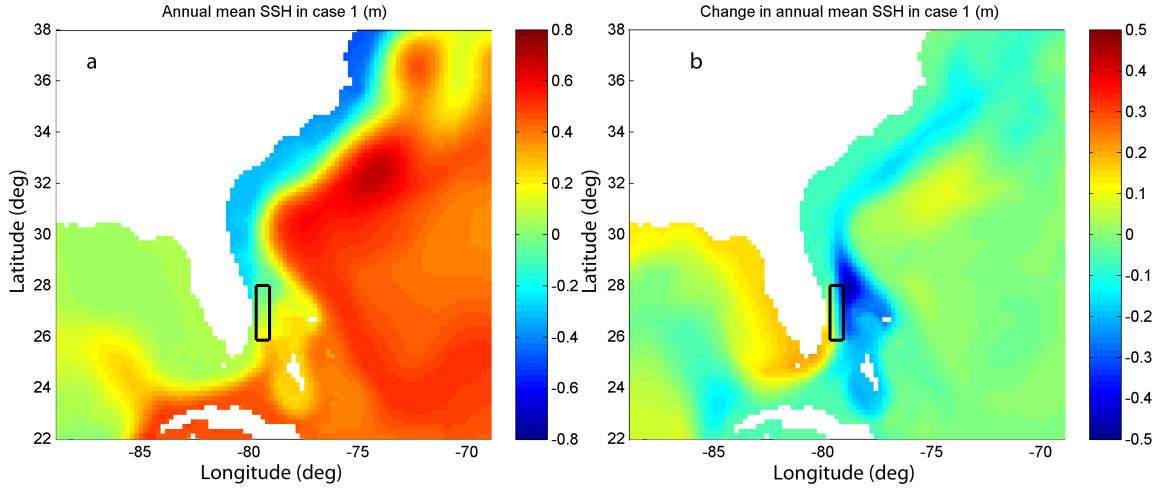


Figure 5.17: (a) Annual mean SSH in power extraction case 1, (b) change in mean SSH in case 1 relative to the baseline (m); black box outlines the location of turbines.

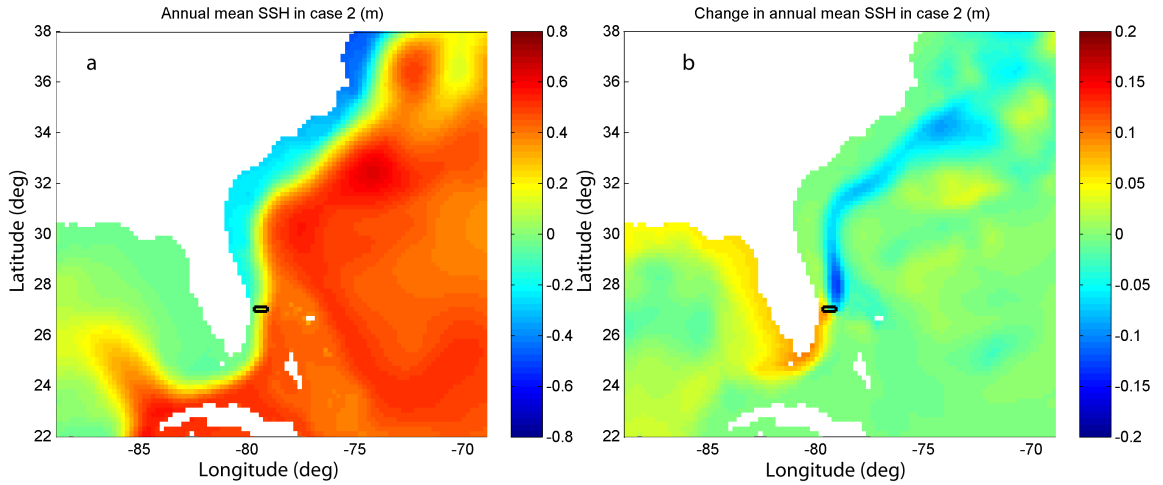


Figure 5.18: (a) Annual mean SSH in power extraction case 2, (b) change in mean SSH in case 2 relative to the baseline (m); black box outlines the location of turbines.

5.4.3 Change in Mean Power Density

With energy extraction added to the Florida Current region, the difference in mean power density between the undisturbed case and two cases with energy extraction is shown in Figures 5.19 and 5.20. Figure 5.7 already shows the power density distribution for the undisturbed condition, in which the Florida Current features a much higher power density than elsewhere. In Figure 5.19, a significant reduction in mean power density is observed in the Florida Strait, where the power extraction takes place. East offshore of the Bahamas

sees an increased power density due to the re-routing of Florida Current. The change of power density in this case is quantified in Figure 5.19b. The power density reduction due to turbines in case 1 occurs along the entire path of the Gulf Stream along the east coast. The highest mean power density drop occurs within the Florida Strait where the turbines are located, and the peak drop reaches as high as $\sim 1200 \text{ W/m}^2$, which is on the same order of magnitude as the baseline undisturbed power density at the same location. An increase in power density along the Florida east coast in the amount of about 200 W/m^2 is observed on a few computational cells west of the turbine region, indicating a current speed increase in the gap between the extraction site and the Florida coast. A slight power density drop is also observed in the far fields both upstream and downstream of the turbine region. In the upstream, a mean power density drop of about $100\text{-}200 \text{ W/m}^2$ is seen along the loop current in the Gulf of Mexico, which is a clockwise warm ocean current that feeds the Gulf Stream (Hofmann and Worley, 1986). In the downstream, the drop in mean power density occurs along the path of the Gulf Stream and extends all the way to approximately Newfoundland. The mean power density change further north is negligible. At the same time, because of the rerouting of the Florida Current, offshore of the east side of the Bahamas see a stronger current flow with power density increased by about $200\text{-}400 \text{ W/m}^2$. The newly formed flow on the east side of the Bahamas moves northward in parallel with the original Gulf Stream path and rejoins the Gulf Stream behind the power extraction site near Jacksonville, FL.

For case 2, since the region with turbines is much smaller, the power extraction from the current flow becomes weaker and its impact on the existing flow field is milder than case 1. The greatest mean power density drop occurs immediately downstream of the turbine region and reaches as high as 600 W/m^2 . Similar to case 1, an increase in mean power density slightly lower than 200 W/m^2 is observed in the computational cells located between the extraction site and the Florida coast. The rerouting of the Florida Current flow to the east of the Bahamas is less obvious in case 2 than in case 1, and a slight increase in mean power density on the order of 100 W/m^2 is observed to the east of the original Gulf Stream path. In the loop current upstream of the Florida Current, the power density drop is less prominent and is around 50 W/m^2 . Between Florida and Cape Hatteras, the original Gulf

Stream features a reduced power density between 100-400 W/m^2 due to energy extraction by turbines, while the power density of the current flow slightly east of the Gulf Stream increases by up to 100 W/m^2 . This observation can be physically interpreted as a slight eastward shift of the Gulf Stream path due to the energy extraction in the Florida Current.

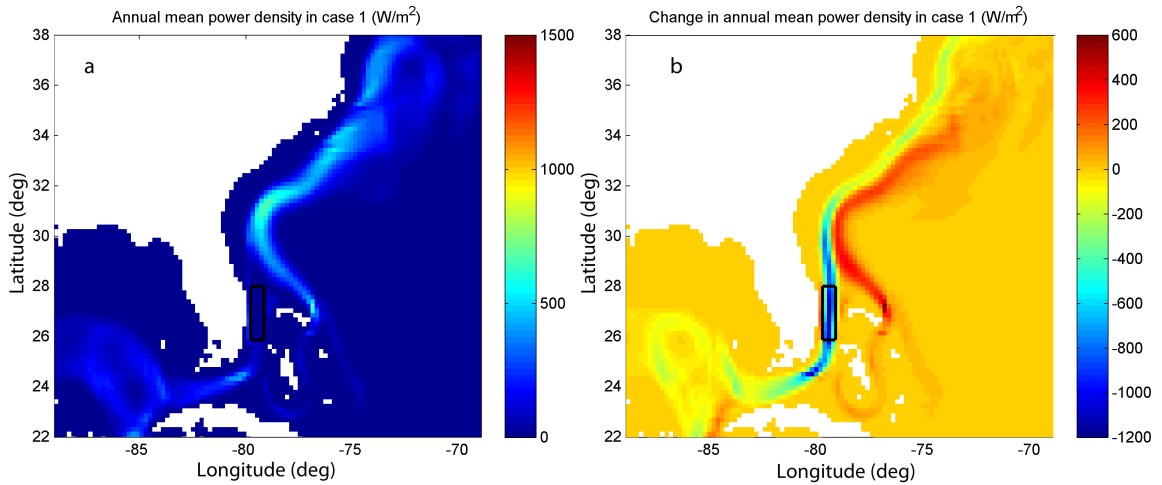


Figure 5.19: (a) Annual mean power density of the top 200 m water column in power extraction case 1, (b) change in mean power density of the top 200 m water column in case 1 relative to the baseline (W/m^2); black box outlines the location of turbines.

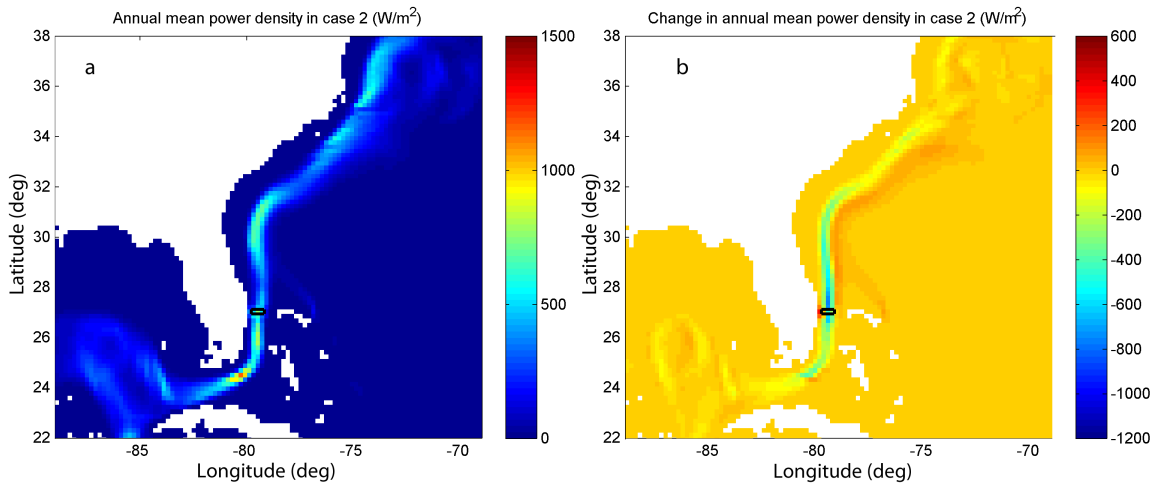


Figure 5.20: (a) Annual mean power density of the top 200 m water column in power extraction case 2, (b) change in mean power density of the top 200 m water column in case 2 relative to the baseline (W/m^2); black box outlines the location of turbines.

Figure 5.21 shows the time series of the energy dissipation from the turbines for case 1. The average power dissipation from the turbines is found to be approximately 2.4 GW,

although this number is under-predicted given that the model under-predicts the flow rate in the Florida Current. In the meantime, the residual energy flux drops by 83% to approximately 1.8 GW from the baseline level of about 11.0 GW. However, it is obvious that the energy dissipation from turbines and the residual kinetic energy flux in the channel do not add up to the original undisturbed kinetic energy flux, and the majority of the energy flux from the channelled flow has been redirected to the rerouted flow on the east of the Bahamas already shown in Figure 5.19. It is also observed that the undisturbed energy flux shows an obvious strong seasonable variability and is the strongest in summer, while the power dissipation by turbines and residual energy flux lack prominent seasonal variability of similar nature, indicating a much stronger flow reduction and redirection in summer time. Therefore, in the season when the energy flux is the strongest, the flow reduction due to power extraction is also the strongest, causing more flow to reroute to the east of the Bahamas.

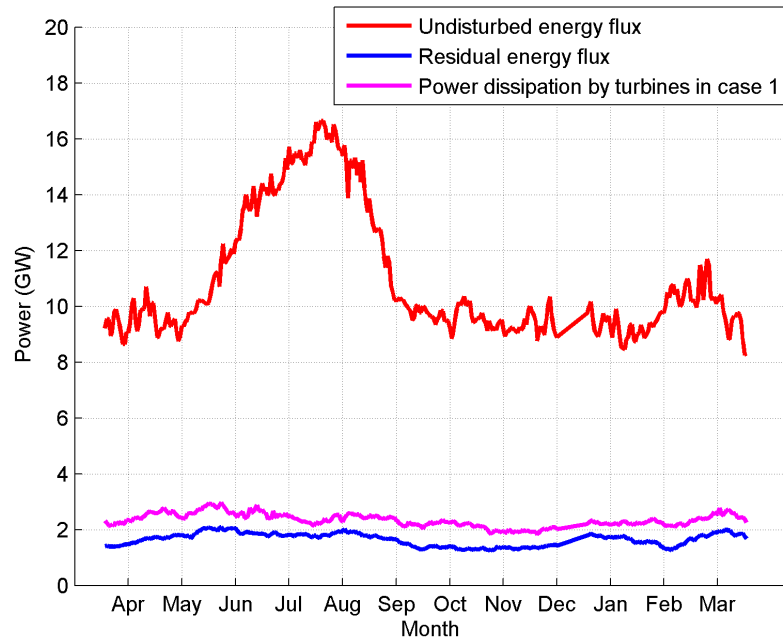


Figure 5.21: Power dissipation from turbines in case 1 together with the undisturbed and residual kinetic energy flux starting from April of the 7th year.

For the second layout of turbines covering much less space in the flow field, a smaller energy dissipation from turbines is observed and the annual average is about 0.40 GW.

Correspondingly, the residual kinetic energy flux in the Florida Strait drops by 32% from 11.0 GW to about 7.5 GW. In this case, the impact from turbines on the flow hydrodynamics in the Florida strait is definitely weaker than in case 1. However, the sum of the energy dissipation from turbines and the residual energy flux is still smaller than the undisturbed energy flux, indicating a net kinetic energy loss in the channel. Similar to case 1, due to the extra resistance created by turbines, part of the kinetic energy flux through the channel is diverted to the new route to the east of the Bahamas. From Figures 5.21 and 5.22, it is clear that the recoverable power from ocean currents in the Gulf Stream is not equivalent to the undisturbed kinetic energy flux, as some traditional methods for estimating power potential have assumed. The more energy extraction devices are placed in the flow, the more the existing flow will be blocked, and the more energy will be diverted from the existing channel to its new route, and thereby reducing the total kinetic energy reserve in the channel. This finding is fundamentally different from what was found by Defne (2010) in the study of power extraction from constrained tidal streams. In the case of extracting power by partially blocking the flow channel in tidal streams, significant flow recovery and power restoration are observed, which contribute to the sum of extracted power and the residual power exceeding the original kinetic power of flow in the baseline case. However, for the case of extracting power from the Florida Current, the sum of extracted power and the residual power is less than the original power in the baseline case due to the redirection of the flow to the east side of the Bahamas upon confronting the additional resistance from turbines.

Table 5.2 shows the effect of power extraction from all four different cases. With turbines deployed extensively in the majority of the Florida Current, both case 1 and case 3 show a substantial reduction in the flow strength with more than 50% decrease in volume flux and more than 80% decrease in energy flux. Case 3 has an extraction coefficient ($C_{ext} = 0.2$) 10 times greater than case 1 ($C_{ext} = 0.02$). However, the mean power dissipation in case 3 is barely twice as great as in case 1. In terms of effect of power extraction in case 1 and case 3, the difference gets even smaller. The maximum mean velocity drop for case 1 and case 3 are both approximately 1 m/s and the maximum mean SSH drop are both around 0.5 m, in

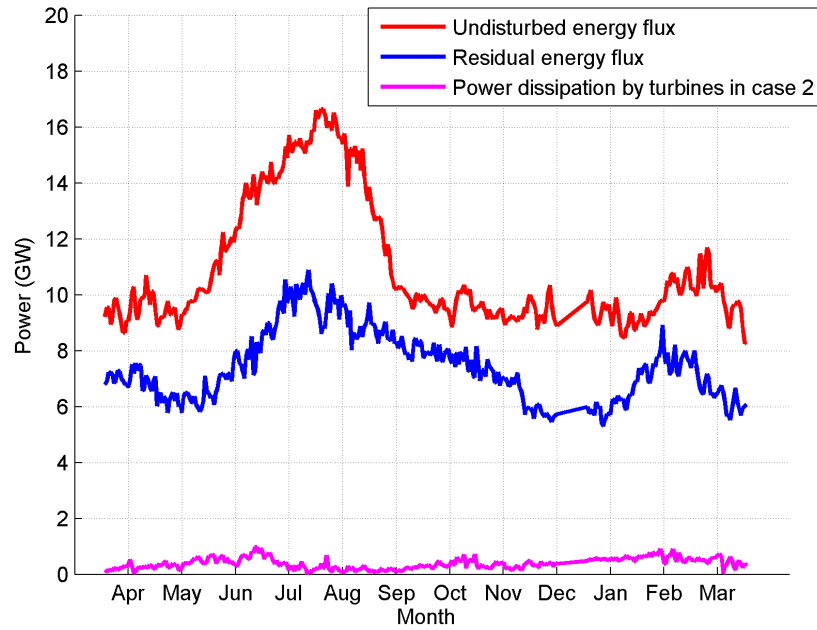


Figure 5.22: Power dissipation from turbines in case 2 together with the undisturbed and residual kinetic energy flux starting from April of the 7th year.

agreement with the findings from the analytical model in the previous chapter. Since C_{ext} can be loosely interpreted as representative of the number of turbines, the comparison shows that increasing the number of turbines by roughly tenfold would not increase the power dissipation from turbines correspondingly. In case 2 and 4 in which turbines are deployed according to the second layout scheme, similarly increasing the extraction coefficient by tenfold increases the power dissipation by less than threefold. Therefore, it is indicated that as more turbines are added to the flow channel, the power dissipation from each turbine is reduced and so is the efficiency of each individual turbine.

Table 5.2: Summary of the effects of power extraction for four different cases.

Cases	Mean power (GW)	Mean vol. flux drop (Sv)	Mean energy flux drop (GW)	Max. mean power density drop (W/m ²)	Max. mean vel. drop (m/s)	Max. mean SSH drop (m)
case 1	2.4	13.4(54%)	9.2(83%)	~1200(80%)	1.0(83%)	0.48(107%)
case 2	0.4	2.5(10%)	3.5(32%)	~800(53%)	0.6(50%)	0.13(59%)
case 3	3.8	16.5(67%)	9.7(88%)	~1300(87%)	1.1(92%)	0.54(120%)
case 4	0.06	1.1(4%)	2.3(21%)	~480(32%)	0.3(25%)	0.05(11%)

5.4.4 Temporal Effects of Power Extraction

Besides the changes in mean ocean state, it is also beneficial to examine the changes of flow field in the temporal domain. Therefore, 5 locations (shown in Figure 5.23) representative of the turbine region, upstream and downstream of the power extraction site are selected and detailed time series of change in velocities and SSH are analyzed.

Location A is selected within the area of the extraction site where turbines are deployed, and therefore has the most direct impact from power extraction and also the greatest current speed drop. Location B is selected slightly downstream of the extraction site where the rerouted path of the Florida Current flow passes through, so the characteristics of the re-directed flow can be analyzed. Previous discussions already show a substantial mean current speed increase at location B. Location C is selected on the west coast of Florida. Location D is selected downstream of the Gulf Stream near Cape Hatteras and location E is selected upstream of the Florida Current so the effects of power extraction on both upstream and downstream can be examined in greater detail.

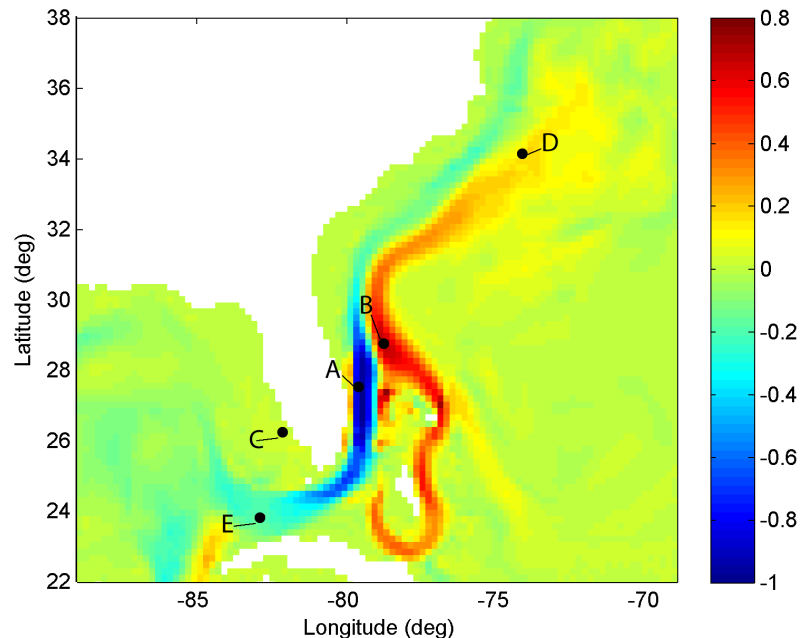


Figure 5.23: Locations of the 5 selected points shown in the annual mean surface current speed map (m/s).

At location A which is located in the Florida Strait, the undisturbed flow is primarily northward directed due to the geographical constraint imposed by the Florida coast and the Bahamas. Therefore the v (northward) velocity component plays a dominant role in the undisturbed condition while the u (eastward) velocity component is much weaker and nearly zero at this location. As power extraction from case 1 is implemented, it practically adds an obstacle in the flow path within the Florida Strait, and therefore forces the flow to redirect to the east. The flow is redirected to bypass the high resistance region by changing flow direction, and therefore the northward flow velocity component is significantly reduced while the eastward component increases. The u velocity component slightly increases from nearly zero to approximately 0.2 m/s, while the v velocity component drops from approximately 1.4 m/s to 0.2 m/s (Figure 5.24). A significant water level drop up to 0.2 m is seen at this location. The SSH drop results from the change of the local momentum balance due to the additional drag force from turbines, which in turn changes the local pressure gradients. The change in pressure gradient is reflected as water surface change.

At location B, modification of the flow pattern from the power extraction is also clearly noticeable on both velocity change and water level change (Figure 5.25). Location B is located at the spot where the rerouted Florida Current from the east of the Bahamas merges back with the original Florida Current flow, therefore a significant increase in u velocity component directed westward is observed. Meanwhile, the redirection of the Florida Current flow also contributes to a stronger northward current velocity at location B and the increase of magnitude is up to 0.8 m/s. Similar to location A, a significant water level drop as great as 0.5 m is also seen at location B. This estimate is in agreement with the estimate from the previous chapter.

At location C, which is on the west coast of the Florida, the baseline current speed is much lower than in the Florida Strait. The impact from power extraction is fairly mild as well compared to locations A and B. The u velocity slightly increases from nearly zero to about 0.02 m/s on average directed westward, and the v velocity goes up by about 0.02 m/s from nearly zero on average and is directed northward. Therefore, the power extraction in the Florida Current causes the flow at location C to gain a net northwest-ward momentum.

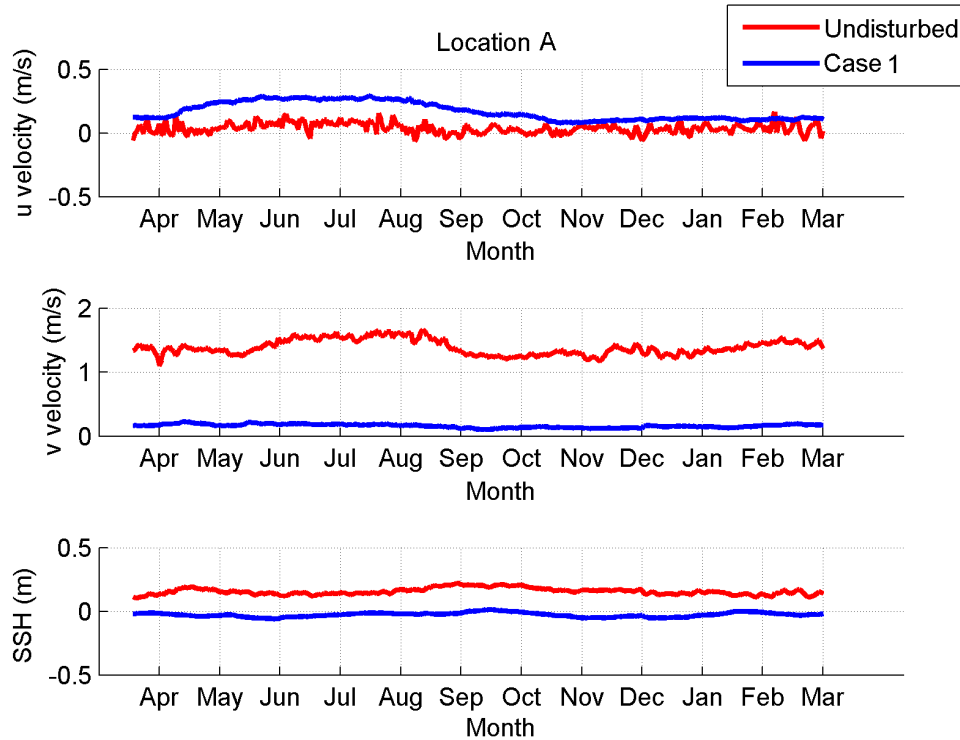


Figure 5.24: Current velocities and SSH at location A (79.6W, 27.5N) for undisturbed flow and for case 1 with positive u velocity being eastward and positive v velocity northward.

This additional momentum constitutes a small portion of the momentum flux that has been diverted from the Florida Current due to the extra resistance by turbines, of which the majority goes to the east side of the Bahamas. At the same time, a substantial water level rise of approximately 0.2 m is observed at this location.

At location D, which is downstream of the power extraction site, very little impact from the power extraction is felt by the mean flow field. The mean values of both u and v velocity components stay almost constant, although mild fluctuations are seen in the time series. However, at some times, differences of relatively great magnitude are observed in both velocity and SSH changes. For example, at about day 150, a relatively significant difference in v velocity time series between the baseline and the case with power extraction is observed. A significant difference in SSH is also observed at a later time (around day 250). These differences result from the propagation of eddies formed by the perturbation caused by power extraction. The main flow in the Florida Current is separated at the

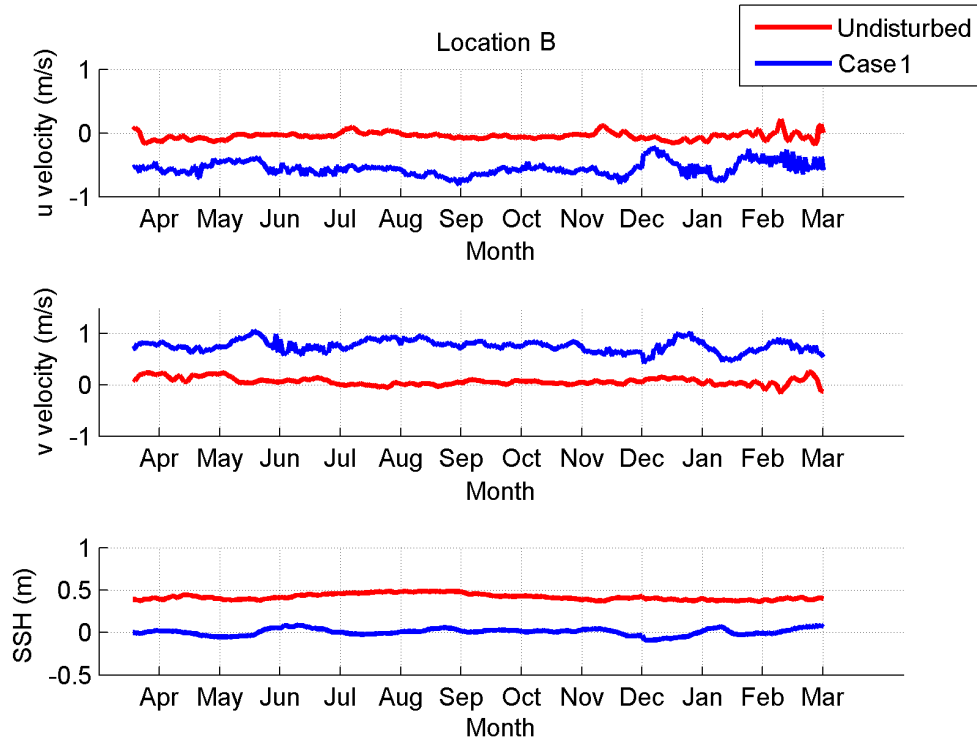


Figure 5.25: Current velocities and SSH at location B (78.8W, 28.7N) for undisturbed flow and for case 1 with positive u velocity being eastward and positive v velocity northward.

power extraction site because of the obstacle created by the additional turbine drag. As the separated flows merge behind the obstacle (i.e. the turbine array) creating eddies, the eddies develop and propagate downstream along the path of the Gulf Stream and contribute to the intermittent differences in velocities and SSH. Impacts from eddies on velocities and SSH are out of phase because the timings of the influence from eddies are different on velocity and SSH fields. A significant change in velocity usually occurs on the edge of an eddy passing through while a significant change in SSH usually occurs when the center of an eddy passes through. Therefore the time of a significant SSH change lags the time of a significant velocity change as shown in Figure 5.27, and the time lag depends on the size and propagating speed of the eddies. Figure 5.28 shows the change in flow field at two different snapshots day 155 and day 250, corresponding to the two prominent differences in velocity and in SSH shown in Figure 5.27. On day 155, a strong current velocity increase is observed at location D, and this happens when the edge of an eddy passes by. On day

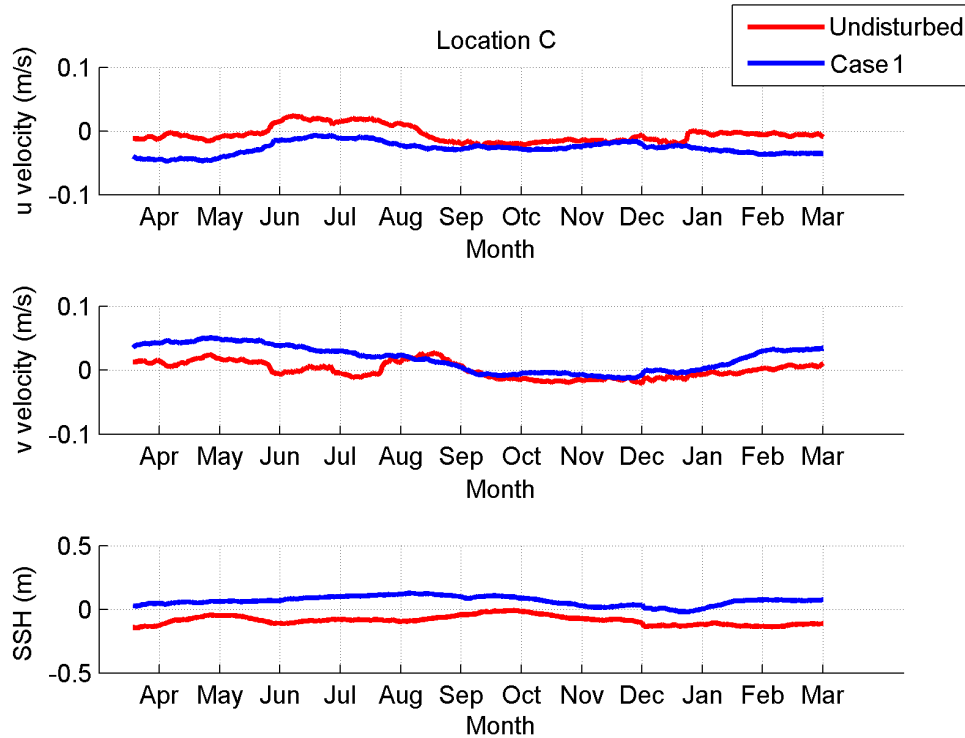


Figure 5.26: Current velocities and SSH at location C (82.2W, 26.4N) for undisturbed flow and for case 1 with positive u velocity being eastward and positive v velocity northward.

250, an significant SSH drop is observed at the same location but the current speed barely changes. This is because that location is situated at the center of an eddy on that day.

At location E, which is upstream of the power extraction site, the primary velocity component is the eastward u component as the current flows eastward to enter the Florida Strait, while the northward v velocity component is weaker. The impact from power extraction on this area is relatively mild compared to locations A and B, since location E is located at the shared upstream of both the original Florida Current and the rerouted flow around the Bahamas. The flow has to pass through location E whether or not there is power extraction in Florida Current. Therefore, the average v velocity component has negligible change, as is the water level difference in this area. Only a slight drop from about approximately 0.9 m/s to 0.8 m/s in annual mean u velocity component is observed.

For case 2 in which the power extraction is simulated in a much smaller area, the same 5 locations are selected as in case 1 and the time series of current velocity components

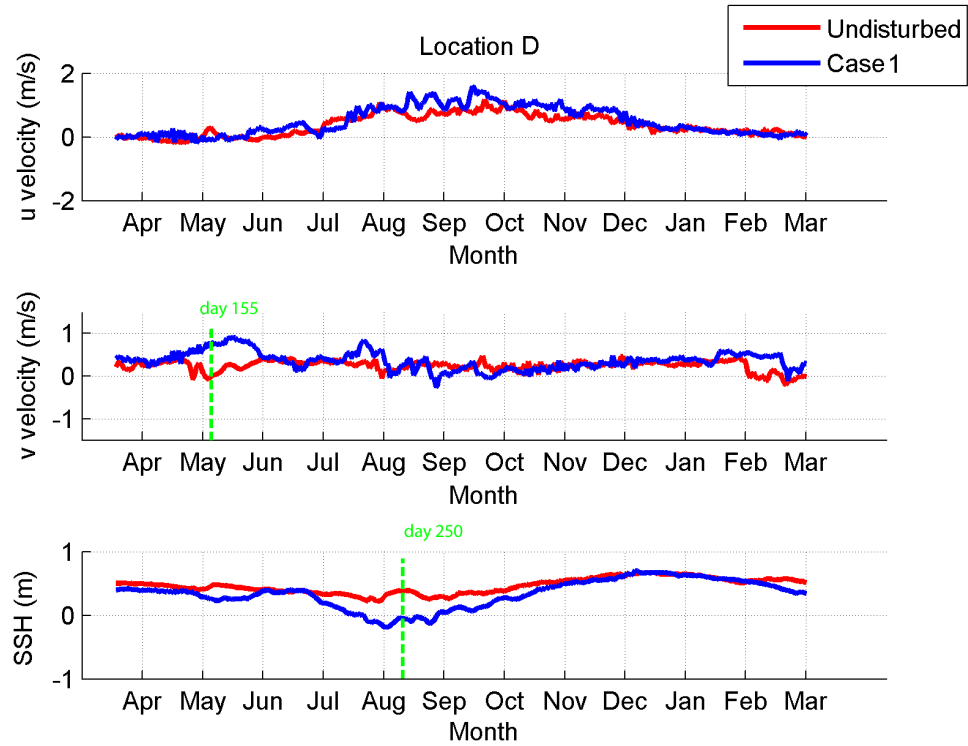


Figure 5.27: Current velocities and SSH at location D (74.2W, 34.2N) for undisturbed flow and for case 1 with positive u velocity being eastward and positive v velocity northward.

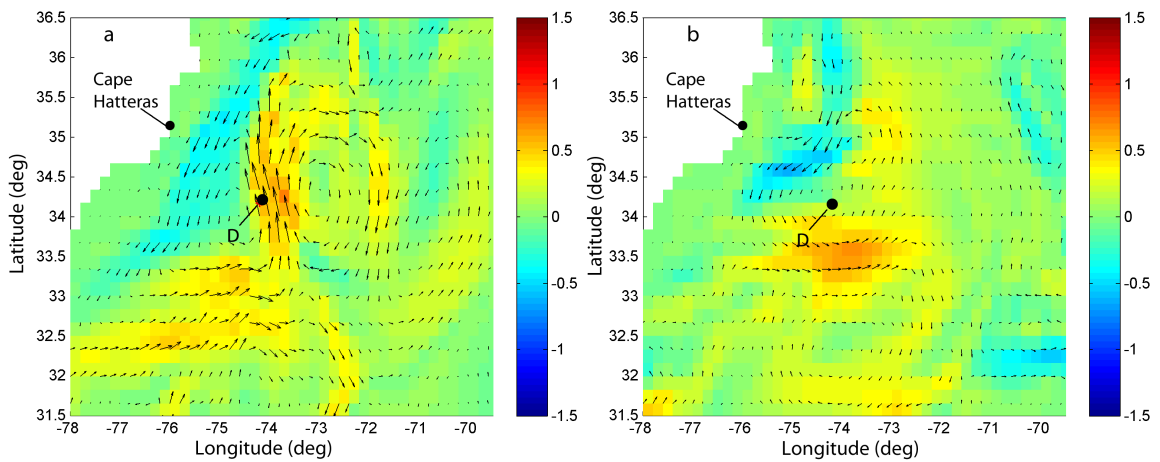


Figure 5.28: Flow field change in case 1 relative to the baseline case on day 155 (a) and day 250 (b) for location D.

and SSH are examined to gain a better understanding of the effect of power extraction at a smaller scale. At location A, the power extraction essentially adds a local obstacle in the Florida Strait channel. However, since the impact area of the additional drag force

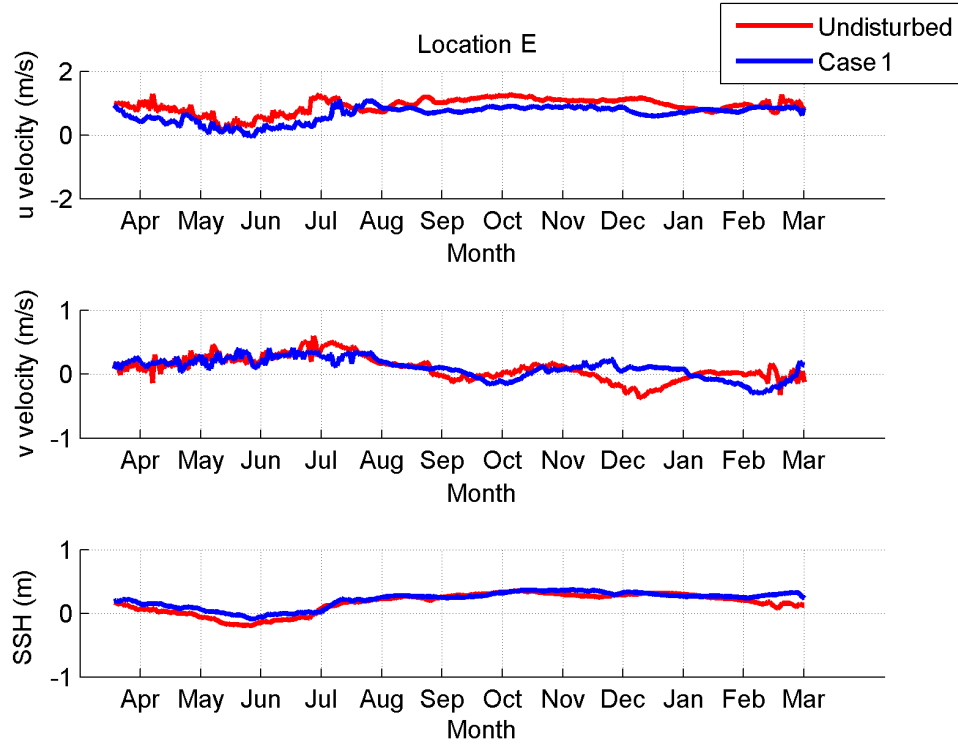


Figure 5.29: Current velocities and SSH at location E (82.8W, 23.9N) for undisturbed flow and for case 1 with positive u velocity being eastward and positive v velocity northward.

from turbines is much smaller than in case 1, a fully developed flow re-direction around the Bahamas as in case 1 is not seen. The power extraction in this case has a very minor impact on the u velocity component at this location, while its impact on the v velocity component is more substantial, with a drop on the order of 0.6 m/s. A less significant but noticeable drop on the order of 0.1 m in the SSH is also seen at this location.

At location B, the impact from turbines on velocities is less noticeable than in case 1 due to weaker strength of power extraction. The change in u velocity component is negligible, and the change in v velocity component is less than 0.2 m/s on average. The change in SSH at this location is also less significant than in case 1, with a 0.2 m SSH drop on average.

At location C located on the west coast of Florida, the effect of turbines in both velocities and SSH is very similar as in case 1 in nature, but weaker in magnitude. The changes in both u and v velocity components are less than 0.01 m/s on average, and the change in SSH is smaller than 0.1 m. Therefore in this case, the hydrodynamic impact in the upstream of

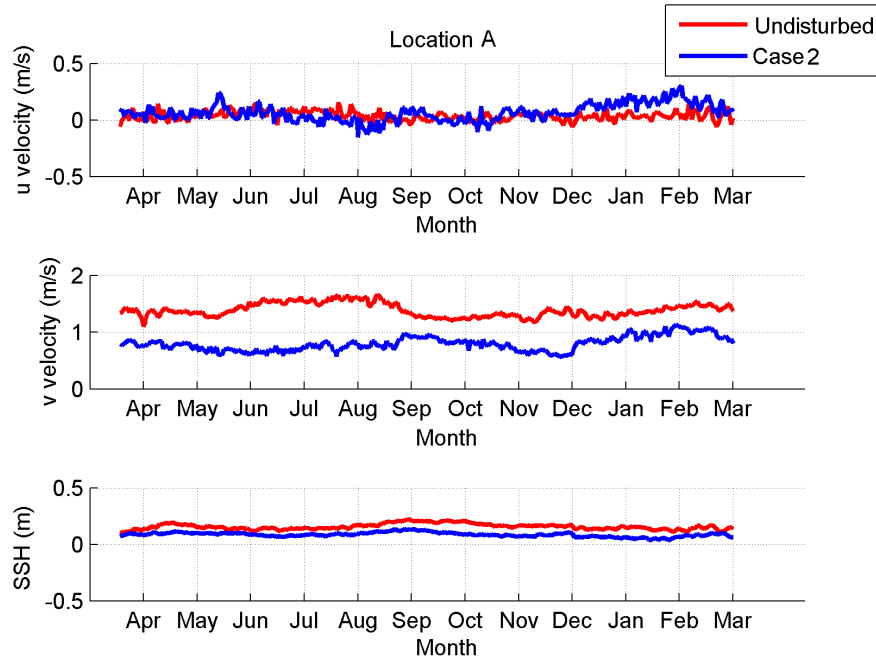


Figure 5.30: Current velocities and SSH at location A (79.6W, 27.5N) for undisturbed flow and for case 2 with positive u velocity being eastward and positive v velocity northward.

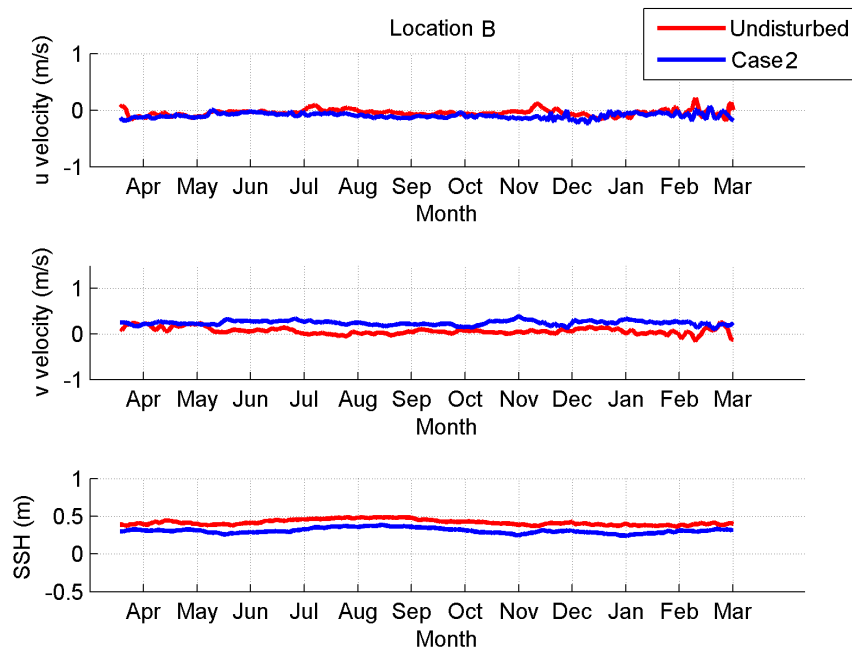


Figure 5.31: Current velocities and SSH at location B (78.8W, 28.7N) for undisturbed flow and for case 2 with positive u velocity being eastward and positive v velocity northward.

the extraction site on the west coast of Florida is too weak to pose any noticeable influence.

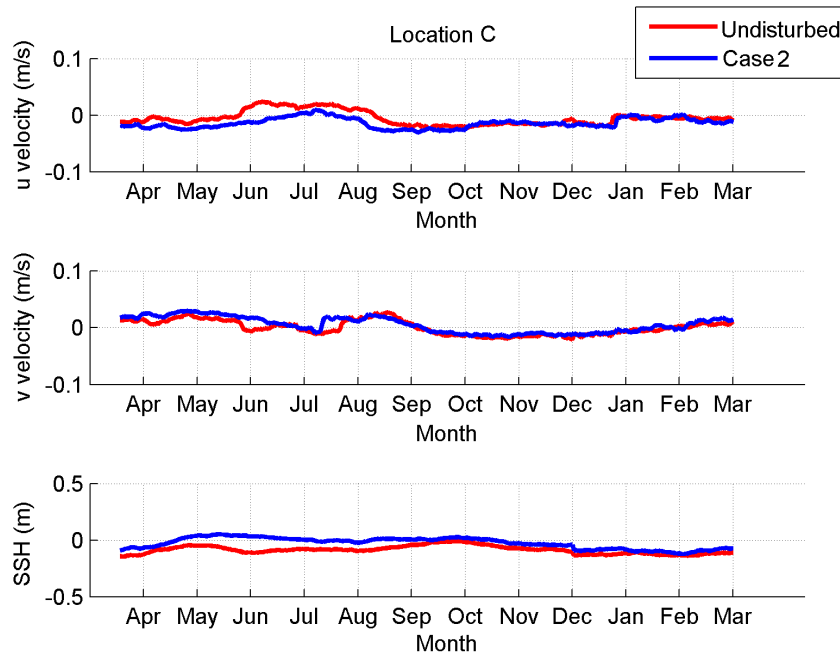


Figure 5.32: Current velocities and SSH at location C (82.8W, 26.4N) for undisturbed flow and for case 2 with positive u velocity being eastward and positive v velocity northward.

At location D located in the downstream of the extraction site, similar to in case 1, very little impact from turbines is felt by the flow field. The change in the mean u and v velocity components is negligible. However, some instantaneous changes in snapshots at certain times can be noticed, and they can also be attributed to the propagation of eddies formed downstream of the power extraction site. At location E located in the upstream of the extraction site, the impact from power extraction on both velocity components and the SSH is barely noticeable, indicating negligible effects on this area.

Although the impact from power extraction on the annual mean flow field is mostly located in the near field of the power extraction site (Figure 5.35a), the time varying effect can reach much farther upstream and downstream (e.g. Figure 5.35b). Figure 5.36 shows the time series of the change in velocity and SSH for location F, which is at the offshore of French Guiana. The impact from power extraction in the Florida Current on this region mainly appears in the form of eddies, and the primary effect is the delay of the timing for

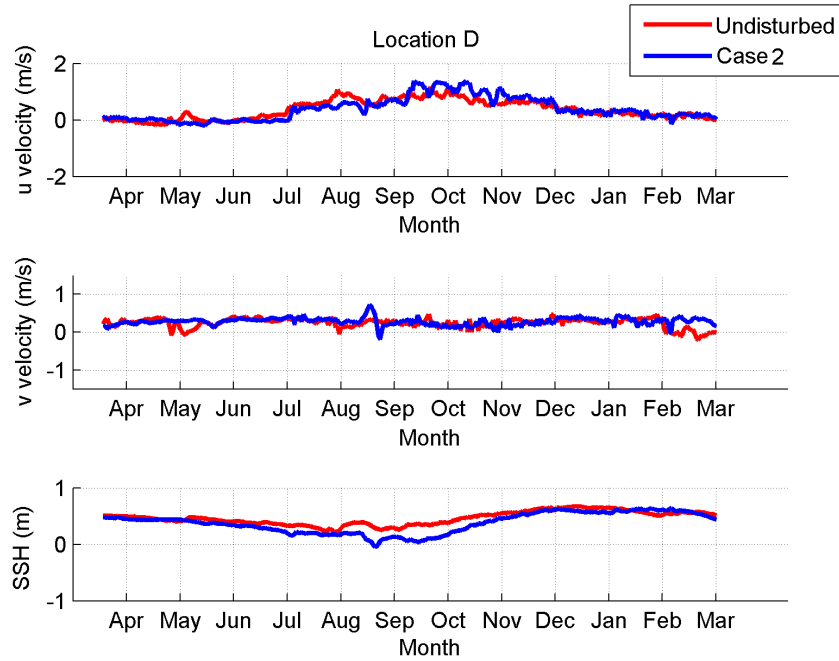


Figure 5.33: Current velocities and SSH at location D (74.2W, 34.2N) for undisturbed flow and for case 1 with positive u velocity being eastward and positive v velocity northward.

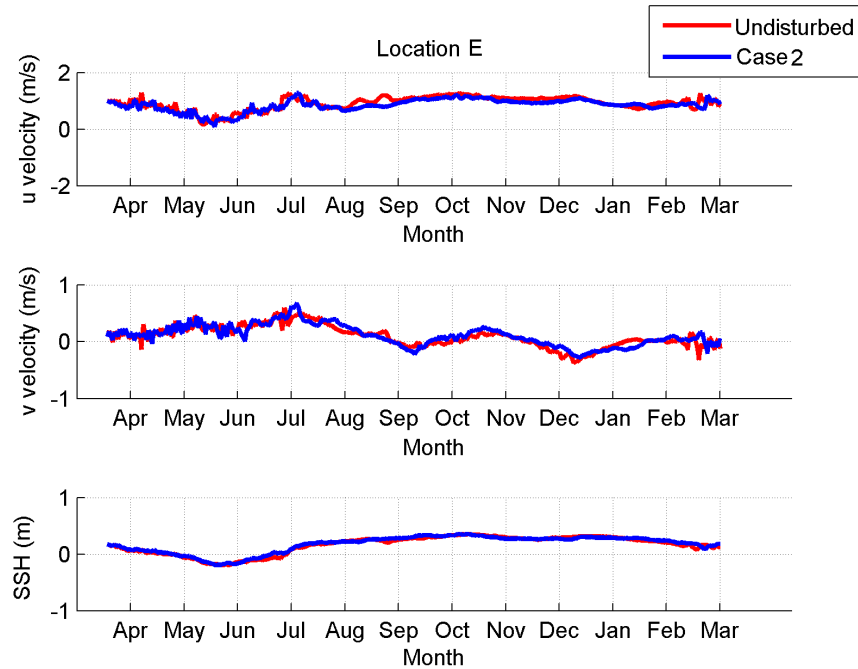


Figure 5.34: Current velocities and SSH at location E (82.8W, 23.9N) for undisturbed flow and for case 2 with positive u velocity being eastward and positive v velocity northward.

eddies to arrive at the same location while there is little change to the mean flow field in this area.

This feature can also be observed by examining the change of variance of the surface current speed due to power extraction. Figure 5.37 shows the variance of surface current speed for both the baseline case and for the power extraction case 1 calculated based on one year of time series data. Figure 5.38 shows the difference of variance of surface current speed resulted from power extraction in case 1. It is seen that although power extraction has a significant effect on the instantaneous flow field in the far field from the power extraction site, especially in the far upstream, the change in the statistical nature of the flow field is fairly minor.

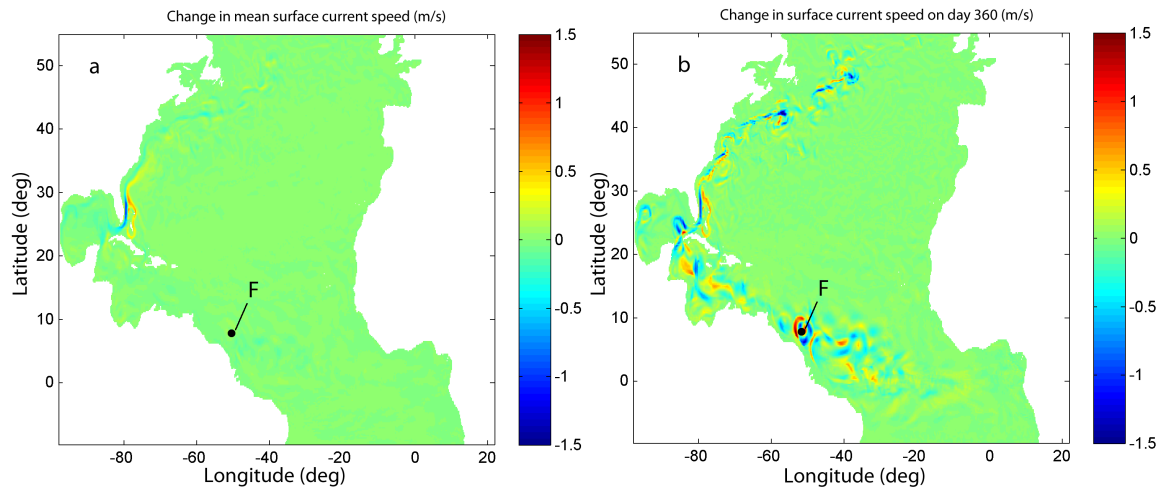


Figure 5.35: Changes in (a) annual mean surface current speed and (b) instantaneous surface current speed at day 360 for case 1.

5.5 Summary

A full numerical simulation using HYCOM was described in this chapter to model the power extraction from the Florida Current in two different turbine layouts. The primary purpose is to evaluate the effects of power extraction on the flow field. For the first turbine layout, the turbine region covers the majority of the surface area of the Florida Current and is dedicated to studying the extreme possible effect of power extraction on the flow hydrodynamics. It is found that power extraction under this turbine layout in the Florida

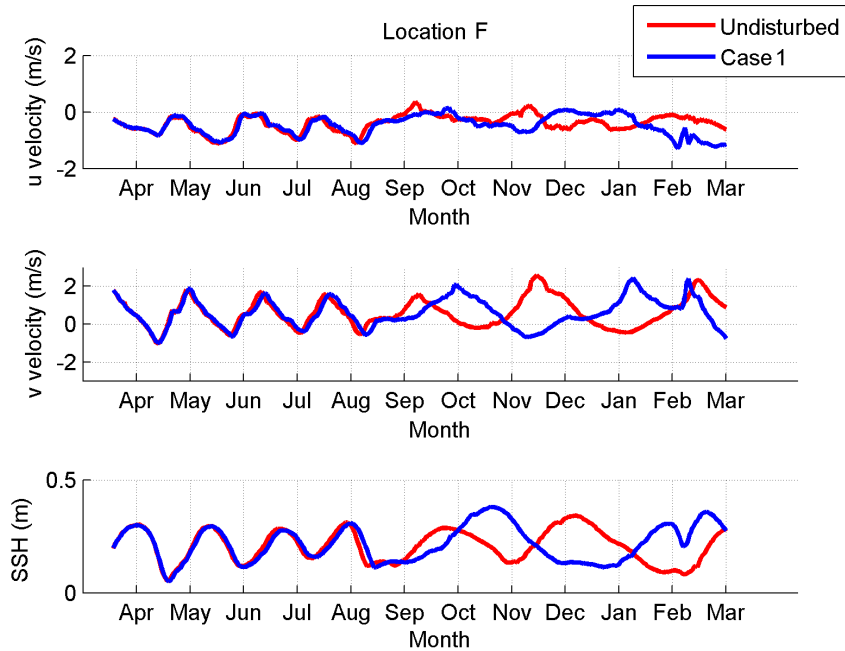


Figure 5.36: Current velocities and SSH at location F (51.6W, 7.6N) for undisturbed flow and for case 1 with positive u velocity being eastward and positive v velocity northward.

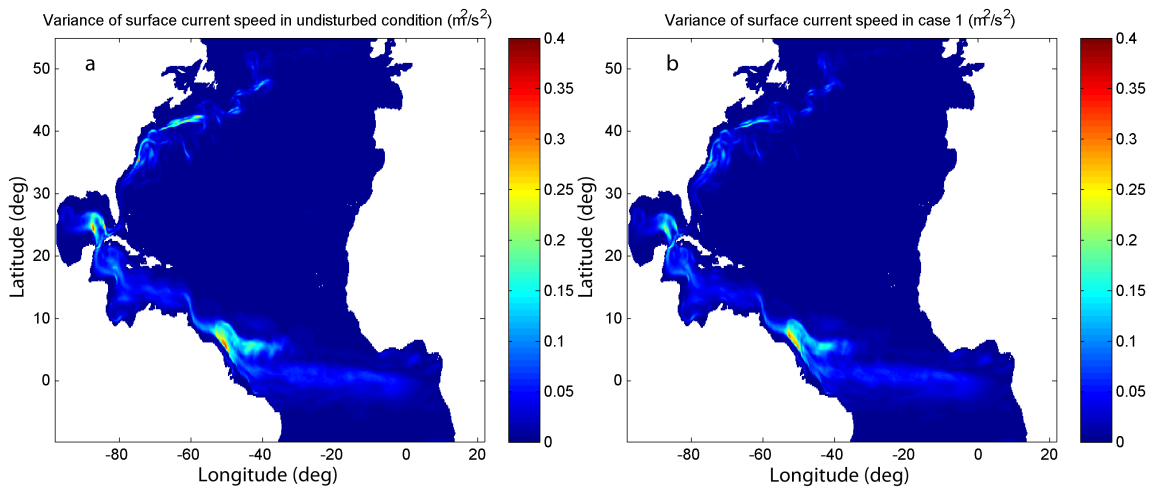


Figure 5.37: Variance of surface current speed for the undisturbed condition case (a) and case 1 (b).

Current can cause significant flow reduction in the Florida Current, with the annual mean surface current speed dropping by up to about 1m/s and the annual mean power density decreasing by more than 1000 W/m². In such scenarios, the volume flux in the Florida Current can be reduced by more than 50% and the kinetic energy flux can drop by more

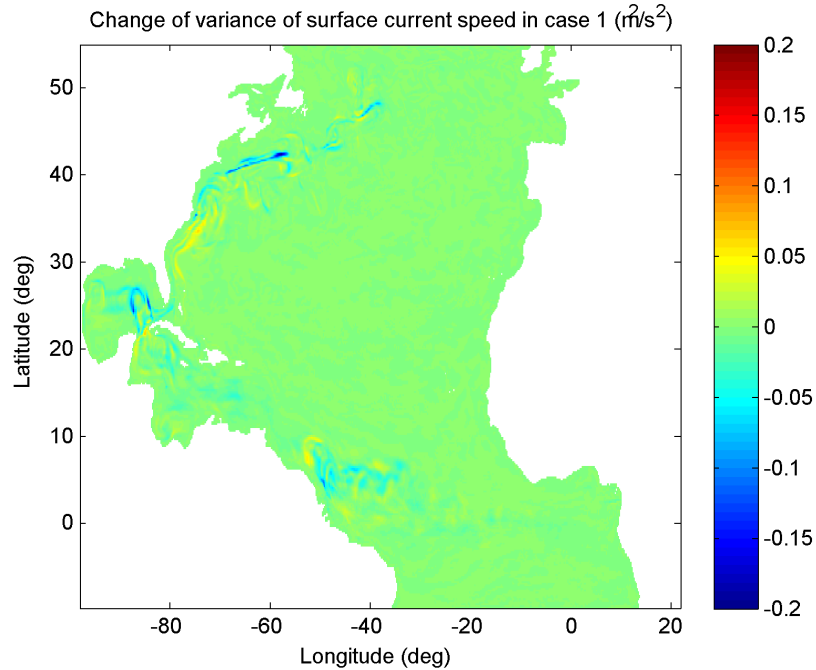


Figure 5.38: Change of variance of surface current speed in case 1.

than 80%. The power extraction can also cause a significant water level drop on the order of 0.5 m in the near field. At the same time, the flow on the east side of the Bahamas strengthens as the original Florida Current flow is redirected further offshore to avoid the increased resistance in the Florida Strait channel. This explains the original energy flux from the baseline case exceeding the sum of the extracted power and the residual energy flux in the Florida Current. For more realistic scenarios in which turbines occupy a much smaller region, the power extraction is also lower. The area immediately downstream of the turbine region feels the most significant impact of a mean surface current speed dropping by about 0.5 m. With the power extraction in this scenario, the residual energy flux in the Florida Current drops by about 20-30%, and the extraction power and the residual energy flux still do not add up to the original power in the baseline case, indicating a net loss of energy reserve in the Florida Current. The flow reduction in the Florida Current also features an obvious seasonal variability, stronger in summer and weaker in other seasons, therefore the power extraction reduces the seasonable variability of the residual fluxes through the Florida Current by causing stronger flow reduction in summer and weaker flow reduction

in winter. The results from this numerical simulation agree well with the results of the analytical model from the previous chapter in terms of current velocity and water level changes due to power extraction. In addition, the simulation predicts a slight water level rise along the Florida and Gulf coasts. Although the effect of power extraction on the mean flow field is primarily felt in the near field of the turbine region site, the time varying effect can reach much farther upstream and downstream. In the far upstream regions, the power extraction has little impact on the mean flow field, but acts to change the timing of the propagation of eddies. In the downstream, eddies created by power extraction develops and propagates downstream to cause intermittent change to both velocity and SSH fields. However, the power extraction in the Florida Current has negligible effect on the overall statistics of the far flow field.

CHAPTER VI

CONCLUSIONS

Increasing energy consumption and decreasing reserves of fossil fuels have resulted in growing interest in alternative renewable energy from the ocean. Ocean currents are an attractive source of clean energy due to their inherent reliability, persistence and sustainability. For the United States, the Gulf Stream system is of particular interest due to its particularly high current speed and its proximity to a large population on the U.S. east coast. In this dissertation, the ocean current characteristics along the U.S. coastline were described from a probabilistic perspective. Ocean current energy potential from the highly energetic Gulf Stream system was estimated using different approaches, and the effects of possible power extraction from the Gulf Stream system were also examined. This study advances awareness and understanding in ocean current energy resource assessment with emphasis on the Gulf Stream system, and provides a preliminary estimate of the prospect for development of power conversion projects.

The ocean currents along the U.S. coastline were characterized by using ocean model data collected from various sources. For regions with multiple data sources available, the optimal data source was selected based on the statistical agreement between the model data and ocean observational data. Selected ocean model data were used to develop a database that maps the ocean current energy resource distribution for the entire U.S. coastline, and also provides joint velocity magnitude and direction probability histograms for offshore areas within about 200 miles of the U.S. coast. The database is accessible from <http://www.oceancurrentpower.gatech.edu>.

The resource characterization particularly focuses on the Gulf Stream system, and mean volume transport calculated from both HYCOM Global 1/12 deg Analysis and HYCOM Gulf of Mexico 1/25 deg Analysis dataset (<http://hycom.org/>) are compared with volume flux measured by submarine cables. HYCOM GoM data were shown to predict the mean

volume flux in the Florida Current fairly accurately with a high statistical agreement ($R^2 = 0.77$) while the HYCOM Global results under-predicts the volume flux by about 15%. The mean vertical velocity profile from HYCOM GoM output also agrees well with 1-year ADCP measurements in the Florida Current. Therefore HYCOM GoM results were selected for characterizing the Florida Current. The Florida Current is found to have the highest mean surface power density exceeding 2500 W/m^2 , while most of the of U.S. offshore has a mean surface power density lower than 100 W/m^2 . The majority of the kinetic energy in the Florida Current is found to be concentrated in the upper 200 m of the water column. The Florida Current is fairly stable due to the geographical constraints of Florida and the Bahamas. However, the Florida Current still features obvious seasonable variation with the current flow being the strongest in summer time. Strong seasonable variability is prevalent in the upper layer of the water column (approximately upper 100 m), while the variation in deeper water is more negligible, indicating that the seasonable variability results from surface momentum flux such as surface wind stress. The core of the Florida Current has higher stability than the edge as a direct result of the meandering and seasonal broadening of the current flow. As the Gulf Stream flows downstream past Cape Hatteras into the open ocean, the variability greatly increases.

The potential extractable energy from ocean currents is not equivalent to the integrated undisturbed ocean current power density. The estimate of energy potential based on undisturbed power density is only meaningful when the number of conversion devices and the cumulative effects on the existing flow are small. When a large amount of energy is extracted, the flow velocity will be significantly reduced and larger number of devices will be needed to extract the same amount of power. Therefore, a 2-D ocean model considering the physical mechanism of the formation of the circulation is utilized in this study to estimate the power potential from ocean currents in the Gulf Stream. Firstly, the theoretical momentum balance in the Gulf Stream system is examined using the two-dimensional ocean circulation equations based on the assumptions of the Stommel model for subtropical gyres with quasi-geostrophic balance between pressure gradient, Coriolis force, wind stress and friction. Parameters including water depth, natural dissipation rate and wind stress are

adjusted in the model to reproduce reasonable flow properties including volume and energy flux in the western boundary current that represents the Gulf Stream system. To represent flow dissipation from turbines, additional turbine drag coefficient is formulated and included in the model.

The analysis showed that considering extraction over a region comprised of only the Florida Current portion of the Gulf Stream system, the theoretical upper bound of average power dissipated ranges between approximately 4 and 6 GW with a mean around 5.1 GW. This corresponds to an average of approximately 45 TWh/yr. However if the extraction area comprises the entire portion of the Gulf Stream within about 200 miles of the US coastline from Florida to North Carolina, the theoretical upper bound of average power dissipated becomes approximately 18.6 GW or 163 TWh/yr. As defined by the National Research Council, the theoretical resource is the amount of power contained in the natural system, and the values provided here can be regarded as the theoretical resources. However, the technically recoverable resource is defined as the resource extraction realizable within the limitations of presently available devices and site-specific resource intensities, and should be significantly below the theoretical estimate provided here. Such limitations include wake loss, turbine and transmission efficiencies, and other engineering and technological constraints. The extract percentage of the theoretical resource that can be converted into electricity considering turbine related efficiencies needs more research to be determined. Since the two-dimensional model is an idealized representation of the actual North Atlantic circulation with assumptions for mathematical convenience, the results need to be treated as an order-of-magnitude estimate with uncertainty due to model simplification. In addition, the estimate is regarded as theoretical energy resource, and the practical resource will only be a fraction of the theoretical resource. Since the technology for ocean current power is not fully developed yet, it is impossible to quantify the uncertainty from technological constraints. However providing an estimate by assuming a 30% power conversion efficiency for energy removal from the flow to electrical power yields the peak potential for electricity production of approximately 1.5 GW on average from the Florida Current and 5.6 GW from the entire U.S. portion of the Gulf Stream system, or 13 and 49 TWh/yr, respectively.

The two-dimensional steady ocean circulation model shows a strong impact from the additional turbine drag in the Gulf Stream on the neighboring area of the power extraction. However, its impact on the far field is less. The presence of turbines creates an artificial obstacle in the flow path, and reduces the northward velocity component of ocean currents in the vicinity of the turbines. The additional turbine drag also modifies the eastward velocity component in the turbine region, primarily changing its direction resulting in redirection of the Gulf Stream flow. The net result is reduced flow in the turbine area while the bulk current flow shifts further offshore to the east to avoid the region of high resistance. The presence of turbines also has a significant impact on the local momentum and energy balance. The turbines also cause a significant water level drop in the turbine region due to modification of the local pressure gradient. In the case in which approximately 5.1 GW of power is dissipated from turbines in an area similar to the Florida Current, a current speed drop of up to 1 m/s is observed in the power extraction site. In addition, the sea surface in the turbine region experiences a water level drop of more than 0.5 m. Localized turbine drag also significantly reduces residual kinetic energy in the circulation. However, the influence on the residual volume flux depends on the size of the turbine region.

The theoretical estimate of power potential using 2-D ocean circulation equations has limitations, such as an inability to resolve temporal variability. The simplification of the model also makes it impossible to include the impact of actual coastline and bathymetry. Therefore, the full numerical ocean model HYCOM was used in this study to simulate power extraction from the Florida Current and study the effects of power extraction in greater details. Most of the findings from the full numerical modeling agree with the results from the analytical model. In numerical simulation of power extraction from the Florida Current with HYCOM, two different turbine layouts were considered, one with the majority of the Florida Current between approximately 50-200 m deep occupied by turbines, and the other with a strip of turbines across the Florida Current only occupying one computational cell width at about 60-100 m deep. When the turbines occupy the majority of the Florida Current space in the upper 50-200 m, the mean power density in the Florida Current can drop by more than 1000 W/m^2 , which corresponds to a mean surface current speed drop

of more than 1 m/s. At the same time, a significant rise in mean power density to the east of the Bahamas is observed, indicating an obvious flow rerouting from the Florida Strait eastward to the east offshore of the Bahamas. The volume flux in the Florida Current can be reduced by more than 50% and the energy flux by more than 80% in the first turbine layout. The power dissipation and the residual energy flux in the Florida Current do not add up to the original energy flux, implying a substantial energy loss in the Florida Strait channel, most of which is diverted to the rerouted flow channel east of the Bahamas. A very small portion is diverted to the west of Florida.

For the second turbine layout in which the turbines occupy a much smaller space in the Florida Current, the power dissipation from turbines is also lower. The greatest power density drop in the Florida Current in this scenario occurs immediately downstream of the turbine region on the order of 500 W/m^2 , and the peak mean current speed drops on the order of 0.5 m/s. With the power extraction in this scenario, residual energy flux in the Florida Current drops by about 20-30%, and there is also a net loss of energy in the Florida Strait channel compared with the baseline case. Similar to scenario 1, a portion of the flow is diverted east of the Bahamas and contributes to an increase in the flow strength there.

Although the original undisturbed volume transport in the Florida Current features a prominent seasonal variation with the strongest flux occurring in summer, a significantly higher power extraction in summer is not observed from the simulation due to more energy flux being diverted during summer time. The flow reduction in the Florida Current and flow strengthening east of the Bahamas is stronger in summer time and relatively weaker in other seasons, causing a reduced seasonal variability of the residual fluxes through the Florida Strait channel.

The power extraction with turbines also significantly changes the water level in the vicinity of the power extraction site, as is also predicted by the analytical model. In the first turbine layout, the water level at the power extraction site drops by more than 0.5 m, on the same order of magnitude as the estimate by the analytical model. In the second layout, the water level drops by less than 0.2 m. The numerical model also reveals that power extraction in the Florida Current results in water level increase of up to 0.3 m along

the Gulf and Florida coasts.

The effects of the power extraction in the Florida Current on the mean flow field is limited to the near field of the power extraction site, however its temporal influence reaches much farther both upstream and downstream. In the downstream, eddies created by the merging of the original Florida Current and the rerouted flow east of the Bahamas cause intermittent changes to both velocity and Sea Surface Height fields. In the upstream, the temporal impact of power extraction can be felt as far as the near the equator where power extraction causes shifts of the instantaneous flow field in time and space but has negligible effect on the annual mean flow field and the overall statistics.

This dissertation describes a comprehensive resource assessment of ocean current energy for the United States with special emphasis on the most energetic and promising site for power extraction, the Florida Current. This resource assessment not only considers the undisturbed power density as an indicator of richness of kinetic energy potential, but also reveals the actual rate of power generation using dynamic models as a more precise measure of recoverable energy resource. Unique contributions of this work include:

- Performed characterization of ocean current energy resources for the Florida Current area with 7 years of ocean model data and ocean observational data;
- Estimated power potential from ocean currents in the Gulf Stream system considering cumulative effects from turbines;
- Performed full numerical simulation of power extraction from the Florida Current and evaluated the hydrodynamic effects on both near and far fields.
- Developed GIS mapping with web interface of ocean current energy resources for the United States at more than 8,000 collection points;

Although this study predicts up to approximately 5 GW of extractable power in theory from the Florida Current, the practically recoverable power is expected to be much lower due to technological, economic and environmental constraints. However, even if only 30% of the power in theory can be recovered, the power generation will be more than that from a

typical nuclear power plant, enough to support a million homes based on the average annual U.S. residential electricity consumption estimated by U.S. Energy Information Administration (<http://www.eia.gov>). However, this estimate is based on the extreme scenario which exploits the maximum power potential from the Florida Current. Moreover, power extraction from the Florida Current does have possible negative impacts. Based on the results of this study, flow velocity will increase along the east coast of Florida and the coasts of the Bahamas upon power extraction from the Florida Current, which will possibly change the characteristics of sediment transport in these coastal zones and pose potential threats to coastline changes. A moderate water level rise up to 0.3 m is also predicted along the Gulf coast that could threaten the coastal ecosystem and man-made infrastructures in the Gulf with low elevation, change the beach profiles and increase storm vulnerability. The ramifications could include additional investment in beach maintenance and nourishment.

Technology for extracting power from ocean currents is still at its early stage, and studies are mainly theoretical. The industry has been making steady progress in both ocean current power technology and its sibling tidal power with the nation's first commercial tidal power plant recently going online in the Bay of Fundy in Maine. Engineering challenges remain for extracting power from the Florida Current. Turbine technology robust enough to withstand extreme storm events along the Florida coast needs to be developed and tested, along with robust mooring and power transmission systems. The interaction between turbines and marine animals also needs to be studied in hopes of minimizing environmental impacts. Most marine animals are probably able to avoid direct confrontation with underwater turbines, but the turbulence created by underwater devices may pose threat to the marine ecosystem. Future studies recommended to further advance knowledge in recovering ocean current energy from the Florida Current include:

- Perform simulations with higher resolution in the Gulf Stream area to obtain more accurate prediction of power extraction;
- Simulate turbine performance in the flow and study turbine interactions with model

grids fine enough to resolve actual turbine scale; study the interaction between turbulence generated by turbines and the marine environment;

- Perform modeling of sediment transport along the Florida and Gulf coasts due to current velocity and Sea Surface Height changes from power extraction in the Florida Current;
- Perform experimental field tests of specific types of turbines.

In conclusion, ocean currents especially the Gulf Stream system can be a potential energy resource for the United States. However, the power potential is not solely governed by the kinetic power density of the current flow. Energy extraction project should proceed with caution in that negative impacts on the coastal regions and marine environment may result. Future studies using means of both numerical simulation and field tests will be helpful to further quantify those influences.

APPENDIX A

DIRECT COMPARISON BETWEEN MODEL AND DRIFTER DATA

This appendix includes figures showing the direct comparison of different ocean model data with the drifter measurement data for each sub-region of the east coast shown in Figure 3.4.

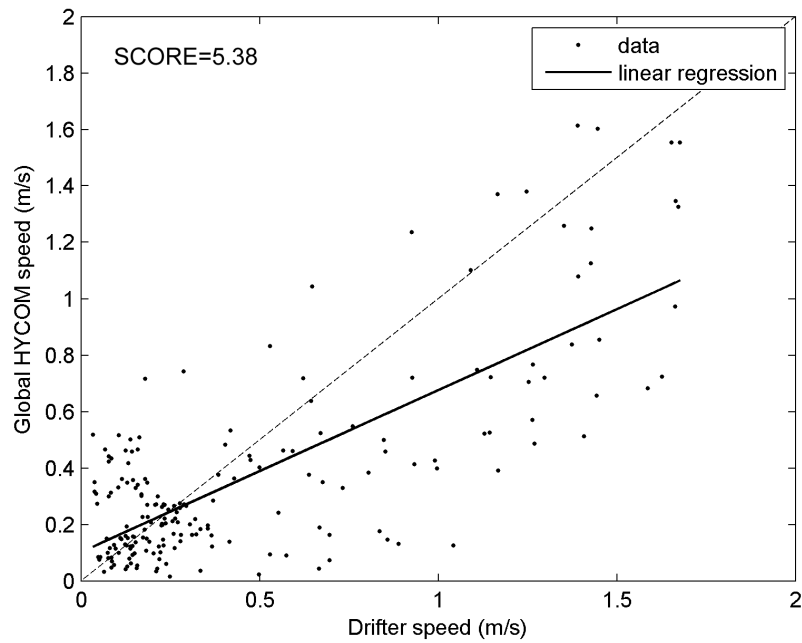


Figure A.1: Comparison of Global HYCOM data with measurement data for E1 region.

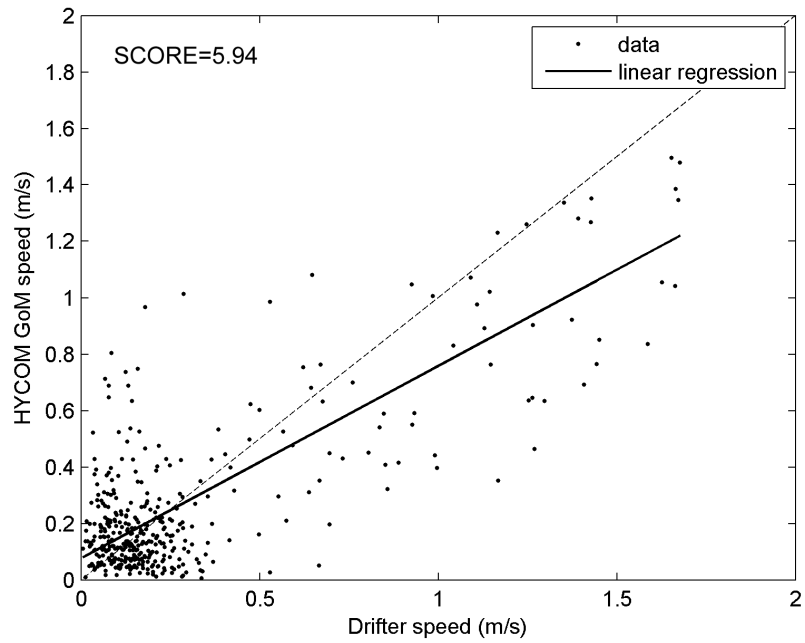


Figure A.2: Comparison of HYCOM GoM data with measurement data for E1 region.

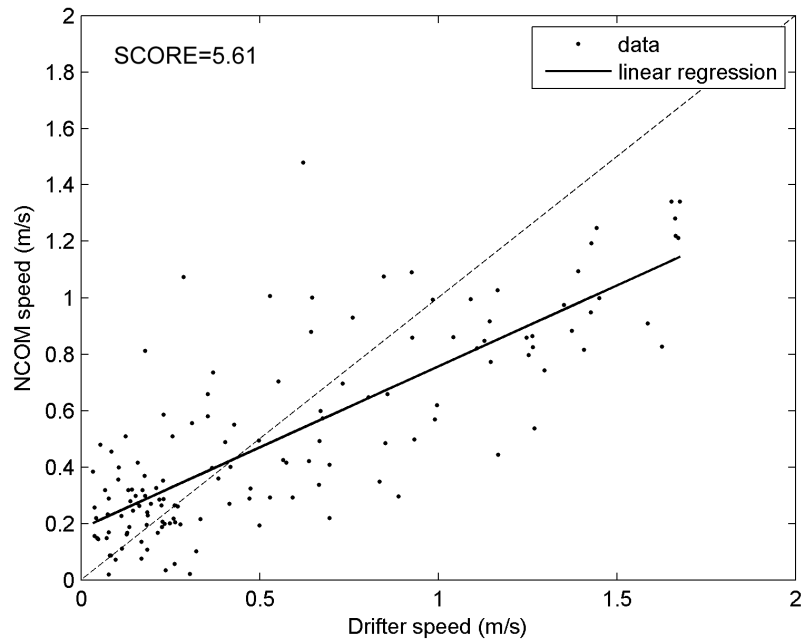


Figure A.3: Comparison of NCOM data with measurement data for E1 region.

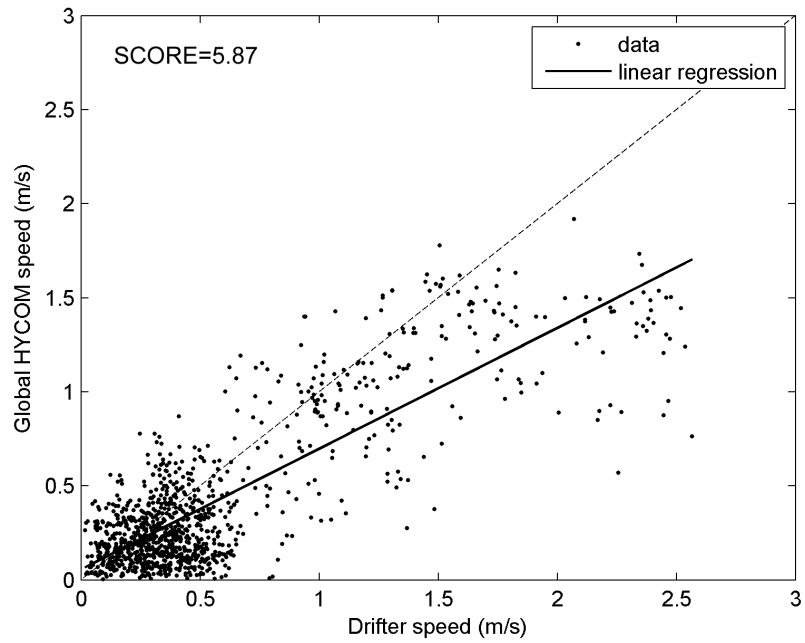


Figure A.4: Comparison of Global HYCOM data with measurement data for E2 region.

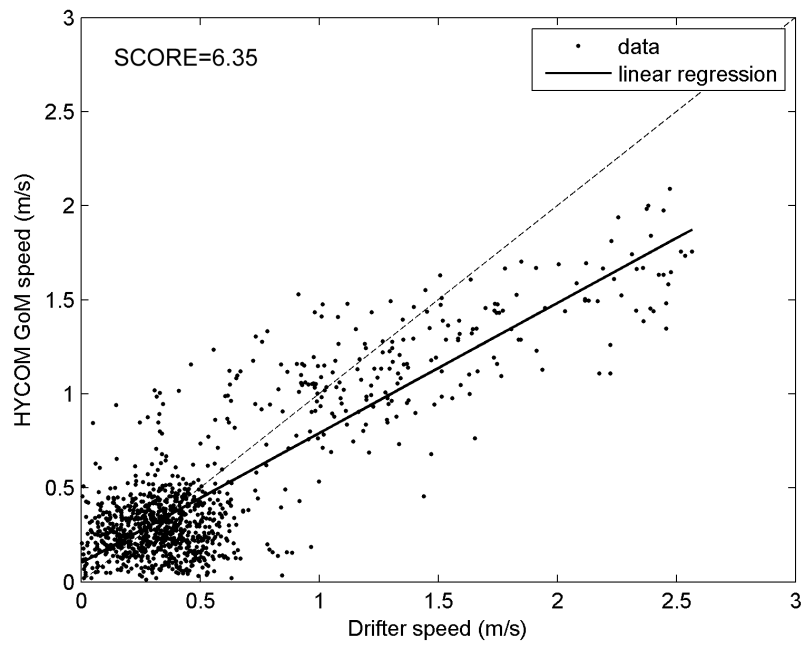


Figure A.5: Comparison of HYCOM GoM data with measurement data for E2 region.

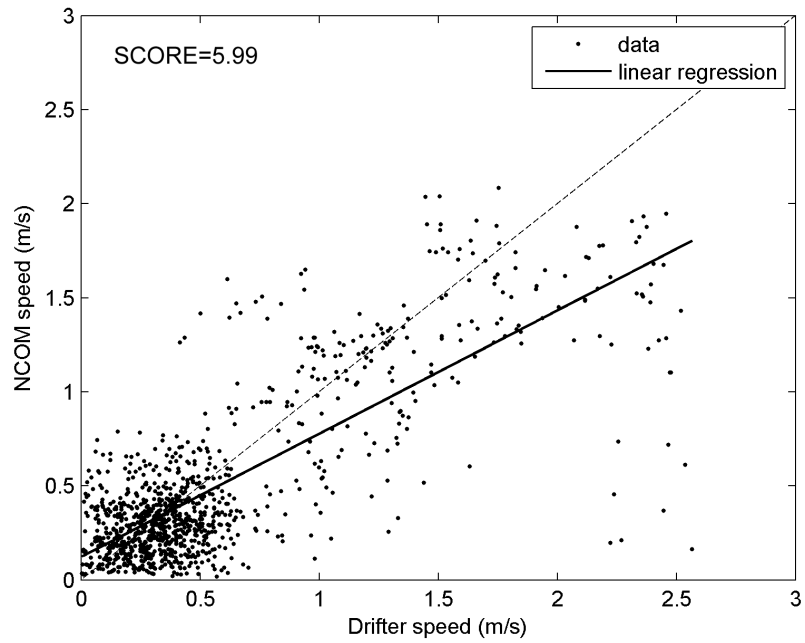


Figure A.6: Comparison of NCOM data with measurement data for E2 region.

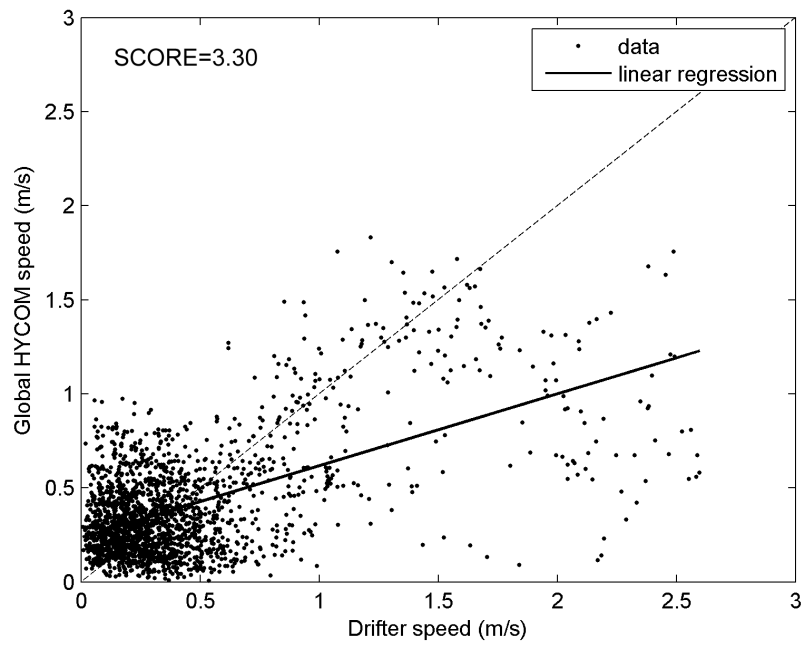


Figure A.7: Comparison of Global HYCOM data with measurement data for E3 region.

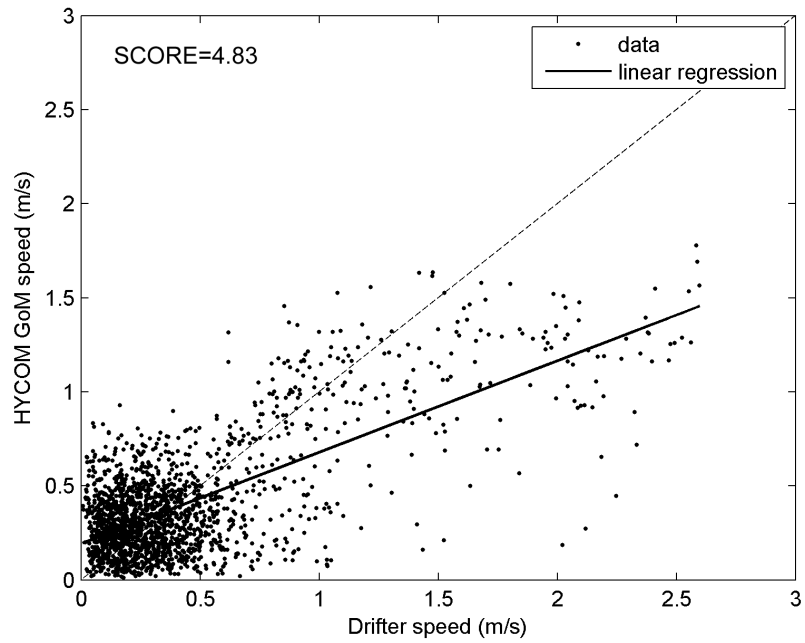


Figure A.8: Comparison of HYCOM GoM data with measurement data for E3 region.

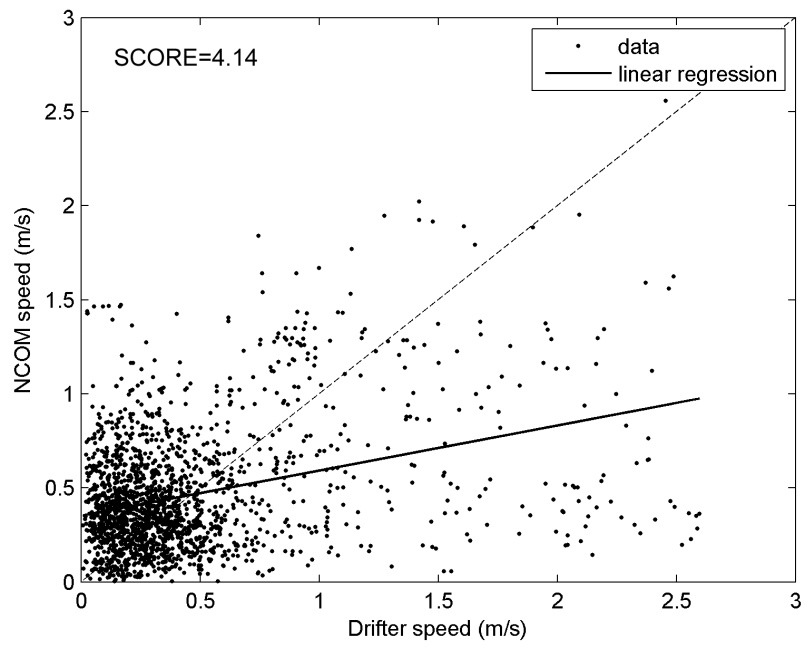


Figure A.9: Comparison of NCOM data with measurement data for E3 region.

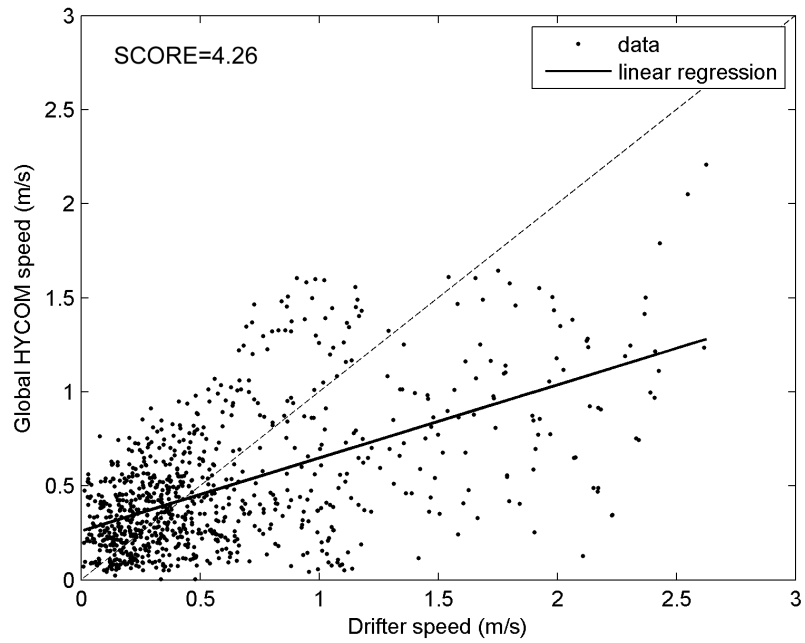


Figure A.10: Comparison of Global HYCOM data with measurement data for E4 region.

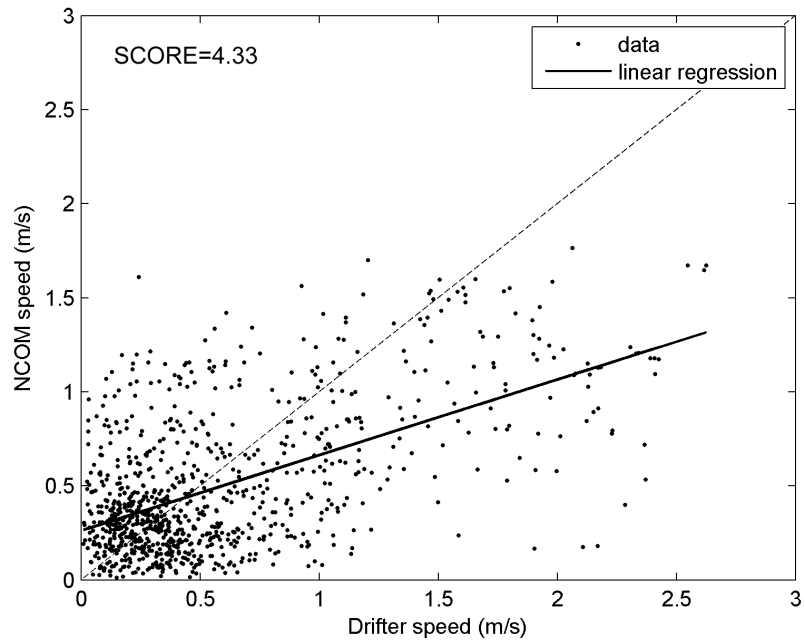


Figure A.11: Comparison of NCOM data with measurement data for E4 region.

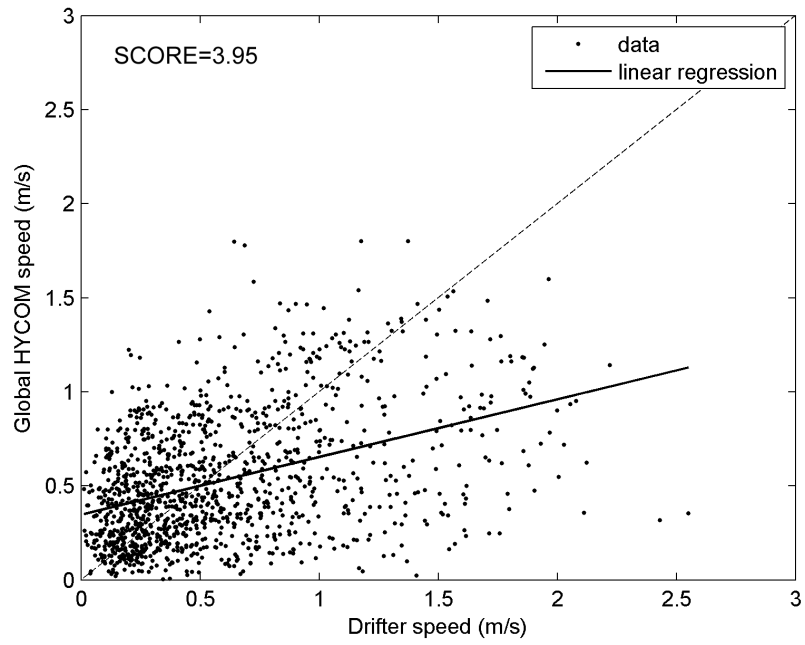


Figure A.12: Comparison of Global HYCOM data with measurement data for E5 region.

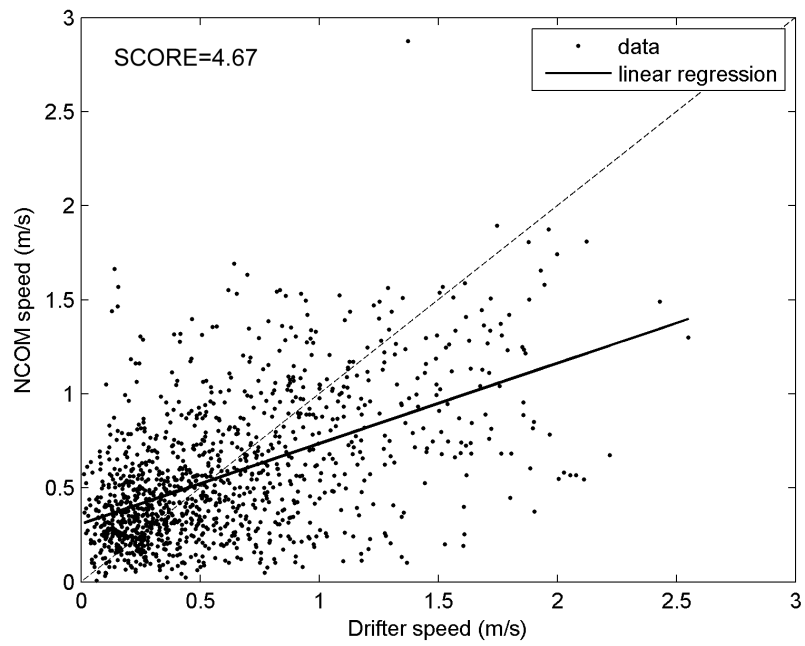


Figure A.13: Comparison of NCOM data with measurement data for E5 region.

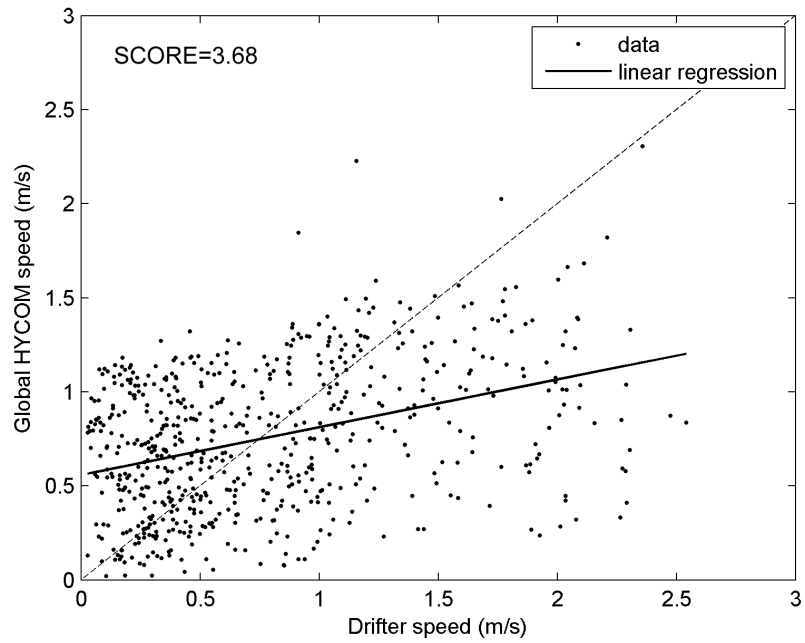


Figure A.14: Comparison of Global HYCOM data with measurement data for E6 region.

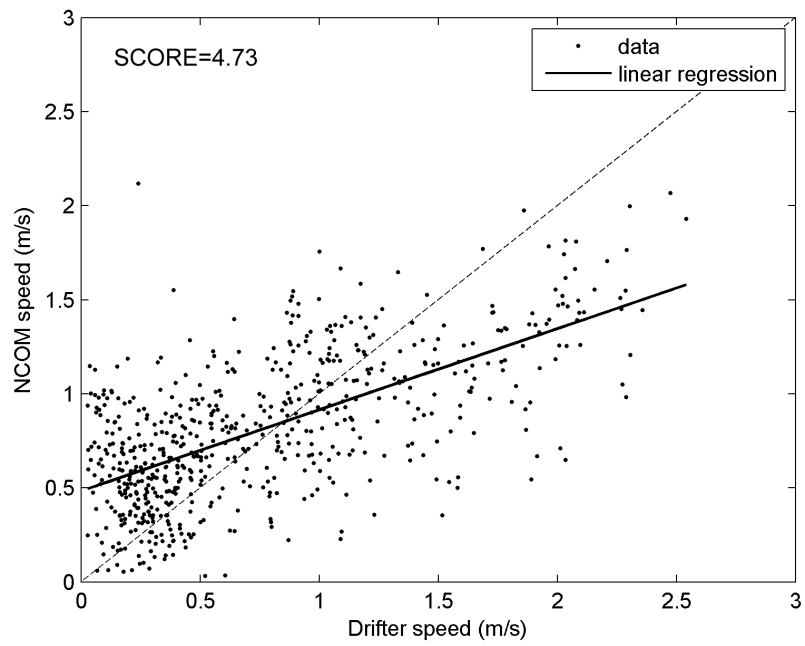


Figure A.15: Comparison of NCOM data with measurement data for E6 region.

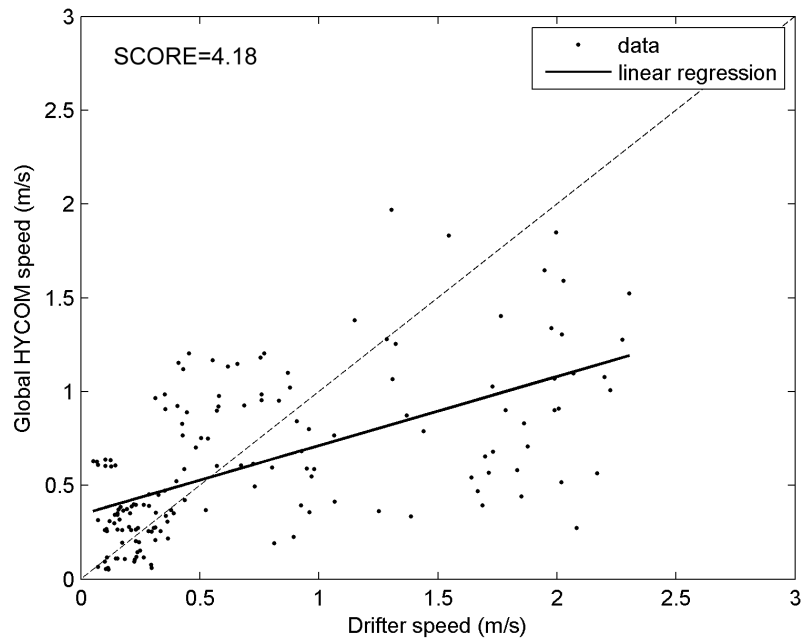


Figure A.16: Comparison of Global HYCOM data with measurement data for E7 region.

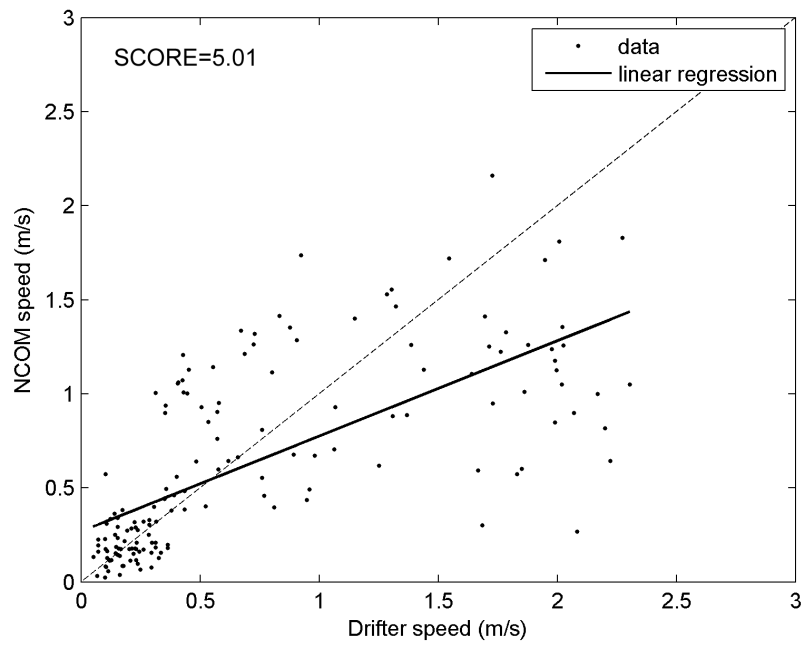


Figure A.17: Comparison of NCOM data with measurement data for E7 region.

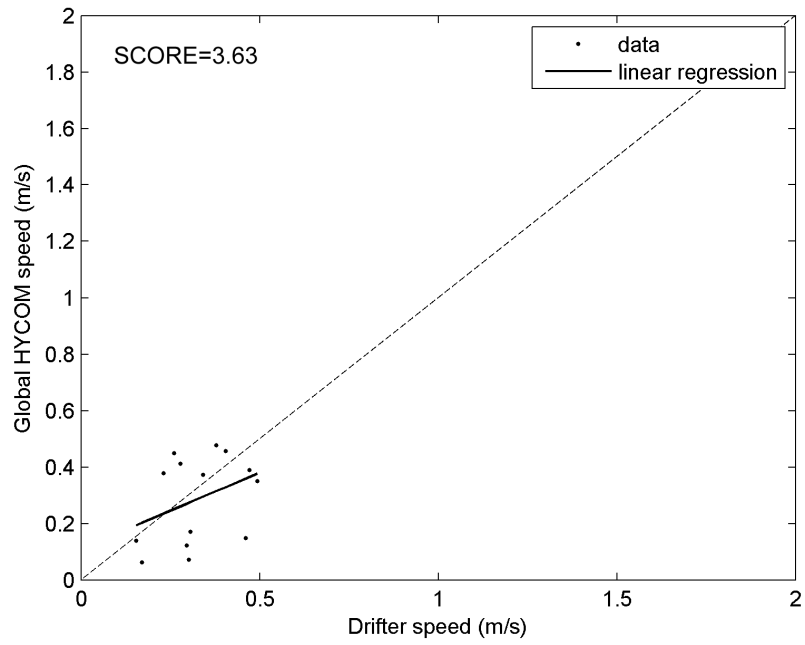


Figure A.18: Comparison of Global HYCOM data with measurement data for E8 region.

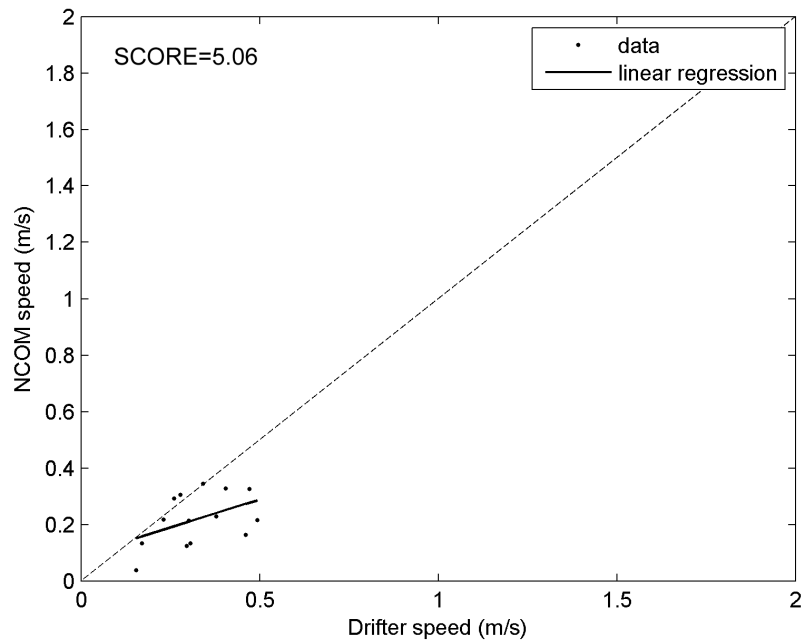


Figure A.19: Comparison of NCOM data with measurement data for E8 region.

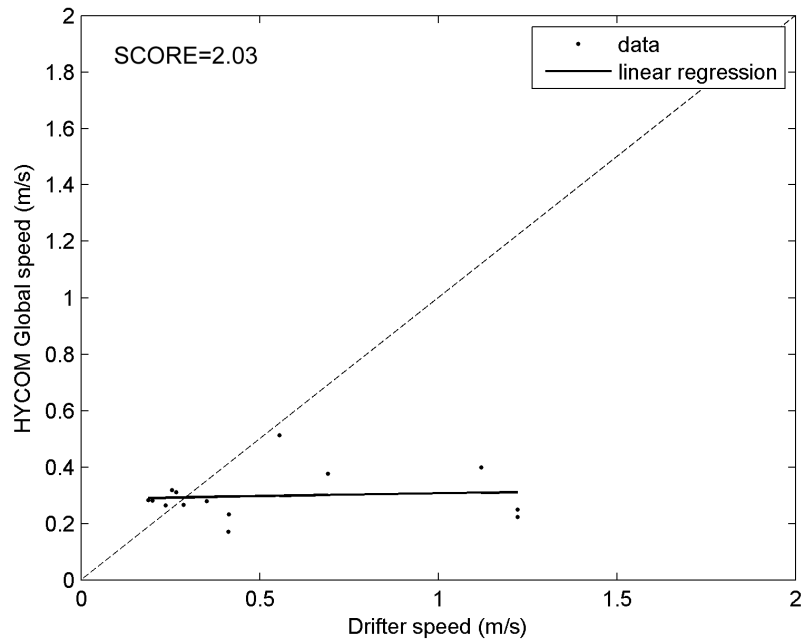


Figure A.20: Comparison of Global HYCOM data with measurement data for E9 region.

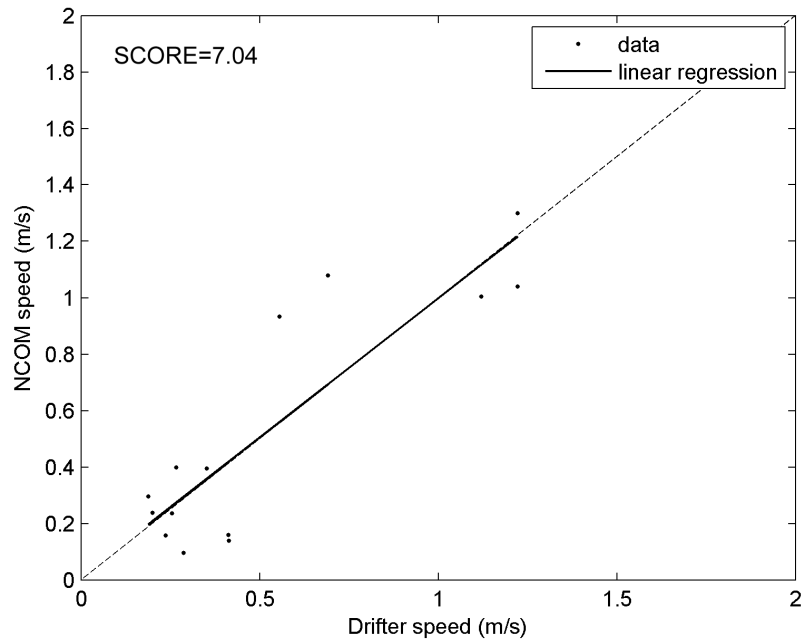


Figure A.21: Comparison of NCOM data with measurement data for E9 region.

REFERENCES

- Asmus, P. and Wheelock, C. (2009). Hydrokinetic and ocean energy. Technical report, www.pikerresearch.com.
- Auer, S. (1987). Five-year climatological survey of the Gulf Stream system and its associated rings. *Journal of Geophysical Research*, 92:11709–11726.
- Bahaj, A. S. and Myers, L. E. (2003). Fundamentals applicable to the utilisation of marine current turbines for energy production. *Renewable Energy*, 28(14):2205–2211.
- Baringer, M. O. and Larsen, J. C. (2001). Sixteen years of Florida Current transport at 27 N. *Geophysical Research Letters*, 28(16):3179–3182.
- Barron, C. N., Kara, A. B., Martin, P. J., Rhodes, R. C., and Smedstad, L. F. (2006). Formulation, implementation and examination of vertical coordinate choices in the global navy coastal ocean model (NCOM). *Ocean Modelling*, 11(34):347 – 375.
- Bedard, R., Jacobson, P. T., Previsic, M., Musial, W., and Varley, R. (2010). An overview of ocean renewable energy technologies. *Oceanography*, 23(2):22–31.
- Ben Elghali, S., Benbouzid, M., and Charpentier, J.-F. (2007). Marine tidal current electric power generation technology: State of the art and current status. In *Electric Machines Drives Conference, 2007. IEMDC '07. IEEE International*, volume 2, pages 1407–1412.
- Beretta, G. P. (2007). World energy consumption and resources: an outlook for the rest of the century. *International Journal of Environmental Technology and Management*, 7(1-2):99–112.
- Betz, A. (1926). *Wind energy and its utilization by windmills*. Vandenhoeck and Ruprecht, Goettingen, Germany.
- Beyene, A. and Wilson, J. H. (2007). Digital mapping of california wave energy resource. *International Journal of Energy Research*, 31(12):1156–1168.
- Bleck, R. (2002). An oceanic general circulation model framed in hybrid isopycnic-cartesian coordinates. *Ocean Modelling*, 4(1):55–88.
- Blunden, L. and Bahaj, A. (2006). Initial evaluation of tidal stream energy resources at portland bill, UK. *Renewable Energy*, 31(2):121 – 132.
- Boning, C. W., Doscher, R., and Budich, R. G. (1991). Seasonal transport variation in the western subtropical north-atlantic - experiments with an eddy-resolving model. *Journal of Physical Oceanography*, 21(9):1271–1289.
- Bryden, I. G., Couch, S. I., Owen, A., and Melville, G. (2007). Tidal current resource assessment. *Proceedings of the Institution of Mechanical Engineers Part a-Journal of Power and Energy*, 221(A2):125–135.
- Chassignet, E. P., Smith, L. T., Bleck, R., and Bryan, F. O. (1996). A model comparison: Numerical simulations of the north and equatorial atlantic oceanic circulation in depth and isopycnic coordinates. *Journal of Physical Oceanography*, 26(9):1849–1867.

- Clement, A., McCullen, P., Falco, A., Fiorentino, A., Gardner, F., Hammarlund, K., Lemois, G., Lewis, T., Nielsen, K., Petroncini, S., Pontes, M.-T., Schild, P., Sjstrm, B.-O., Srensen, H. C., and Thorpe, T. (2002). Wave energy in Europe: current status and perspectives. *Renewable and Sustainable Energy Reviews*, 6(5):405 – 431.
- Csanady, G. T. (1989). Energy dissipation and upwelling in a western boundary current. *Journal of Physical Oceanography*, 19(4):462–473.
- Defne, Z. (2010). *Multi-criteria assessment of wave and tidal power along the Atlantic coast of the southeastern USA*. PhD thesis, Georgia Institute of Technology.
- Defne, Z., Haas, K. A., and Fritz, H. M. (2011). Numerical modeling of tidal currents and the effects of power extraction on estuarine hydrodynamics along the Georgia coast, USA. *Renewable Energy*, 36(12):3461 – 3471.
- Defne, Z., Haas, K. A., Fritz, H. M., Jiang, L. D., French, S. P., Shi, X., Smith, B. T., Neary, V. S., and Stewart, K. M. (2012). National geodatabase of tidal stream power resource in USA. *Renewable & Sustainable Energy Reviews*, 16(5):3326–3338.
- Duerr, A. and Dhanak, M. (2012). An assessment of the hydrokinetic energy resource of the Florida Current. *IEEE Journal of Oceanic Engineering*, 37(2):281 –293.
- Duing, W. (1975). Synoptic studies of transients in the Florida Current. *Journal of Marine Research*, 33:53–73.
- Duran, D. (1999). *Numerical methods for wave equations in geophysical fluid dynamics*. Springer, New York.
- EIA (2010). Levelized cost of new generation resources in the annual energy outlook 2011. Technical report, US Energy Information Administration of the US Department of Energy.
- EIA (2013). Electric power monthly. Technical report, U.S. Energy Information Administration.
- Elert, G. (2002). The physics factbook. Online resource at <http://hypertextbook.com/facts/2002/EugeneStatnikov.shtml> (accessed in 2012).
- EPRI (2006). Wave energy conversion (WEC) project. Technical report, Electric Power Research Institute.
- EPRI (2011). Mapping and assessment of the united states ocean wave energy resource. Technical report, Electric Power Research Institute.
- Esteban, M. and Leary, D. (2012). Current developments and future prospects of offshore wind and ocean energy. *Applied Energy*, 90(1):128 – 136.
- ExxonMobil (2012). 2012 the outlook for energy: A view to 2040. Technical report, ExxonMobil.
- Garrett, C. and Cummins, P. (2004). Generating power from tidal currents. *Journal of waterway, port, coastal, and ocean engineering*, 130(3):114–118.

- Garrett, C. and Cummins, P. (2005). The power potential of tidal currents in channels. *Proceedings of the Royal Society a-Mathematical Physical and Engineering Sciences*, 461(2060):2563–2572.
- Garrett, C. and Cummins, P. (2008). Limits to tidal current power. *Renewable energy*, 33:2485–2490.
- Gibson, J., Killberg, P., Uppala, S., Hernandez, A., Nomura, A., and Serrano, E. (1997). ERA description. Technical report, ECMWF ERA-15 Project Report Series 1.
- Gorban, A. N., Gorlov, A. M., and Silantyev, V. M. (2001). Limits of the turbine efficiency for free fluid flow. *Journal of Energy Resources Technology*, 123(4):311–317.
- Gould, W. (1985). Physical oceanography of the azores front. *Progress in Oceanography*, 14:167–190.
- Greatbatch, R., Lu, Y., DeYoung, B., and Larsen, J. (1995). The variation of transport through the straits of florida: A barotropic model study. *Journal of Physical Oceanography*, 25(1):2726–2740.
- Gross, M. (1993). *Oceanography, a view of Earth, 6th edition*. Prentice Hall.
- Guney, M. S. and Kaygusuz, K. (2010). Hydrokinetic energy conversion systems: A technology status review. *Renewable and Sustainable Energy Reviews*, 14(9):2996–3004.
- Haidvogel, D. B., Arango, H., Budgell, W. P., Cornuelle, B. D., Curchitser, E., Di Lorenzo, E., Fennel, K., Geyer, W. R., Hermann, A. J., Lanerolle, L., Levin, J., McWilliams, J. C., Miller, A. J., Moore, A. M., Powell, T. M., Shchepetkin, A. F., Sherwood, C. R., Signell, R. P., Warner, J. C., and Wilkin, J. (2008). Ocean forecasting in terrain-following coordinates: Formulation and skill assessment of the regional ocean modeling system. *Journal of Computational Physics*, 227(7):3595–3624.
- Hall, M. and Fofonoff, N. (1993). Downstream development of the Gulf Stream from 68 to 55W. *Journal of Physical Oceanography*, 23(C1):225–249.
- Halliwel, G. R. (2004). Evaluation of vertical coordinate and vertical mixing algorithms in the hybrid-coordinate ocean model (HYCOM). *Ocean Modelling*, 7(3-4):285–322.
- Hammons, T. J. (1993). Tidal power. *Proceedings of the IEEE*, 81(3):419–433.
- Hanson, H. P., Bozek, A., and Duerr, A. E. (2011). The Florida Current: A clean but challenging energy resource. *EOS, Transactions American Geophysical Union*, 92:29.
- Hanson, H. P., Skemp, S. H., Alsenas, G. M., and Coley, C. E. (2010). Power from the Florida Current a new perspective on an old vision. *Bulletin of the American Meteorological Society*, 91(7):861–866.
- Henfridsson, U., Neimane, V., Strand, K., Kapper, R., Bernhoff, H., Danielsson, O., Leijon, M., Sundberg, J., Thorburn, K., Ericsson, E., and Bergman, K. (2007). Wave energy potential in the baltic sea and the danish part of the north sea, with reflections on the skagerrak. *Renewable Energy*, 32(12):2069 – 2084.
- Hofmann, E. E. and Worley, S. J. (1986). An investigation of the circulation of the gulf of mexico. *Journal of Geophysical Research-Oceans*, 91(C12):14221–14236.

- Hogg, N. and Johns, W. (1995). Western boundary currents. *U.S. National Report to International Union of Geodesy and Geophysics 1991-1994*, 33:1311–1334.
- Iselin, C. (1936). A study of the circulation of the western North Atlantic. *Physical Oceanography and Meteorology*, 4:101.
- Johns, W. E., Shay, T. J., Bane, J. M., and Watts, D. R. (1995). Gulf Stream structure, transport, and recirculation near 68w. *J. Geophys. Res.*, 100(C1):817–838.
- Johnson, R. (2006). *Statistics: Principles and Methods 5th Edition*, page 671. Wiley and Sons.
- Joyce, T. (1984). Velocity and hydrographic structure of a Gulf Stream warm-core ring. *J. Phys. Oceanogr.*, 14(5):936–947.
- Kara, A. B., Rochford, P. A., and Hurlburt, H. E. (2000). Efficient and accurate bulk parameterizations of air-sea fluxes for use in general circulation models. *J. Atmos. Oceanic Technol.*, 17:1421–1438.
- Karsten, R. H., McMillan, I. M., Lickley, M. J., and Haynes, R. D. (2008). Assessment of tidal current energy in the minas passage, Bay of Fundy. *Proceedings of the Institution of Mechanical Engineers Part a-Journal of Power and Energy*, 222(A5):493–507.
- Keith, D. W., DeCarolis, J. F., Denkenberger, D. C., Lenschow, D. H., Malyshev, S. L., Pacala, S., and Rasch, P. J. (2004). The influence of large-scale wind power on global climate. *Proceedings of the National Academy of Sciences of the United States of America*, 101(46):16115–16120.
- Khan, M., Bhuyan, G., Iqbal, M., and Quaicoe, J. (2009). Hydrokinetic energy conversion systems and assessment of horizontal and vertical axis turbines for river and tidal applications: A technology status review. *Applied Energy*, 86(10):1823 – 1835.
- Kofoed, J. P., Frigaard, P., Friis-Madsen, E., and Srensen, H. C. (2006). Prototype testing of the wave energy converter wave dragon. *Renewable Energy*, 31(2):181 – 189.
- Koller, J., Koppel, J., and Peters, W. (2006). *Offshore wind energy: Research on environmental impacts*, page 135. New York: Springer.
- Large, W. G., Williams, J. C. M., and Doney, S. C. (1994). Oceanic vertical mixing: a review and a model with a nonlocal boundary layer parameterization. *Rev. Geophys.*, 32(4):363–403.
- Larsen, J. C. and Sanford, T. B. (1985). Florida Current volume transports from voltage measurements. *Science*, 227(4684):302–304.
- Lawn, C. (2003). Optimization of the power output from ducted turbines. *Proc. Instn Mech. Engrs, Part A: J. Power and Energy*, 217:107–118.
- Leaman, K., Molinari, R., and Vertes, P. (1987). Structure and variability of the Florida Current at 27 n. *Journal of Physical Oceanography*, 17(5):565–583.
- Lee, T. (1975). Florida Current spin-off eddies. *Deep-Sea Research*, 22(11):753 – 765.

- Lee, T. and Williams, E. (1988). Wind-forced transport fluctuations of the Florida Current. *Journal of Physical Oceanography*, 18:937–946.
- Levitus, S. and Boyer, T. (1994). World ocean atlas 1994. Technical report, NOAA Atlas NESDIS, NOAA, Silver Spring, Md.
- Lissaman, P. B. S. (1979). Coriolis program. *Oceanus*, 22(4):23–28.
- Lueck, R. and Reid, R. (1984). On the production and dissipation of mechanical energy in the ocean. *Journal of Geophysical Research-Oceans*, 89(Nc3):3439–3445.
- Mann, C. (1967). The termination of the Gulf Stream and the beginning of the North Atlantic Current. *Deep-Sea Research*, 14:337–359.
- Manwell, J. F., McGowan, J. G., and Rogers, A. L. (2010). *Wind Energy Explained: Theory, Design and Application*. John Wiley & Sons Ltd, UK.
- Marais, E., Chowdhury, S., and Chowdhury, S. (2011). Theoretical resource assessment of marine current energy in the Agulhas Current along South Africa’s east coast. In *Power and Energy Society General Meeting, 2011 IEEE*, pages 1–8.
- Melek-Madani, R. (2012). *Physical oceanography: a mathematical introduction with MATLAB*. Capman and Hall/CRC.
- Mellor, G. L. and Yamada, T. (1982). Development of a turbulence closure model for geophysical fluid problems. *Rev. Geophys. Space Phys.*, 20(4):851–875.
- Miller, L. M., Gans, F., and Kleidon, A. (2011a). Estimating maximum global land surface wind power extractability and associated climatic consequences. *Earth Syst. Dynam. Discuss.*, 2:1–12.
- Miller, L. M., Gans, F., and Kleidon, A. (2011b). Jet stream wind power as a renewable energy resource: little power, big impacts. *Earth Syst. Dynam. Discuss.*, 2:435–465.
- MMS (2006). Technology white paper on wave energy potential on the u.s. outer continental shelf. Technical report, Minerals Management Service Renewable Energy and Alternate Use Program, U.S. Department of the Interior.
- Mueller, M. and Wallace, R. (2008). Enabling science and technology for marine renewable energy. *Energy Policy*, 36(12):4376–4382.
- Musial, W. and Butterfield, C. (2004). Future for offshore wind energy in the united states. *EnergyOcean Proceedings*.
- Myers, L. and Bahaj, A. S. (2006). Power output performance characteristics of a horizontal axis marine current turbine. *Renewable Energy*, 31(2):197–208.
- NASA (2012). Nasa seawifs imaging project image archive. Online resource at <http://oceancolor.gsfc.nasa.gov/SeaWiFS/> (accessed 2012).
- Neary, V., Gunawan, B., and Ryou, A. (2012). Performance evaluation of hycom-gom for hydrokinetic resource assessment in the florida strait. Technical report, U.S. Department of Energy.

- New, A. L. and Bleck, R. (1995). An isopycnic model study of the North-Atlantic .2. interdecadal variability of the subtropical gyre. *Journal of Physical Oceanography*, 25(11):2700–2714.
- NGDC (1995). Terrainbase, global 5-minute ocean depth and land elevation, from NGDC. Technical report, Research Data Archive at the National Center for Atmospheric Research, Computational and Information Systems Laboratory.
- Niiler, P. and Kraus, E. B. (1977). *One-dimensional models, in Modeling and Prediction of the Upper Layers of the Ocean*. Pergamon Press, New York.
- Niiler, P. and Richardson, W. (1973). Seasonal variability of the Florida Current. *Journal of Marine Research*, 31:144–167.
- NRC (2013). An evaluation of the u.s. department of energy’s marine and hydrokinetic resource assessments. Technical report, The National Academies Press.
- OpenHydro (2009). Nova scotia power and openhydro unveil in-stream tidal turbine, final preparations underway for deployment in Bay of Fundy. Online resource at <http://www.openhydro.com/news/> (accessed 2012).
- Polagye, B., Kawase, M., and Malte, P. (2009). In-stream tidal energy potential of puget sound, washington. *Proceedings of the Institution of Mechanical Engineers Part a-Journal of Power and Energy*, 223(A5):571–587.
- Prandle, D. (1984). Simple theory for designing tidal power schemes. *Advances in Water Resources*, 7(1):21 – 27.
- Price, J. F., Weller, R. A., and Pinkel, R. (1986). Diurnal cycling: Observations and models of the upper ocean response to diurnal heating, cooling, and wind mixing. *J. Geophys. Res.*, 91(C7):8411–8427.
- Raye, R. E. (2002). Characterization study of the florida current at 26.11 north latitude, 79.50 west longitude for ocean current power generation. Master’s thesis, Florida Atlantic University.
- REN21 (2012). The REN21 renewables 2011 global status report. Technical report, renewable Energy Policy Network for the 21st Century (<http://www.ren21.net/>).
- Rhodes, R. C., Hurlburt, H. E., Wallcraft, A. J., Barron, C. N., Martin, P. J., Metzger, E. J., Shriver, J. F., Ko, D. S., Smedstad, O. M., Cross, S. L., and Kara, A. B. (2002). Navy real-time global modeling systems. *Oceanography*, 15(1):29–43.
- Ring-Group (1981). Gulf-stream cold-core rings - their physics, chemistry, and biology. *Science*, 212(4499):1091–1100.
- Roberts, M. J., Marsh, R., New, A. L., and Wood, R. A. (1996). An intercomparison of a bryan-cox-type ocean model and an isopycnic ocean model .1. the subpolar gyre and high-latitude processes. *Journal of Physical Oceanography*, 26(8):1495–1527.
- Salter, S. (1974). Wave power. *Nature*, 249(5459):720–724.
- Schott, F. and Duing, W. (1976). Continental shelf waves in the florida straits. *Journal of Physical Oceanography*, 6(4):451–460.

- Shapiro, G. I. (2011). Effect of tidal stream power generation on the region-wide circulation in a shallow sea. *Ocean Science*, 7(1):165–174.
- Shay, L. K., Lee, T. N., Williams, E. J., Graber, H. C., and Rooth, C. G. H. (1998). Effects of low-frequency current variability on near-inertial submesoscale vortices. *J. Geophys. Res.*, 103(C9):18691–18714.
- Stern, M. (1975). *Ocean Circulation Physics*, page 246. Academic Press.
- Stewart, R. (2008). Introduction to physical oceanography. Open Source Textbook at <http://oceanworld.tamu.edu/> (accessed 2012).
- Stommel, H. (1948). the westward intensification of wind-driven ocean currents. *Transactions American Geophysical Union*, 29:202–206.
- Sutherland, G., Foreman, M., and Garrett, C. (2007). Tidal current energy assessment for johnstone strait, vancouver island. *Proceedings of the Institution of Mechanical Engineers Part a-Journal of Power and Energy*, 221(A2):147–157.
- Sverdrup, H. (1947). Wind-driven currents in a baroclinic ocean; with application to the equatorial currents of the eastern pacific. *Proc. Natl. Acad. Sci.*, 33(11):318–326.
- Thurman, H. V. and Trujillo, A. P. (2003). *Introductory Oceanography*, chapter 8. Prentice Hall.
- Twidell, J. and Weir, A. (2006). *Renewable Energy Resources*. Taylor and Francis.
- Vallis, G. (2006). *Atmospheric and Oceanic Fluid Dynamics : Fundamentals and Large-Scale Circulation*. Cambridge University Press.
- Vanek, F., Albright, L., and Angenent, L. (2008). *Energy systems engineering: evaluation and implementation*. New York: McGraw-Hill.
- Venkatesh, S., Sanderson, B., and El-Tahan, M. (1990). Optimum deployment of satellite-tracked drifters to support iceberg drift forecasting. *Cold Regions Science and Technology*, 18(2):117 – 131.
- VerdantPower (2007). Verdant Powers Roosevelt Island Tidal Energy (RITE) project. Online resource at <http://www.verdantpower.com/Initiatives/eastriver.shtml> (accessed 2012).
- Von Arx, W., Stewart, H., and Apel, J. (1974). The Florida Current as a potential source of usable energy. *Proc. Mac Arthur Workshop Feasibility of Extracting Usable Energy From the Florida Current*, pages 91–101.
- Westwood, A. (2008). Seagen installation moves forward. *Renewable Energy Focus*, 9(3):26 – 27.
- Wolf, J., Walkington, I. A., Holt, J., and Burrows, R. (2009). Environmental impacts of tidal power schemes. *Proceedings of the Institution of Civil Engineers-Maritime Engineering*, 162(4):165–177.

- Wright, S. H., Chowdhury, S. P., and Chowdhury, S. (2011). A feasibility study for marine energy extraction from the Agulhas Current. *2011 Ieee Power and Energy Society General Meeting*.
- Wunsch, C. (1998). The work done by the wind on the oceanic general circulation. *Journal of Physical Oceanography*, 28(11):2332–2340.
- Wunsch, C. and Ferrari, R. (2004). Vertical mixing, energy and the general circulation of the oceans. *Annual Review of Fluid Mechanics*, 36:281–314.
- Xu, X., Schmitz, W. J., Hurlburt, H. E., and Hogan, P. J. (2012). Mean atlantic meridional overturning circulation across 26.5n from eddy-resolving simulations compared to observations. *Journal of Geophysical Research: Oceans*, 117(C3).
- Yao, F. C. and Johns, W. E. (2010). A hycom modeling study of the persian gulf: 1. model configurations and surface circulation. *Journal of Geophysical Research-Oceans*, 115.